# Monitoring Radiation Damage in the Vertex Locator and Top Pair Production in LHCb

Henry Brown

The University of Liverpool
October 2013

Thesis submitted in accordance with the requirements of The University of Liverpool for the degree of Doctor of Philosophy

# Abstract

The Large Hadron Collider (LHC) is a proton-proton collider at the European Centre for Nuclear Research (CERN). The LHCb experiment is one of the four main experiments at the LHC. It is designed for the detection of $b\bar{b}$ pairs produced in proton-proton collisions and to make precision measurements of $B$-mesons. The trigger level identification of $B$-mesons is provided by the Vertex Locator (VELO), which is the primary tracking detector of the experiment. Due to its proximity to the interaction point, the VELO is exposed to high levels of radiation damage. A new method of monitoring the damage is to perform current-voltage (IV) scans and to compare the results of these scans to laboratory tests on sample sensors. A method to perform the first $t\bar{t}$ production measurement in the $\eta > 2$ range at the LHC, using a dilepton+$b$-jet channel, is also presented. A fiducial cross-section is obtained of $\sigma_{\text{fid}} = 24.3^{+14.6}_{-9.7}(\text{stat.}) \pm 6.9(\text{syst.}) \pm 0.9(\text{lumi.})\text{fb}$, which is consistent with Standard Model expectations.

The author's work was to perform the analysis of the IV scans and the comparison to the empirical models obtained in test environments, and to develop the method, as well as the necessary theoretical predictions, for the top pair cross-section measurement.

# Declaration

This dissertation is the result of my own work, except where explicit reference is made to the work of others, and has not been submitted for another qualification to this, or any, other university. This dissertation does not exceed the word limit for the respective Degree Committee.

Henry Brown

# Contents

# Acknowledgements

Many people deserve my gratitute for assisting me to getting where I am today. It makes sense to begin from the start, where I must thank my parents for allowing and encouraging me to study physics, and being prepared to support these endeavours. Without them I wouldn't be where I am today, and for that I have to really say thank you.

I am grateful to many people who have assisted in one way or another with my work over the last few years. I owe many thanks to, in no particular order, Phil Allport, my undergraduate supervisor, Gianluigi Casse and Tony Affolder, who helped me so much with my masters project which really got me on the track to do a PhD, Ilya Tsurin, Ashley Greenall, Tim Jones, Mike Wormald, Karol Hennessy, Kurt Rinnert, Stephen Farry, Kate Shaw, Rhorry Gauld, Tara Shears, Steve Maxfield, Paul Laycock, Eduardo Rodrigues, Girish Patel and all the unfortunate souls who have ever had to share an office with me. My two supervisors for this PhD, Themis Bowcock and David Hutchcroft have provided invaluable input and put in a lot of work in helping me to get to where I am, thus they have their own sentence reserved for them. I also wish to thank the University of Liverpool, and STFC, for allowing me the opportunity to undertake these studies.

I want to close my acknowledgements by thanking the friends which have helped me to get here, who I haven't mentioned above. Thanks for the great times in Liverpool, and thanks for the great times in CERN.

# Chapter 1

# Introduction

Particle physics is the study of the fundamental forces in the Universe. The most successful theory to date is known as the Standard Model (SM). However, the SM has yet to incorporate the theory of gravity and it does not predict several key observations: neutrino oscillations, a mechanism for generating neutrino masses, and the matter/anti-matter asymmetry in the Universe. The need for a fuller understanding of the SM, and the development of ways in which it could be extended is one of the driving forces behind particle physics. To this end, stringent tests of the SM must be performed.

This thesis presents a first study of the production of top quarks, the heaviest known particle, in an unexplored region of phase space at the LHC, using the LHCb detector. A brief introduction to the SM, with emphasis on the top quark, is given in Chapter 2. A short description of the LHC, and the LHCb experiment, is outlined in Chapter 3.

An analysis of radiation damage and its effects to the VELO, one of the LHCb sub-detectors, is documented in Chapter 4. Particle reconstruction, identification and triggering in LHCb is described in Chapter 5, before a study of the top quark pair production cross-section in Chapter 6. A summary of the analyses and an outlook is given in Chapter 7.

# Chapter 2

# Theoretical Context

Particle physics is the study of the fundamental constituents of matter, and the forces which govern their interactions. The best theoretical model to date to explain the empirical observations from experiments is the SM. This section will describe key aspects of the SM that are relevant to the top quark analysis presented in Chapter 6.

## 2.1 The Fundamental Particles and Forces

The three forces described in the SM are the electromagnetic, weak, and strong interactions. The SM describes the known fundamental particles: leptons and quarks. The quarks and leptons are the constituents of all matter such as protons, neutrons and electrons, whilst gauge bosons are the quanta of the fields and mediate the interactions between the fundamental particles. The Higgs particle is the only fundamental scalar particle in the SM, and its function is to provide masses to the fermions and bosons.

### 2.1.1 Fermions

Fermions in the SM are divided into two categories, the leptons and the quarks. The fermions are, by definition, spin-$\frac{1}{2}$ particles. The leptons are charged ($Q = -1$) or neutral ($Q = 0$). There are three known generations of charged leptons in the SM. These are, in order of increasing mass: the electron ($e^-$), the muon ($\mu^-$) and the tau ($\tau^-$). These generations display identical properties except for their mass and lepton flavour. The neutral leptons occur in three matching flavours: the electron neutrino ($\nu_e$), the muon neutrino ($\nu_\mu$) and the tau neutrino ($\nu_\tau$). The neutrino masses are not

currently experimentally measured, but have to be non-zero to allow for mixing in the neutrino sector [1].

The quark sector contains three generations of two charged quarks. The charged quarks in a doublet can be classified as an '*up*'-type quark with charge of $Q = +2/3$, and a '*down*'-type quark with charge of $Q = -1/3$. The three generational doublets are: the up and down quarks ($u$ and $d$), the charm and strange quarks ($c$ and $s$), and the top and bottom quarks ($t$ and $b$). The quarks possess a quantum number, *colour*, which takes values of red, green and blue. These generate the colour field responsible for the strong interaction. The leptons are listed in Table 2.1 and the quarks in Table 2.2.

| Generation | Lepton | Mass (MeV/c$^2$) | Spin | Q/e |
|---|---|---|---|---|
| 1 | $e^-$ | 0.510998928(11) | 1/2 | -1 |
| | $\nu_e$ | <0.002 (CL=95%) | 1/2 | 0 |
| 2 | $\mu^-$ | 105.6587315(35) | 1/2 | -1 |
| | $\nu_\mu$ | <0.19 (CL=90%) | 1/2 | 0 |
| 3 | $\tau^-$ | 1776.82(16) | 1/2 | -1 |
| | $\nu_\tau$ | <18.2 (CL=95%) | 1/2 | 0 |

**Table 2.1:** The leptons in the SM [1].

| Generation | Quark | Mass (MeV/c$^2$) | Spin | Q/e |
|---|---|---|---|---|
| 1 | u | $2.3^{+0.7}_{-0.5}$ | 1/2 | 2/3 |
| | d | $4.8^{+0.7}_{-0.3}$ | 1/2 | -1/3 |
| 2 | c | $1275 \pm 25$ | 1/2 | 2/3 |
| | s | $95 \pm 5$ | 1/2 | -1/3 |
| 3 | t | $173070 \pm 888$ | 1/2 | 2/3 |
| | b | $4180 \pm 30$ | 1/2 | -1/3 |

**Table 2.2:** The quarks in the SM [1].

### 2.1.2 Gauge Bosons

The three forces described by the SM are mediated by spin-1 particles, known as gauge bosons. The electromagnetic and weak interactions are propagated by the photon ($\gamma$)

and the $W^{\pm}$ and $Z^0$ bosons, and the strong interaction by the gluon. The photon couples only to charged particles and has no direct interaction with other photons. The other gauge bosons, the Intermediate Vector Bosons (IVBs) i.e. $W^{\pm}$ and $Z^0$ and gluons differ from the photon in that they do interact with themselves, i.e. $Z \rightarrow W^+W^-$.

Within the SM, both lepton and quark numbers are conserved, whereas the numbers of gluons, IVBs, and photons are not. The gauge bosons are listed in Table 2.3.

| Field | Particle | Mass (GeV/c$^2$) | Spin | Q/e |
|---|---|---|---|---|
| Electromagnetic | $\gamma$ | $<1 \times 10^{-27}$ | 1 | 0 |
| Weak Nuclear | $W^{\pm}$ | $80.385 \pm 0.015$ | 1 | $\pm 1$ |
| | Z | $91.1876 \pm 0.0021$ | 1 | 0 |
| Strong Nuclear | g | $< 1 \times 10^{-3}$ | 1 | 0 |
| Higgs | H | $125.9 \pm 0.4$ | 0 | 0 |

**Table 2.3:** The bosons in the SM [1].

## 2.2 Mathematical Framework

The SM treats particles as excitations of relativistic quantum fields. These quantum field theories (QFTs) all have the property that they are locally gauge invariant, and this requirement of gauge invariance leads to the conservation of the charges associated with the particle field.

If a field only has one charge, the gauge invariance is based upon the unitary group $U(1)$, while for fields with $n > 1$ associated charges, the invariance is based upon the group $SU(n)$ [2]. The structure of the SM is given by $SU(3)_C \otimes\ SU(2)_L\ \otimes\ U(1)_Y$. The subscripts $C$, $L$ and $Y$ refer to the quantity conserved in each group, namely the colour charge, weak isospin and weak hypercharge respectively [3]. The groups $SU(2)_L \otimes U(1)_Y$ correspond to the electroweak interaction, a unified theory combining the electromagnetic and weak forces. The group $SU(3)_C$ refers to the gauge field theory which describes the interaction of coloured quarks, as defined by Quantum Chromodynamics (QCD).

A brief description of each of the QFTs related to the fundamental forces is given below.

### 2.2.1 Quantum Electrodynamics

Quantum Electrodynamics (QED) is the QFT which describes electromagnetic interactions. Starting with a free Dirac field, $\Psi(x)$, which describes the behaviour of a fermion with charge $Q$ and mass $m$, whose dynamics are described by the Dirac equation [4]:

$$(i\partial\!\!\!/ - m)\Psi(x) = 0 \tag{2.1}$$

which is derived by applying the Euler-Lagrange equations [5] to its Lagrangian density,

$$\mathcal{L} = \bar{\Psi}(x)(i\partial\!\!\!/ - m)\Psi(x). \tag{2.2}$$

This Lagrangian is invariant under a global U(1) transformation,

$$\Psi(x) \;\rightarrow\; e^{iQ\theta}\Psi(x) \tag{2.3}$$

where $\theta$ is a continuous parameter. However, it is not invariant under a local transformation, where $\theta(x)$ depends on the space-time coordinate, since the partial derivative in Equation (2.2) will transform as:

$$\partial_\mu\Psi(x) \rightarrow \partial_\mu[e^{i\theta(x)}\Psi(x)] = e^{i\theta(x)}(\partial_\mu + i\partial_\mu\theta(x))\Psi(x). \tag{2.4}$$

To maintain local gauge invariance, the introduction of a gauge vector boson field, $A_\mu(x)$, is required, which transforms as [6]

$$A_\mu \rightarrow A_\mu - \frac{1}{e}\partial_\mu\theta. \tag{2.5}$$

Defining the covariant derivative $D_\mu$,

$$D_\mu\Psi(x) = (\partial_\mu - ieQA_\mu)\Psi(x) \tag{2.6}$$

which has transformation properties identical to the field, then:

$$D_\mu\Psi(x) \rightarrow e^{-iQ\theta(x)}D_\mu\Psi(x). \tag{2.7}$$

A gauge invariant kinetic term, the field strength tensor, $F_{\mu\nu}$, may be introduced by

$$F_{\mu\nu}(x) = \partial_\mu A_\nu(x) - \partial_\nu A_\mu(x). \tag{2.8}$$

Adding a vector field $A_\mu(x)$ and a term for $F_{\mu\nu}(x)$ to Equation (2.2), and substituting for $D_\mu$ yields the QED Lagrangian density

$$\mathcal{L}_{QED} = \bar{\Psi}(x)(i\gamma_\mu D^\mu - m)\Psi(x) - \frac{1}{4}F_{\mu\nu}(x)F^{\mu\nu}(x). \tag{2.9}$$

The vector field introduced can be identified as the propagator for the electromagnetic force, and is associated with the photon.

The coupling strength between charged particles and the photon is given by $e$. This is related to the fine structure constant by $\alpha_{em} = e^2/4\pi$. At low energies, $\alpha_{em} \sim 1/137$. An addition of a potential mass term, $\frac{1}{2}m_A^2 A_\mu A^\mu$, to $\mathcal{L}_{QED}$ would violate local gauge invariance, thus the photon must be massless. This prediction is in agreement with the massless photon observed by experiment [1].

### 2.2.2 Quantum Chromodynamics (QCD)

The theory of the strong force, QCD, describes the interaction of quarks and gluons. It is a non-Abelian* gauge theory, based on the $SU(3)_C$ group, which requires eight generators, known as gluons. In analogy to the photon of QED, they are the mediators of the force.

The Lagrangian density for QCD is constructed in a method similar to the QED Lagrangian - it is expressed by:

$$\mathcal{L}_{QCD} = \sum_q \bar{q}(x)(i\gamma_\mu D^\mu - m_q)q(x) - \frac{1}{4}G^\alpha_{\mu\nu}G^{\mu\nu}_\alpha \tag{2.10}$$

where $G^\alpha_{\mu\nu}$ denotes the QCD strength tensor, and is given by

$$G^\alpha_{\mu\nu} = \partial_\mu A^\alpha_\nu(x) - \partial_\nu A^\alpha_\mu(x) + g_s f^{\alpha\beta\gamma} A_{\mu\beta} A_{\nu\gamma} \tag{2.11}$$

where $f^{\alpha\beta\gamma}$ are the structure constants and $A^\alpha_\mu$ represents the different gluon fields, with $\alpha = 1 \rightarrow 8$. The coupling of the strong interactions, $\alpha_s$, can be written as

$$\alpha_s(Q^2) = \frac{g_s^2}{4\pi}. \tag{2.12}$$

*A non-Abelian group is one where the multiplication operator on two elements of the group is not commutative - e.g. $x \times y \neq y \times x$.

Note that $\alpha_s$ varies as a function of energy and is generally quoted at specific energy scales, such as the mass of the $Z^0$ boson.

The strong force is weakest for large $Q^2$ interactions, where $Q^2$ is the momentum transfer between the two colliding partons. At high $Q^2$ partons scatter in a simple way analogously to QED. At low $Q^2$, the force becomes very large and this leads to colour confinement. This manifests itself as the final state containing "dressed" colour neutral hadrons; the process of hadronisation is complex and non-perturbative.

### 2.2.3 Electroweak Theory and Higgs Mechanism

The Electroweak (EW) theory is a unified theory describing both the electromagnetic and weak interactions. It is achieved by requiring that the combined Lagrangian obeys the local gauge invariance provided by the $SU(2)_L \otimes U(1)_Y$ symmetry group. Weak hypercharge, $Y$, is related to the charge $Q$, and the third component of isospin, $I_3$, by the relation [7]

$$Q = I_3 + \frac{Y}{2}. \tag{2.13}$$

Isospin is a fundamental quantum number, and the up-type quarks take values of $I_3 = +1/2$ whereas the down-type quarks take values of $I_3$ = -1/2[†]. A quark cannot weakly decay into a quark with the same $I_3$ value. EW interactions propagate through four gauge fields ($B_\mu$, $W^1_\mu$, $W^2_\mu$, and $W^3_\mu$). $B_\mu$ is required for maintaining invariance under electromagnetic transformations, while the remaining three fields $W^i_\mu$ (for $i$=1,2,3) are required to maintain invariance under weak transformations.

EW theory describes the interactions of left and right handed lepton and quark fields, and purely left handed neutrino fields. In the SM, neutrinos are considered massless and exclusively left-handed. This is known to be inconsistent with experimental observations where neutrinos are required to have mass [8]. It is not understood how neutrino mass is generated nor all the implications of this in terms of new physics (NP).

The weak interaction violates parity i.e. the helicity[‡] $H$ of a fermion is not conserved. This means that left-handed ($H$=-1) and right-handed ($H$=+1) fermions are asymmetric. The Dirac fields of massless fermions can be separated into two constituent components,

[†]The neutrinos take the value of $I_3$=+1/2 and the leptons of $I_3$=-1/2.
[‡]The helicity being the component of a particle's spin in the direction of the particle's motion.

left-handed and right-handed, with each generation of leptons and quarks containing a left-handed doublet, and a right-handed singlet. The left-handed doublets can be represented as

$$\begin{pmatrix} \nu_l \\ l \end{pmatrix}_L, \begin{pmatrix} u \\ d \end{pmatrix}_L$$

where $l$=$e, \mu, \tau$ and $\nu_l$ are the corresponding lepton neutrinos, $u$ represents an 'up' type quark, and $d$ is the 'down' type quark weak eigenstate. The right-handed singlets are represented, similarly, by

$$l_R, u_R, d_R.$$

The simplest form of the EW interaction, through the requirement of gauge invariance, is that its four gauge fields are *massless* spin-1 fields. It should be noted that this is inconsistent with experimental evidence, where only the photon is massless.

The Higgs mechanism is postulated to introduce mass to both a subset of the IVBs and the fermions [9]. This proposes a scalar field, called the Higgs field, which breaks electro-weak symmetry of $SU(2) \times U(1)$ through spontaneous symmetry breaking (SSB). The particle associated with the Higgs field is known as the Higgs Boson.

The Higgs Mechanism for the IVBs relies on an isospin $SU(2)$ doublet, $\Phi$, of complex scalar fields $\Phi^+$ and $\Phi^0$,

$$\Phi = \begin{pmatrix} \Phi^+ \\ \Phi^0 \end{pmatrix} = \begin{pmatrix} \phi^1 + i\phi^2 \\ \phi^3 + i\phi^4 \end{pmatrix}. \tag{2.14}$$

These fields have an associated scalar potential $V(\phi)$ described by:

$$V(\Phi) = \mu^2 \Phi^\dagger \Phi + \lambda (\Phi^\dagger \Phi)^2. \tag{2.15}$$

For the case where $\mu^2 > 0$, this potential has a trivial minima at $\Phi = 0$ corresponding to the vacuum state of the system. However, if $\mu^2 < 0$, the potential has a non-trivial ground state at

$$|\Phi| = \sqrt{\frac{\mu^2}{2\lambda}} = \frac{v}{\sqrt{2}} \tag{2.16}$$

where $v = \mu/\sqrt{\lambda}$ and where $v$ is the vacuum expectation value. A graphical representation of this is given in Figure 2.1.

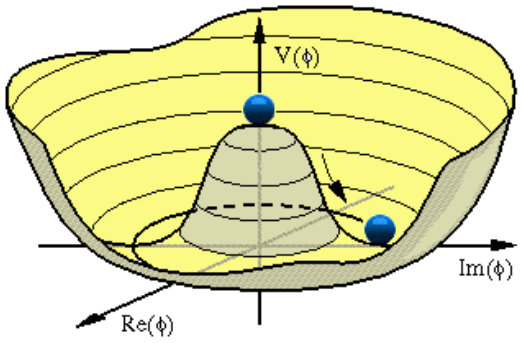


**Figure 2.1:** A diagram demonstrating the non-zero vacuum expectation value of the Higgs field. A minima is indicated in the bottom of the circle, with a blue ball indicating the motion of the spontaneous symmetry breaking. Reproduced from [10].

This ground state has an infinite number of solutions, corresponding to any point on a circle given by

$$|\phi_0|^2 = \frac{(\phi^1 + \phi^2 + \phi^3 + \phi^4)}{2} = \frac{v^2}{2}. \tag{2.17}$$

It is possible to choose the vacuum such that $\phi^1 = \phi^2 = \phi^4 = 0$, which gives, substituting into Equation (2.14),

$$\Phi_{min} = \frac{1}{\sqrt{2}} \begin{pmatrix} 0 \\ v \end{pmatrix}. \tag{2.18}$$

This choice of a particular vacuum is known as the spontaneous symmetry breaking (SSB) of the theory.

The Lagrangian which describes the motion of the doublet in the potential in Equation (2.15) is given by

$$\mathcal{L}_{Higgs} = (D_\mu \Phi)^\dagger - \mu^2 \Phi^\dagger \Phi - \lambda (\Phi^\dagger \Phi)^2. \tag{2.19}$$

From Goldstone's Theorem [11], there is an expectation of four Goldstone bosons associated with Equation (2.17). Three of these bosons are massless, whilst one of them, known as the Higgs Boson, will be massive. A unitary gauge transformation of the field $\phi(x)$ removes the three massless Goldstone bosons which are non-physical and are

associated with the axial/rotational symmetry of the fields. The remaining Goldstone boson, the Higgs particle, is associated with the radial excitation and is physical.

From the implementation of the Higgs field, it is possible to express the observable bosons in terms of the underlying fields:

$$W_\mu^+ = \frac{1}{\sqrt{2}}(W_\mu^1 + iW_\mu^2), \tag{2.20}$$

$$W_\mu^- = \frac{1}{\sqrt{2}}(W_\mu^1 - iW_\mu^2), \tag{2.21}$$

$$\begin{pmatrix} Z_\mu \\ A_\mu \end{pmatrix} = \begin{pmatrix} \cos\theta_W & -\sin\theta_W \\ \sin\theta_W & \cos\theta_W \end{pmatrix} \begin{pmatrix} W_\mu^3 \\ B_\mu \end{pmatrix}. \tag{2.22}$$

The fields $W_\mu^+$, $W_\mu^-$, $Z_\mu$ and $A_\mu$ correspond to the $W^\pm$ and $Z$ bosons, and the photon. The parameter $\theta_W$ is the weak mixing angle, also known as the Weinberg angle [1], and relates the couplings for the electromagnetic field and the weak field through:

$$g\sin\theta_W = g'\cos\theta_W \tag{2.23}$$

where $g$ is the electromagnetic coupling, and $g'$ the weak coupling.

## 2.3 CP Violation and the CKM Matrix

The experimentally observed phenomena of quark mixing is accounted for within the SM by allowing the quark's weak and mass eigenstates to be different. This is described by the Cabibbo-Kobayashi-Maskawa (CKM) matrix [1].

The weak eigenstates of the quarks may be described as a superposition of the mass eigenstates in Equation (2.24), e.g. $s'$ is a superposition of $d$, $s$ and $b$.

$$\begin{pmatrix} d' \\ s' \\ b' \end{pmatrix} = V_{CKM} \begin{pmatrix} d \\ s \\ b \end{pmatrix} = \begin{pmatrix} V_{ud} & V_{us} & V_{ub} \\ V_{cd} & V_{cs} & V_{cb} \\ V_{td} & V_{ts} & V_{tb} \end{pmatrix} \begin{pmatrix} d \\ s \\ b \end{pmatrix}. \tag{2.24}$$

The coupling strengths of the 9 possible quark transitions are provided by the elements of this matrix. For example, $V_{ud}$ provides the amplitude and phase of the charged weak coupling between $u$ and $d$ quarks.

Experimentally, it is observed that the highest coupling strengths occur for transitions within the same generation (e.g. $u \to d, c \to s, t \to b$). In terms of the matrix, the diagonal elements are close to one, and the off-diagonal elements are small.

The current most precise values for the amplitudes of the CKM matrix values are presented below [1]:

$$|V_{CKM}| = \begin{pmatrix} 0.97428 \pm 0.00015 & 0.2253 \pm 0.0007 & 0.00347^{+0.00016}_{-0.00012} \\ 0.2252 \pm 0.0007 & 0.97345^{+0.00015}_{-0.00016} & 0.0410^{+0.0011}_{-0.0007} \\ 0.00862^{+0.00026}_{-0.00020} & 0.0403^{+0.0011}_{-0.0007} & 0.999152^{+0.000030}_{-0.00045} \end{pmatrix}. \tag{2.25}$$

A general $3 \times 3$ matrix can be described with 18 parameters. The unitary nature implies 6 orthogonality and 3 normalisation constraints, which means the number of parameters can be reduced to 9. Five of the phases can be assigned arbitrary values, thus the CKM matrix can be limited to 4 independent parameters [12], three rotation angles and a complex phase. This results in the CKM matrix being rewritten as [1]:

$$V_{CKM} = \begin{pmatrix} c_{12}c_{13} & s_{12}c_{13} & s_{13}e^{-i\delta_{13}} \\ -s_{12}c_{23} - c_{12}s_{23}s_{13}e^{i\delta_{13}} & c_{12}c_{23} - s_{12}s_{23}s_{13}e^{i\delta_{13}} & s_{23}c_{13} \\ s_{12}s_{23} - c_{12}c_{23}s_{13}e^{i\delta_{13}} & -c_{12}s_{23} - s_{12}c_{23}s_{13}e^{i\delta_{13}} & c_{23}c_{13} \end{pmatrix} \tag{2.26}$$

where the terms $s$ and $c$ represent the sines and cosines of the angles denoted by the subscript, such that $s_{12} = \sin\theta_{12}$, and a CP-violating phase $\delta_{13}$.

Only some of the observed phenomena of CP violation[§] can be accounted for via the phase ($e^{-i\delta_{13}}$) introduced in the CKM matrix. The CKM matrix does not describe CP violation in neutrino mixing, nor any strong CP-violating phases and does not provide a complete explanation for the matter asymmetry in universe [13].

CP violation in the weak sector can be demonstrated, for example, by writing down the Lagrangian describing the charged weak transition between an up-type and down-

[§]CP violation is an asymmetry of physics under the CP operation, with C standing for the charge-conjugate operator, and P standing for the parity operation

type quark,

$$\mathcal{L} \propto \bar{u}_i \gamma^\mu V_{ij} d_j W_\mu^- + \bar{d}_i \gamma^\mu V_{ij}^* u_j W_\mu^+. \tag{2.27}$$

Transforming this Lagrangian under the combined CP operation yields,

$$\mathcal{L} \propto \bar{d}_i \gamma^\mu V_{ij} u_j W_\mu^+ + \bar{u}_i \gamma^\mu V_{ij}^* d_j W_\mu^-. \tag{2.28}$$

Since the CKM matrix contains a complex phase, the matrix elements will not necessarily be equal to their complex conjugates i.e. $V_{ij} \neq V_{ij}^*$. The Lagrangian, therefore, can be asymmetric under a CP transformation resulting in a violation of CP symmetry in a process containing one or more amplitudes.

## 2.4 Top Quark

### 2.4.1 Introduction

A two generation SM adequately explained experimental results until the discovery of CP violation in 1964, for which the 1980 Noble Prize in Physics was awarded [14]. With the discovery of CP violation, there were insufficient parameters in the quark mixing matrix to explain this observation. The generalisation to the CKM matrix, in which a complex phase may be introduced, led to searches for the two new postulated quarks, as well as the third generation leptons.

The discovery of a third generation fermion, the tau lepton, was made at SLAC between 1974 and 1977 [15]. Subsequently the bottom quark was discovered in Fermilab in 1977 [16] leaving only the tau neutrino and up-like (top) quark to be found. The tau neutrino discovery followed in 2001 [17].

By 1994, using electroweak constraints, it was possible to predict an approximate mass for the top quark of $\sim$ 175 GeV/c$^2$ [18]. The top quark was experimentally discovered in 1995, by the CDF and D0 experiments at Fermilab [19, 20]. The top quark mass is currently measured to be 173.07 $\pm 0.52 \pm 0.72$ GeV/c$^2$ [1].

The high mass of the top quark gives it the unique property of decaying before any hadronisation [21] can occur. This characteristic means that the top quark provides the only example of a quark that can be studied directly.

### 2.4.2 Production of Top Quark Pairs

The production of top quarks is usually described using Feynman diagrams. Feynman diagrams can be considered as pictorial representations of mathematical expressions governing the behaviour of particles. Lines represent particle currents, and where they meet represents an interaction, and time runs from left to right. These points of intersection are called *vertices*.

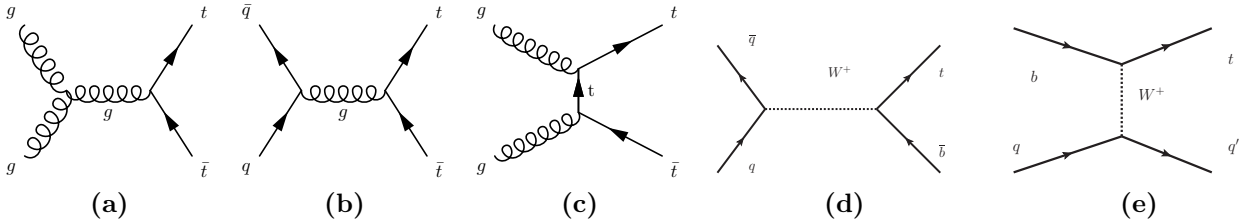


**Figure 2.2:** Leading order Feynman diagrams for $t\bar{t}$ production and single top production at the LHC: (a) gluon fusion, the dominant process at the LHC contributing approximately 85% of the cross-section (b) pair creation from $q\overline{q}$ annihilation (c) $t$-channel gluon fusion for top pair production (d) $s$-channel single top production (e) $t$-channel single top production. $s$-channel production mechanisms join the incoming particles into an intermediate particle which subsequently splits into the outgoing particles, and $t$-channel processes are ones in which an incoming particle emits an intermediate propagator.

A leading order (LO) Feynman diagram represents the simplest diagram possible to produce a final state. Examples of LO Feynman diagrams for $t\bar{t}$ production are presented in Figure 2.2. Next to leading order (NLO) diagrams can then be considered diagrams with extra interactions or vertices. Typical NLO $t\bar{t}$ production diagrams are presented in Figure 2.3.

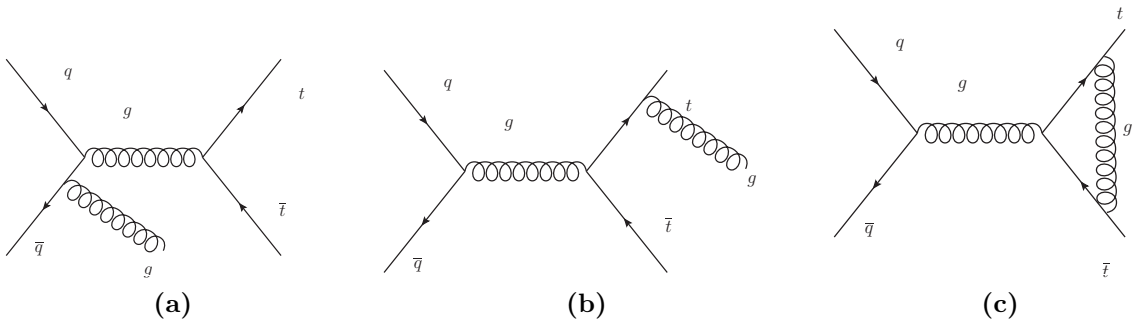


**Figure 2.3:** Some example diagrams of Next to Leading Order production mechanisms for $t\bar{t}$ production.

The diagrams can be read left-to-right for initial to final states. In the example of diagram (a) in Figure 2.2, two gluons from the colliding protons fuse together to create a higher energy gluon which subsequently decays to $t\bar{t}$ pairs. Diagram (a) in Figure 2.3 shows a $q\bar{q}$ annihilation where one of the incident partons undergoes initial state radiation. Each instance of a vertex in a Feynman diagram, for which all the NLO diagrams couple via the strong force, cause a process to be rarer by an order of $\alpha_s$. For example diagram (a) in Figure 2.2 is a diagram whose cross-section is of order $\alpha_s^2$. Diagram (a) in Figure 2.3 has a cross-section of order $\alpha_s^3$, and diagram (c) has a cross-section of order $\alpha_s^4$. This means that, whilst significantly more NLO diagrams can be drawn than LO diagrams, the contribution to the cross-section is generally reduced.

In a proton-proton collider like the LHC, the two incident particles are not simple objects as they would be in an electron-positron collider. The proton has a substructure with three valence quarks and a number of sea partons (quarks, anti-quarks and gluons). The proton momentum, therefore, is split between the valence quarks and the sea partons, so the fraction of momentum carried by a specific type of quark or a gluon has a distribution called a parton distribution function (PDF) which has to be measured.

An example of two colliding protons in a leading order $t\bar{t}$ Feynman diagram is illustrated in Figure 2.4, and a parton density function is given in Figure 2.5. This graph shows the probability of finding a parton of a certain flavour with a fraction of the proton momentum between $x$ and $x+dx$, at an (energy scale)$^2$ of $Q^2$. PDFs are amalgamations of experimental results from a wide range of particle physics experiments, with different PDF collaborations utilising different techniques or fit methods to extract the substructure of the proton.

In particle physics experiments, the process of interest is often the hard scattering. A hard scattering process is one in which there is a high momentum transfer between the colliding particles. The hard process itself can often be treated perturbatively yielding a partonic cross-section[¶] ($\hat{\sigma}$) for two specific incoming partons. This must be folded with the PDFs to calculate a full hadronic cross-section, $\sigma$

$$\sigma = \sum_{ij} \int dx_1 dx_2 f_i(x_1, Q^2) f_j(x_2, Q^2) \hat{\sigma}(x_1, x_2, Q^2) \tag{2.29}$$

[¶]Useful theoretical predictions must be translated into observable quantities such as the cross-section, $\sigma$, for a process. This is measured in units of $\mathrm{m}^{-2}$, and is generally translated into units of barns ($10^{-28}$ $\mathrm{m}^2$). The cross-section is a measure of the rate of production, so a process with $\sigma = 1$ nb is produced at a rate of 1,000,000 times that of a process with $\sigma = 1$ fb.

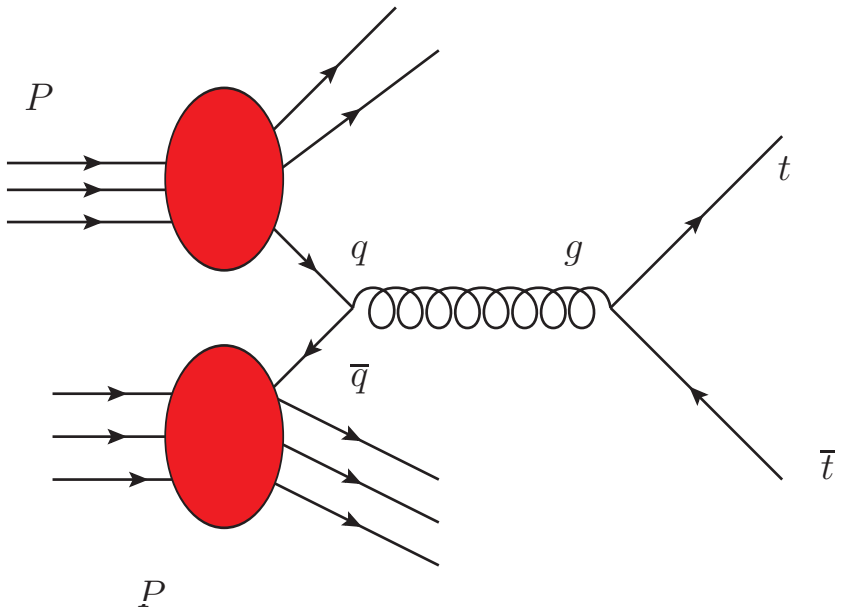


**Figure 2.4:** An illustration of how the hard scattering occurs in a proton-proton colliding experiment, to create top quark pairs.

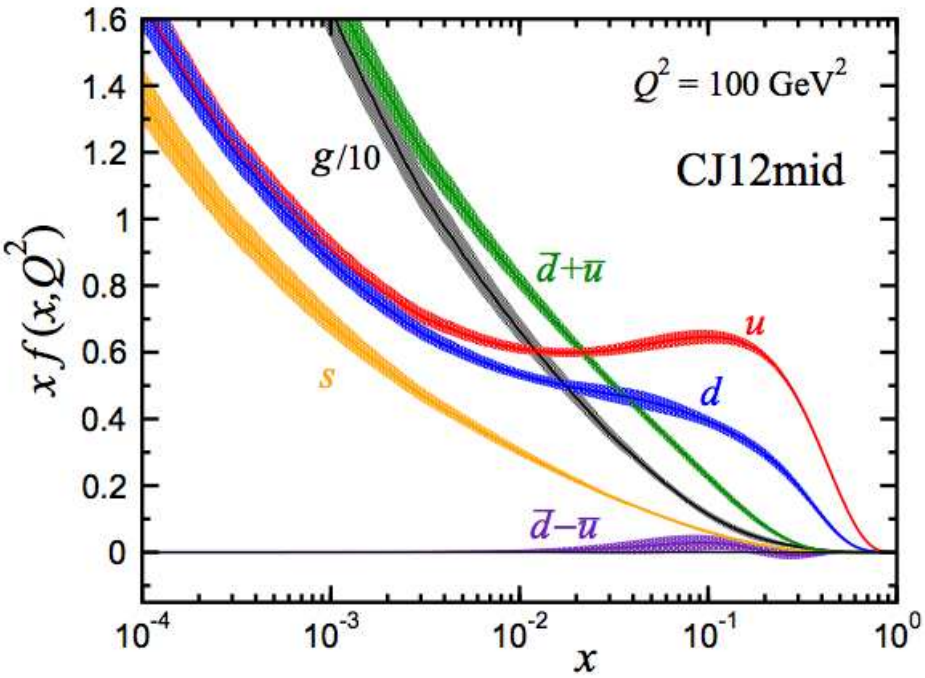


**Figure 2.5:** An example of a parton density function. Uncertainties correspond to the shaded areas around the specific quark content. Reproduced from [22]. The quantity $xf(x, Q^2)$ is the product of the momentum fraction $x$ and the distribution function $f(x, Q^2)$.

which can then be compared to experimental results. This cross-section must be integrated numerically, which can be done using an event generator, as used in Chapter 6. A review on the calculation of the partonic cross-section can be found in [23] or [24].

At a centre of mass energy of $\sqrt{s} = 7$ TeV in the LHC, top pair production occurs with an NNLO calculated cross-section for an assumed mass of $m_t = 173$ GeV [25] of $\sigma = 163^{+7+9}_{-5-9}$ pb. The Feynman diagrams for the leading order production mechanisms for pair production are shown in (a) through (c) of Figure 2.2. At an energy of 8 TeV the top pair production cross-section increases to $\sigma = 234^{+10}_{-7} \pm 12$ pb [26], and at 14 TeV it is $\sigma = 920^{+50+33}_{-39-35}$ pb [25]. An example of an NNLO top pair production diagram is included in Figure 2.6.

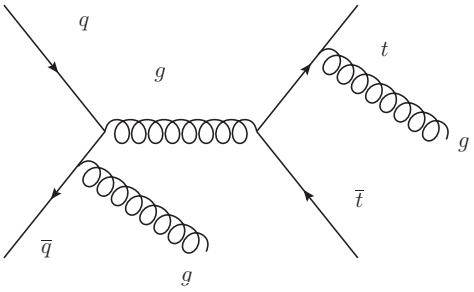


**Figure 2.6:** An example of an NNLO Feynman diagram for $t\bar{t}$ production.

Top (which refers to both top quarks and anti-top quarks) can also be produced singly rather than in pair combinations. Two example diagrams for single top production are shown in Figure 2.2 (d) and (e). Single top production is dominated by a $t$-channel process, and has a cross-section at $\sqrt{s} = 7$ TeV of $\sigma = 41.7^{+1.6}_{-0.2} \pm 0.8$ pb [27], which is substantially smaller than the cross-section for top pair production.

Recent results from ATLAS and CMS on the top pair production cross-section and mass are consistent with predictions and previous measurements respectively [28–31]. The top quark mass has been measured to high precision at the Tevatron, and studies are on-going at the LHC [32]. A cross-experiment combination for the top mass is presented in Figure 2.7. The cross-section in the central region at the LHC has already been well measured and the $\sqrt{s} = 7$ TeV results are systematically limited after 0.7→1.1 fb$^{-1}$. The combination of the LHC results is illustrated in Figure 2.8.

More recent measurements from ATLAS and CMS incorporating $\sqrt{s} = 8$ TeV data samples also produce results consistent with SM expectations [35–37]. The results are limited to $\sim 14\%$ precision from systematic uncertainties.

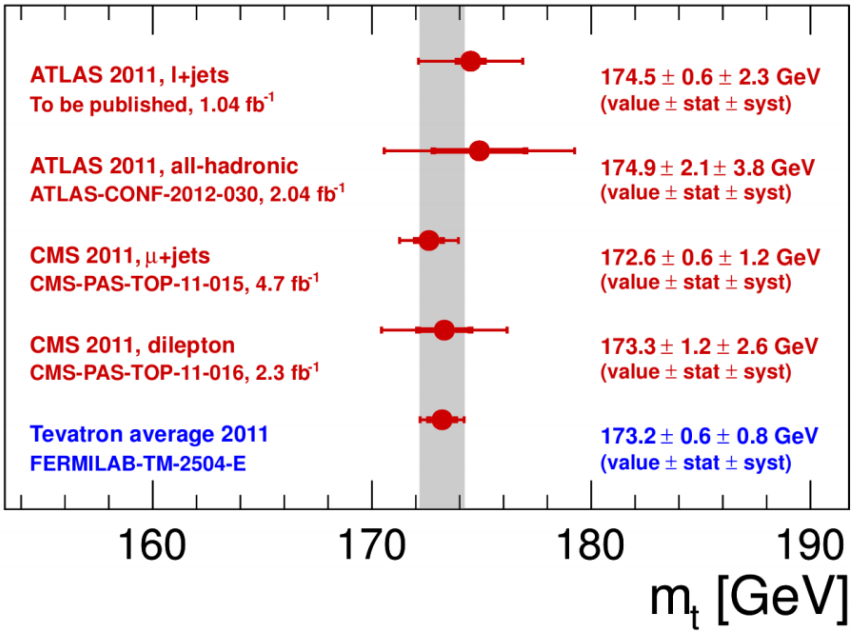


**Figure 2.7:** A combined top quark direct mass measurement from the Tevatron and the LHC. Reproduced from [33].

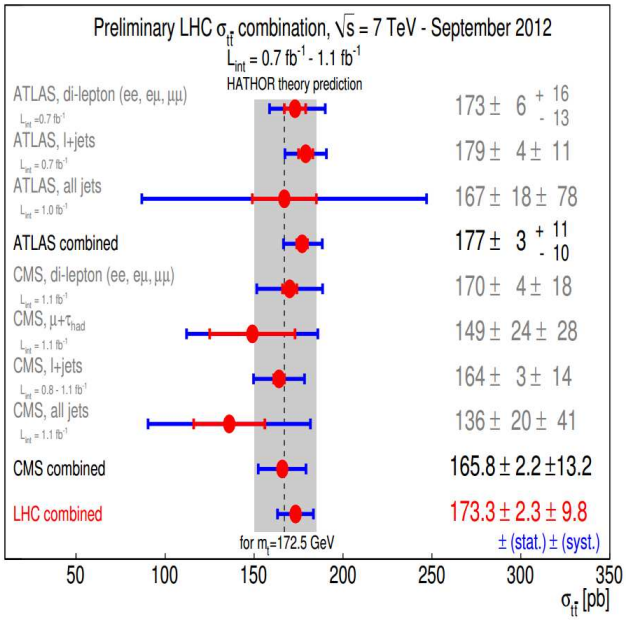


**Figure 2.8:** Top pair production cross-section at CMS and ATLAS. Reproduced from [34].

### 2.4.3 Decay Properties of the Top Quark

The decay width of the top quark can be calculated to be $\sim$ 1.29 GeV/c$^2$ [38]. This corresponds to a lifetime of $\sim$ 0.5 $\times$ $10^{-24}$ seconds. With a decay width of $\Gamma_t > \Lambda_{QCD}$, where $\Lambda_{QCD}$, the QCD scale, is typically on the order of $\sim$ 200 MeV for these interactions, top will decay before hadronising into $Q\overline{Q}$ quarkonium states. A more detailed discussion on the calculations to derive the top decay width, the hadronisation scale, and the respective lifetimes can be found in [21, 38, 39].

In 99.9% of cases [1], the top quark will decay to a bottom quark and a $W$ boson, as given by the $V_{tb}$ term of the CKM matrix. The $W$ bosons subsequently decay (67%) to $q\bar{q}$ pairs, and (33%) to lepton + neutrino states. Thus a $t\bar{t}$ pair can decay into a range of states, from 2 $b$-jets and 4 jets to 2 charged leptons and 2 $b$-jets. A $b$-jet is a jet of particles originating from the hadronisation of a high energy $b$-quark. The former is known as the *all-hadronic* channel, and the latter as the *dilepton* channel. Note that the decays of the $W$ boson to taus are more complicated to classify than that of muons or electrons. The tau lepton decays to $\mu$ or e leptons in $\sim$35% of the time, with the remaining 65% being hadronic decays [1]. This property means that tau lepton decay modes of the $W$ boson are sometimes considered as hadronic channels. A graphical representation of the combined top quark pair decay channels is presented in Figure 2.9.

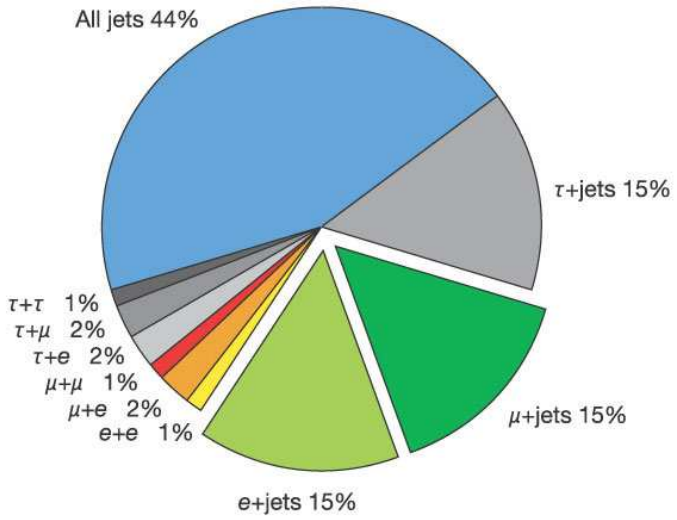


**Figure 2.9:** The different branching ratios of a top pair. This plot refers to the decay modes of the two $W$ bosons arising from top quark decays. This plot is reproduced from [40].

### 2.4.4 Asymmetry

An important quantity that can be analysed in the top quark sector at the LHC is the distribution in pseudorapidity[‖] of the top quark versus its anti-matter partner. The asymmetry causes a difference in these distributions, which themselves relate to parton level differences between the two collding partons. As such, no asymmetry exists in a $gg$ initial state, but is instead manifested in $q\bar{q}$ collisions and $qg$, and $\bar{q}g$, initial states.

The asymmetry can be written as [41]

$$A_{FB} = \frac{N_t(\cos\theta \geq 0) - N_{\bar{t}}(\cos\theta \geq 0)}{N_t(\cos\theta \geq 0) + N_{\bar{t}}(\cos\theta \geq 0)}$$

which can be qualitatively described as the number of top quarks in the forward region compared to the number of anti-top quarks.

The physical asymmetry originates from NLO and higher order diagrams. In a leading order diagram, the exchange of $t$ and $\bar{t}$ quarks is an entirely symmetric mechanism. In the process of a leading order $q\bar{q}$ diagram, as well as gluon fusion diagrams, no asymmetry is calculated. The NLO manifestation has two different origins, the first is radiative corrections to $q\bar{q}$ annihilation diagrams, and the second is interference between different amplitudes in the $qg \to t\bar{t}q$ and $\bar{q}g \to t\bar{t}\bar{q}$ processes [42]. Contributing diagrams towards the charge asymmetry can be found in Figure 2.10, where for example, final state and initial state gluon radiation interfere.

A rapidity-dependent asymmetry analysis from CDF yields results of [41]:

$$A_{FB}(|\Delta y| > 1.0) = 0.611 \pm 0.256$$
$$A_{FB}(|\Delta y| < 1.0) = 0.026 \pm 0.104 \pm 0.0506$$

in comparison to SM predictions of:

$$A_{FB}(|\Delta y| > 1.0) = 0.123 \pm 0.018$$
$$A_{FB}(|\Delta y| < 1.0) = 0.039 \pm 0.006.$$

[‖] Pseudorapidity is an experimental observable which can be considered to be a measure of the particle's direction of travel with respect to the beam axis. It is $\eta = -ln\left(\tan\frac{\theta}{2}\right)$ and can be shown to be equivalent to $y = \frac{1}{2}ln\left(\frac{E+p_z}{E-p_z}\right)$ in the limit of $m \to 0$ using the identity $tan^2\theta = \frac{1-\cos(2\theta)}{1+\cos(2\theta)}$.

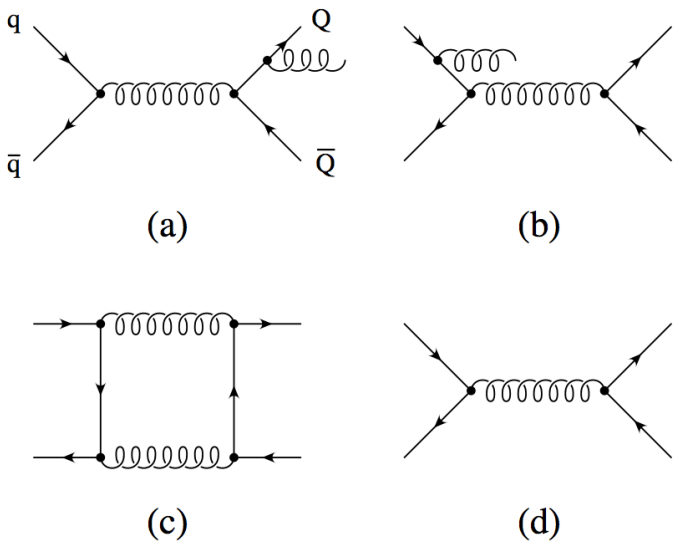


**Figure 2.10:** The diagrams which contribute towards the QCD charge asymmetry. Interference between diagrams (a) (final-state) and (b) (initial-state) gluon radiation, and interference of double virtual gluon exchange (c) with the leading order $q\bar{q}$ diagram (d). Reproduced from [42].

A summary plot of the Tevatron asymmetry results is presented in Figure 2.11. Two potential Beyond Standard Model explanations for anomalous asymmetry measurements are elaborated upon in [43, 44], where a $Z'$ boson could contribute marginally to the cross-section, but provides a significant change in the distribution of the top quarks.

Further observations from the Tevatron include a mass-dependent forward-backward asymmetry, with a result of $A_{FB}^{t\bar{t}}(M_{t\bar{t}} > 450\ \mathrm{GeV/c^2}) = 0.475 \pm 0.112$ in comparison to a SM prediction of $0.088 \pm 0.013$, or a $3.5\sigma$ deviation [41]. It is also possible to perform a measurement based on the charge of the lepton, in which D0 observe a result of $A_{FB}^{l} = (15.2 \pm 4.0)\%$ in comparison to an MC@NLO generator prediction of $(2.1 \pm 0.1)\%$ [45].

The top asymmetry measurement at the LHC is a difficult measurement to make, despite the significantly larger cross-section. At the LHC, the direction of the colliding quark is harder to determine due to the symmetry of the proton-proton collisions compared to the Tevatron with proton-antiproton collisions, in which the colliding quark direction is taken to be a valence quark from the proton. This coupled with the significantly increased proportion of events produced by gluon fusion generally make the LHC a challenging environment for a top asymmetry study, in contrast to the Tevatron where proton-antiproton collisions result in $q\bar{q}$ annihilation providing the dominant process.

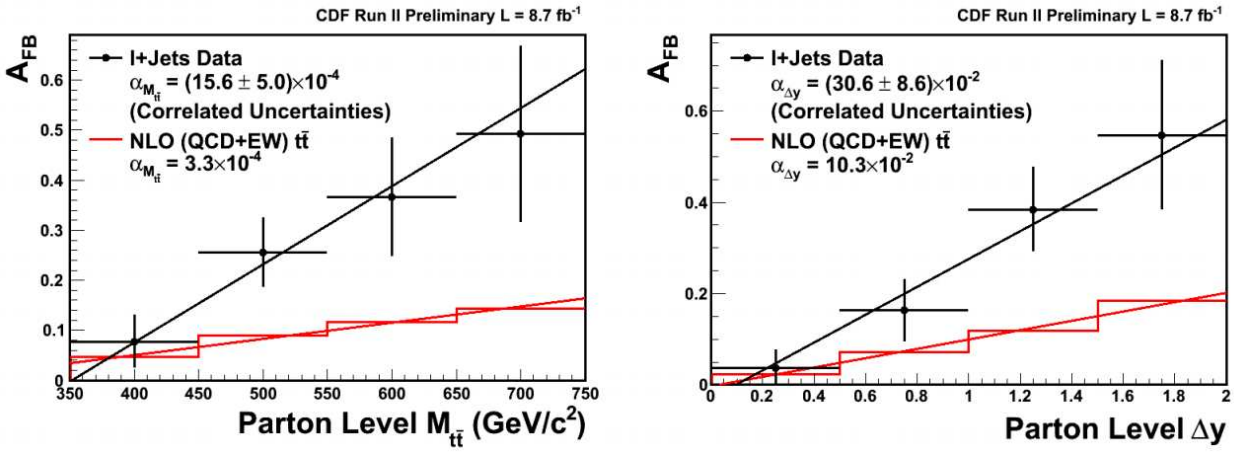


**Figure 2.11:** Tevatron top asymmetry results. Reproduced from [46].

However, for the LHCb experiment the high pseudorapidity coverage yields an increased purity of $q\bar{q}$ events with respect to the symmetric $gg$ fusion events, as can be seen in Figure 2.12 and Figure 2.13.

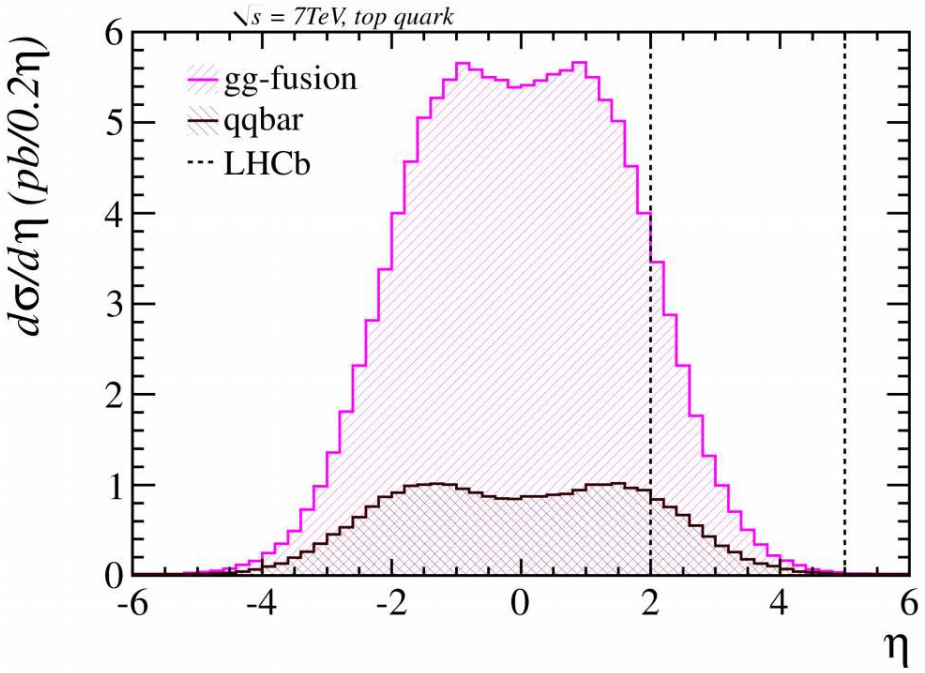


**Figure 2.12:** The two dominant production mechanisms of top quark pairs as a function of pseudorapidity. Reproduced from [47].

At the LHC, the incident quark direction is tagged from the outgoing top quark direction, with the top quark preferentially being in the same direction as the incoming

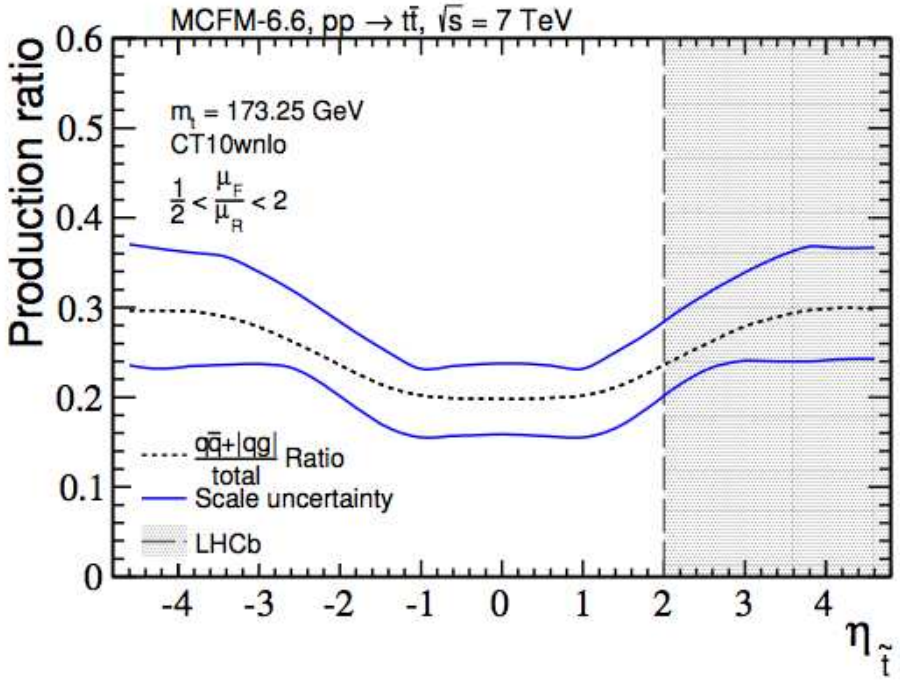


**Figure 2.13:** The ratio of top quark pairs produced by $q\bar{q}$ annihilation versus gluon fusion as a function of pseudorapidity. Reproduced from [48].

quark [49]. Together with the fraction of the momentum carried by the colliding valence quarks being on average larger when compared to the sea antiquarks, this results in top quarks being produced at higher $\eta$ than anti-top quarks [50]. This is illustrated in Figure 2.14, in contrast to the Tevatron distribution which is illustrated in Figure 2.15.

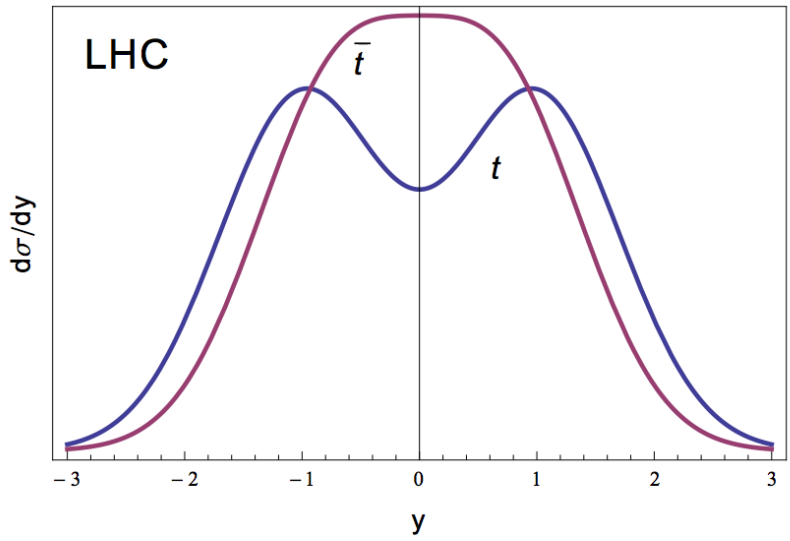


**Figure 2.14:** The rapidity distributions for top (blue) and anti-top (red) quarks at the LHC. Reproduced from [51].

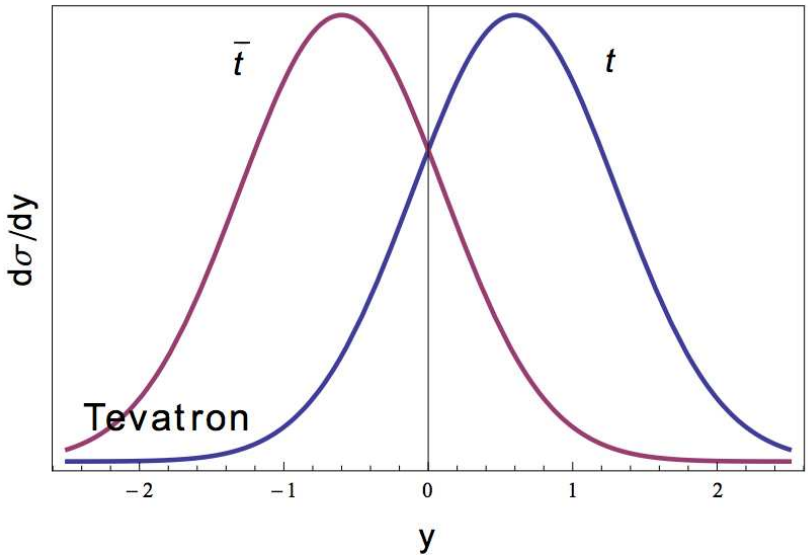


**Figure 2.15:** The rapidity distributions for top (blue) and anti-top (red) quarks at the Tevatron. Reproduced from [51].

ATLAS have performed a measurement [52] of

$$A_C \;=\; 0.029 \;\pm\; 0.018 \text{ (stat.)} \;\pm\; 0.014\text{(syst.)}$$

which is consistent with the SM expectations at the LHC, and has systematic uncertainties comparable to the statistical ones, where $A_C$ is defined as [53, 54]:

$$A_C = \frac{N(\Delta|y| > 0) - N(\Delta|y| < 0)}{N(\Delta|y| > 0) + N(\Delta|y| < 0)}$$

where

$$\Delta|y| = |y_t| - |y_{\bar{t}}|.$$

At LHCb, the top asymmetry is a unique measurement, given the forward region coverage of the detector, in contrast to ATLAS and CMS which typically go up to $\sim|\eta| < 2.5$. The geometry of the detector yields a higher probability of assigning the correct colliding parton charge to the outgoing top, and thus offers a potential advantage over the General Purpose Detectors (GPDs) for this measurement [55].

### 2.4.5 Summary

The study of the top quark in the forward region at LHCb presents another opportunity to observe NP at the LHC. Key measurements offer crucial insights into BSM physics, such as a measurement of the $t\bar{t}$ differential cross-section, or through measurements such as the production asymmetry in the forwards direction. A vital first step is a cross-section measurement which is discussed in Chapter 6, which could lead to an expanded sector of $t\bar{t}$ measurements in an unexplored region of phase space at the LHC.

# Chapter 3

# The LHCb Experiment

## 3.1 The LHC

The Large Hadron Collider (LHC) [56] is a proton-proton collider built by the European Centre for Nuclear Research (CERN) in Geneva, Switzerland. The LHC is housed in a 27 km circumference ring approximately 100 metres underground, on the Franco-Swiss border. A schematic diagram of the LHC ring is shown in Figure 3.1. The LHC design specification is to collide two counter-rotating beams of protons at a centre of mass energy of 14 TeV, with a design luminosity of $10^{34}$ cm$^2$s$^{-1}$ [56]. Further parameters of the machine are detailed in Table 3.1. Due to a fault in the system discovered in 2010, the LHC has only been able to operate at lower beam energies than nominal; the protons were accelerated to 3.5 TeV in 2010 and 2011, and 4 TeV in 2012. After the 2013/2014 shutdown it is expected that the machine will be able to operate at the design specification of 7 TeV per proton beam.

### 3.1.1 Accelerator System

The LHC consists of a series of superconducting dipole magnets and RF cavities. The beams are focused using a series of quadrupole magnets. It uses 8.4 T superconducting dipole magnets to maintain the proton trajectories. In its nominal configuration, it will be able to inject 2808 proton bunches separated in time by 25 ns between bunches. To achieve the performance, the LHC relies on a series of smaller accelerators to take the protons from low energies to the LHC injection energy of 450 GeV.

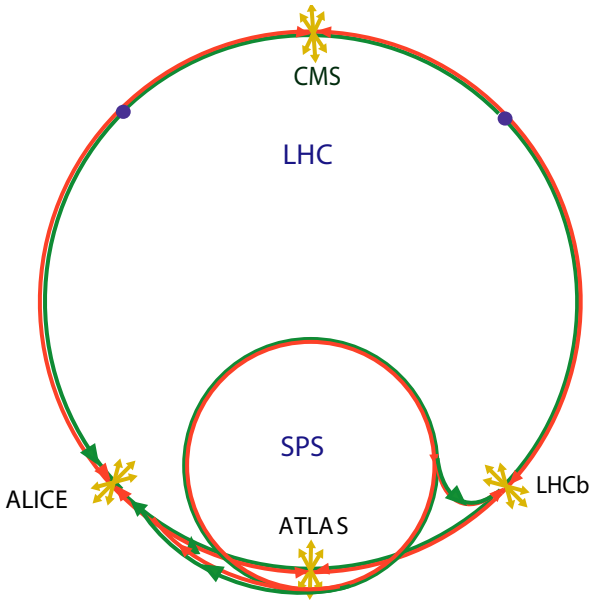


**Figure 3.1:** The LHC ring, with the SPS injection system shown as well as the four collision points comprising the four experiments.

| Parameter | Value |
|---|---|
| Circumference | 27 km |
| Proton energy at collision | 3.5 TeV |
| Centre of mass energy | 7 TeV |
| Circulating beam current | 0.58 A |
| Luminosity | $10^{34}$ cm$^2$s$^{-1}$ |
| Number of bunches | 2808 |
| Number of particles per bunch | $1.5 \times 10^{11}$ |
| Bunch length | 7.5 cm |
| Time between beam crossings | 25 ns |
| Luminosity at LHCb | $2 \times 10^{32}$ cm$^2$s$^{-1}$ |
| Beam size at LHCb | 70 $\mu$m |
| Crossing angle at LHCb | 200 $\mu$rad |

**Table 3.1:** The main design parameters of the LHC, and LHCb specific aspects at point 8 on the LHC ring [56].

The injection chain starts from the LINAC (LINear particle ACcelerator), which accelerates the protons to an energy of 50 MeV, and then injects them into the Proton Synchrotron (PS), which boosts them to 26 GeV. This is followed by injection into the Super Proton Synchrotron (SPS), which takes the protons to the injection energy of 450 GeV after which they are injected into the LHC itself and accelerated to their full energy. This is illustrated in Figure 3.2.

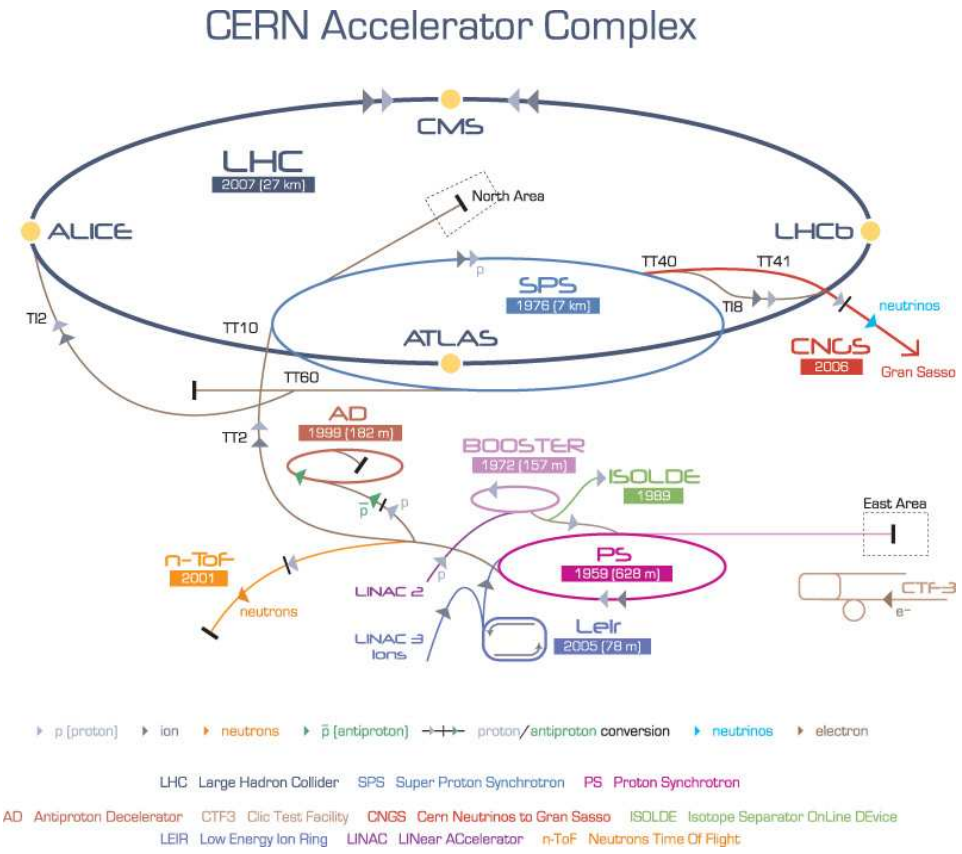


**Figure 3.2:** The injection system for the LHC. Reproduced from [57].

### 3.1.2 The Experiments and Luminosity Levelling

The LHC is designed to provide the highest centre of mass energy proton collisions yet achieved in the laboratory. For full exploitation of the accelerator, there are four experiments, each one corresponding to a different collision point along the LHC ring: ATLAS [58], CMS [59], ALICE [60] and LHCb [61]. The first two experiments are general purpose detectors (GPDs), designed to search for NP beyond the SM and one of the last crucial pieces of the SM, the Higgs Boson. ALICE is dedicated to heavy ion collisions.

In contrast to the two GPDs, LHCb is an experiment that offers precision measurements in the flavour sector, such as CP violation or rare decays.

A measurement of data taking is the total luminosity delivered. The instantaneous luminosity, $\mathcal{L}$, is defined by the following equation, where $\sigma$ is the cross section for a given process, and $R$ is the event rate.

$$\mathcal{L} \times \sigma = R. \tag{3.1}$$

The total number of events produced in an experiment, $N$, therefore is a function of the total luminosity delivered, which itself is the integral of the instantaneous luminosity.

$$N = \sigma \times \int_0^t \mathcal{L} dt. \tag{3.2}$$

The instantaneous luminosity is often expressed as a product of beam parameters [62]

$$\mathcal{L} = f \frac{N_b^2}{4\pi\sigma_x\sigma_y} \tag{3.3}$$

where $f$ is the bunch collision frequency, the value $N_b$ is the number of particles in the bunches of each beam, and $\sigma_{x,y}$ describe the transverse beam profiles in the $x$ and $y$ planes corresponding to the horizontal and vertical planes. Once the total luminosity of a data sample is known, and the number of signal events is established, the cross section of the process can be determined.

The detection of NP, which has, almost by definition, a low cross-section, may be made by direct or indirect means [63]. Broadly the GPDs rely on direct observation of NP through the creation and detection of new states. LHCb uses indirect techniques, including what is sometimes called "quantum interferometry" (time dependent CP violation) to study SM processes with great precision. Higher order processes in $B$-decays, involving new particles beyond the threshold for observation using direct techniques at GPDs, can have large measurable influence on SM processes, such as the $B_s \to \mu\mu$ branching ratio [64]. The low cross-section NP processes place the constraint that the GPD experiments must receive very high levels of luminosity, with multiple collisions per event.

For ATLAS and CMS to acquire the high luminosities they require, the LHC must deliver a large number of average collisions per bunch crossing ($\mu$). The increased number

of collisions, which is also known as pile up, makes reconstruction more difficult, and would cause specific problems for LHCb which is designed as a precision experiment.

The design operating condition for LHCb is to have $\mu \sim 1$. The experiment, from this requirement, must run at lower luminosity than ATLAS or CMS; this is achieved by offsetting the colliding beams in order to reduce the probability of collision. Using a dynamic offset, LHCb can maintain a constant instantaneous luminosity over the course of a fill, whereas ATLAS and CMS both have decaying instantaneous luminosities; this process is known as "luminosity levelling". The luminosity levelling is achieved by using magnets to induce a crossing angle, and displace the beams.

A beneficial feature of luminosity levelling is that LHCb can create Monte Carlo samples with a fixed pile-up and does not have to correct or allow for the time, relative to stable beams being established, of the event. This is an important ingredient in the operation of LHCb as a precision experiment. An example of the luminosity levelling is presented in Figure 3.3 and the total accumulated data for 2011 is presented in Figure 3.4.

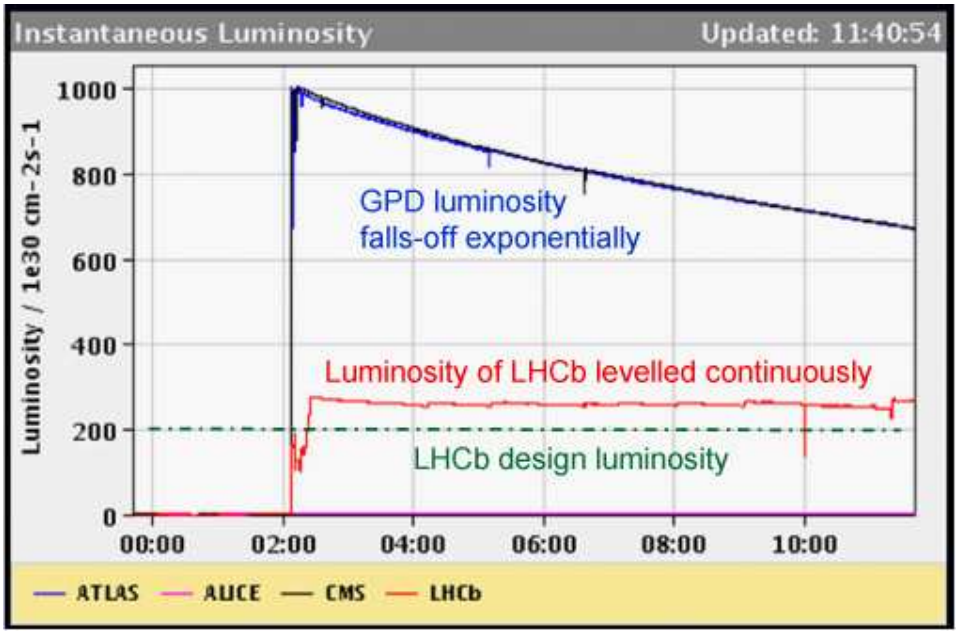


**Figure 3.3:** An example of the decaying luminosity for the GPDs versus the flat luminosity for LHCb in a particular run. Reproduced from [65].

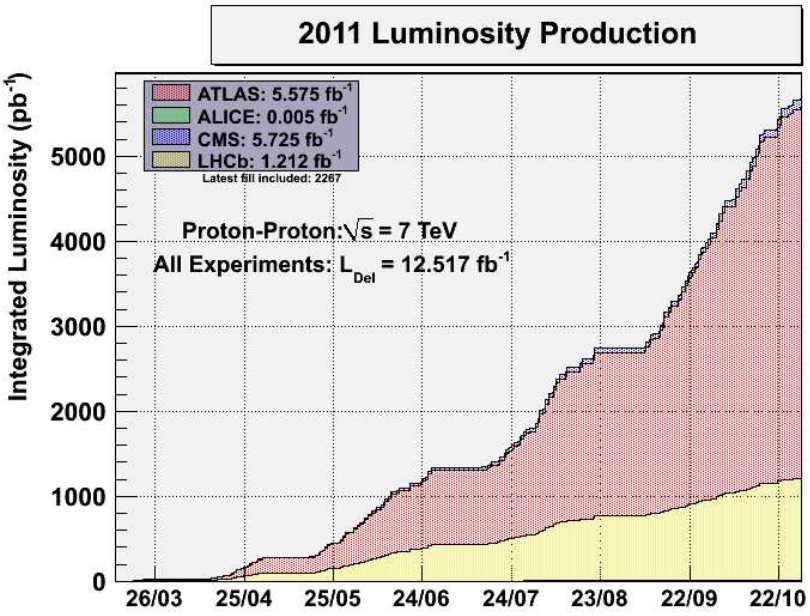


**Figure 3.4:** The total integrated luminosity for the LHC experiments in 2011. The effects of LHCb's luminosity levelling can be observed in having less acquired data than the GPDs. Reproduced from [65].

## 3.2 The LHCb Detector

### 3.2.1 Overview

LHCb is a forward-arm spectrometer*, aiming to make precision measurements of particles within its active aperture. The choice of acceptance lies in the production of $b\bar{b}$ pairs, which are typically produced in either the forward or backward region close to the beam line as illustrated in Figure 3.5. The detector is built to cover one of the regions where pairs are produced in significant quantity. It is in principle possible to build a two-arm spectrometer with a forwards and backwards component, doubling the acceptance for the correlated $b\bar{b}$ pairs, but this would significantly increase the detector and civil engineering costs to the point that the experiment would not be financially viable. The $b\bar{b}$ cross-section into the fiducial volume is approximately 500 $\mu$b at 14 TeV, amounting to approximately $10^{12}$ $b\bar{b}$ pairs per 2 fb$^{-1}$.

*Note that there are VELO and Pile Up stations behind the nominal interaction point used for event vetoing and to allow for the spread of the interaction point to $\sim$10 cm.

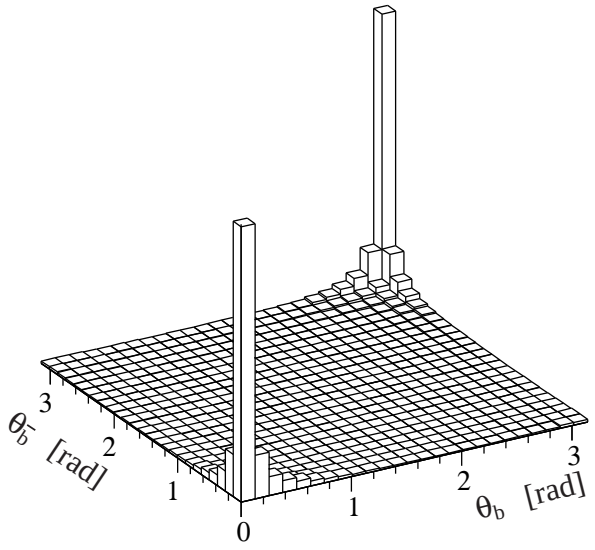


**Figure 3.5:** The polar angle distribution of the $b\bar{b}$ pairs produced at a centre of mass energy of 14 TeV as generated by the PYTHIA event generator [66]. Reproduced from [67].

Bottom quark pair production from proton-proton collisions may occur through several mechanisms. Figure 3.6 shows two of the main production diagrams. The primary mechanism is gluon fusion, where a gluon from each of the colliding protons interacts. Quark anti-quark annihilation will also contribute as well as higher order processes such as flavour excitation and gluon splitting as shown in Figure 3.7.

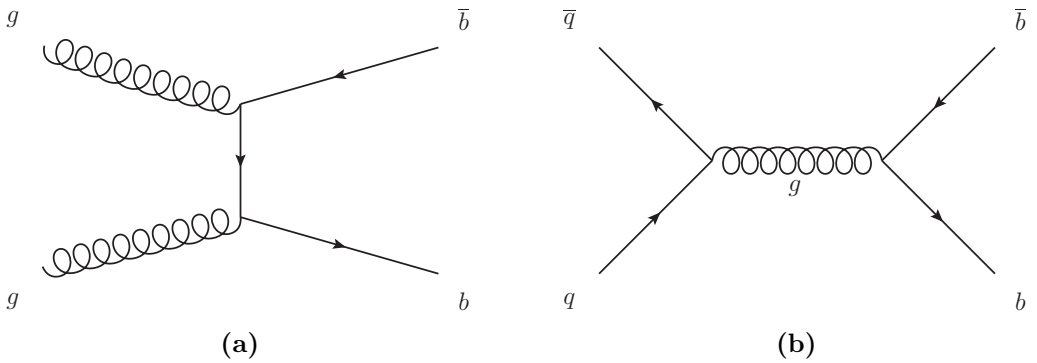


**Figure 3.6:** Leading order Feynman processes for $b\bar{b}$ production. (a) gluon fusion and (b) pair creation from $q\bar{q}$.

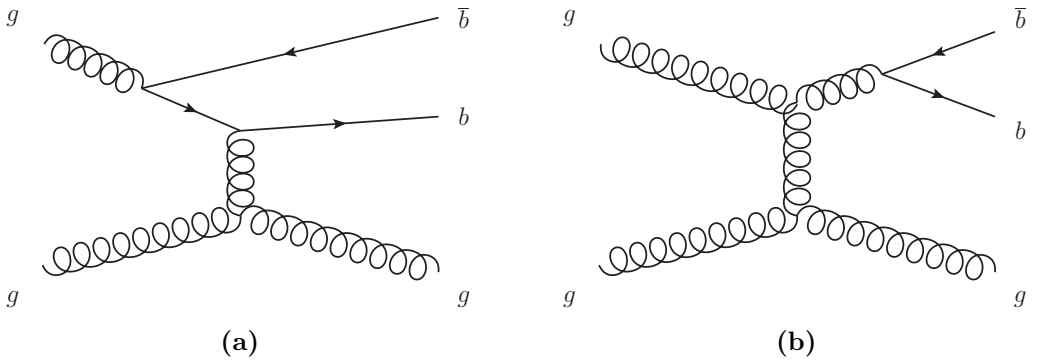


**Figure 3.7:** Next to leading order Feynman processes for $b\bar{b}$ production. Examples of flavour excitation (a) and gluon splitting (b) are shown.

LHCb, see Figure 3.8, has an angular acceptance of $\pm 250$ mrad in the $yz$ plane, and $\pm 300$ mrad in the $xz$ plane[†]. The collisions occur at approximately $z$=0, shown on the left hand side of the Figure 3.8. This region, known as the Interaction Point (IP), is surrounded by the VErtex LOcator (or VELO) which measures the direction of charged particles. Downstream in increasing $+z$ is the first RICH station, which along with RICH2 is used to determine the velocity of particles, which can then be used to distinguish the mass of the particle. After the RICH1 station is the Tracker Turicensis (TT), which is before the magnet. After the magnet is the Silicon Tracker (ST), which is placed before RICH2. After RICH2 are the calorimeter and muon systems, which extend from $z$=12 m onwards. These systems will be described in detail subsequently.

LHCb was designed to read out events at a rate of 40 MHz, corresponding to the nominal bunch spacing inside the LHC. At LHCb, the ability to store data is limited by the capacity of the Grid network. Therefore, it is necessary to discard events that are not of significant interest such as elastic scattering, or light jet production, and these are normally discarded in favour of storing events containing selected channels. Relevant details of the triggering mechanism are discussed in Section 5.2.

[†]The coordinate system used in LHCb is with positive $z$ along the direction of the beam line away from the interaction point into the detector, positive $y$ towards the surface, and positive $x$ to the right hand side if faced down the beam pipe looking into the detector with the VELO first, where $(0, 0, 0)$ corresponds to approximately the interaction point. The $+x$ direction is towards the centre of the ring.

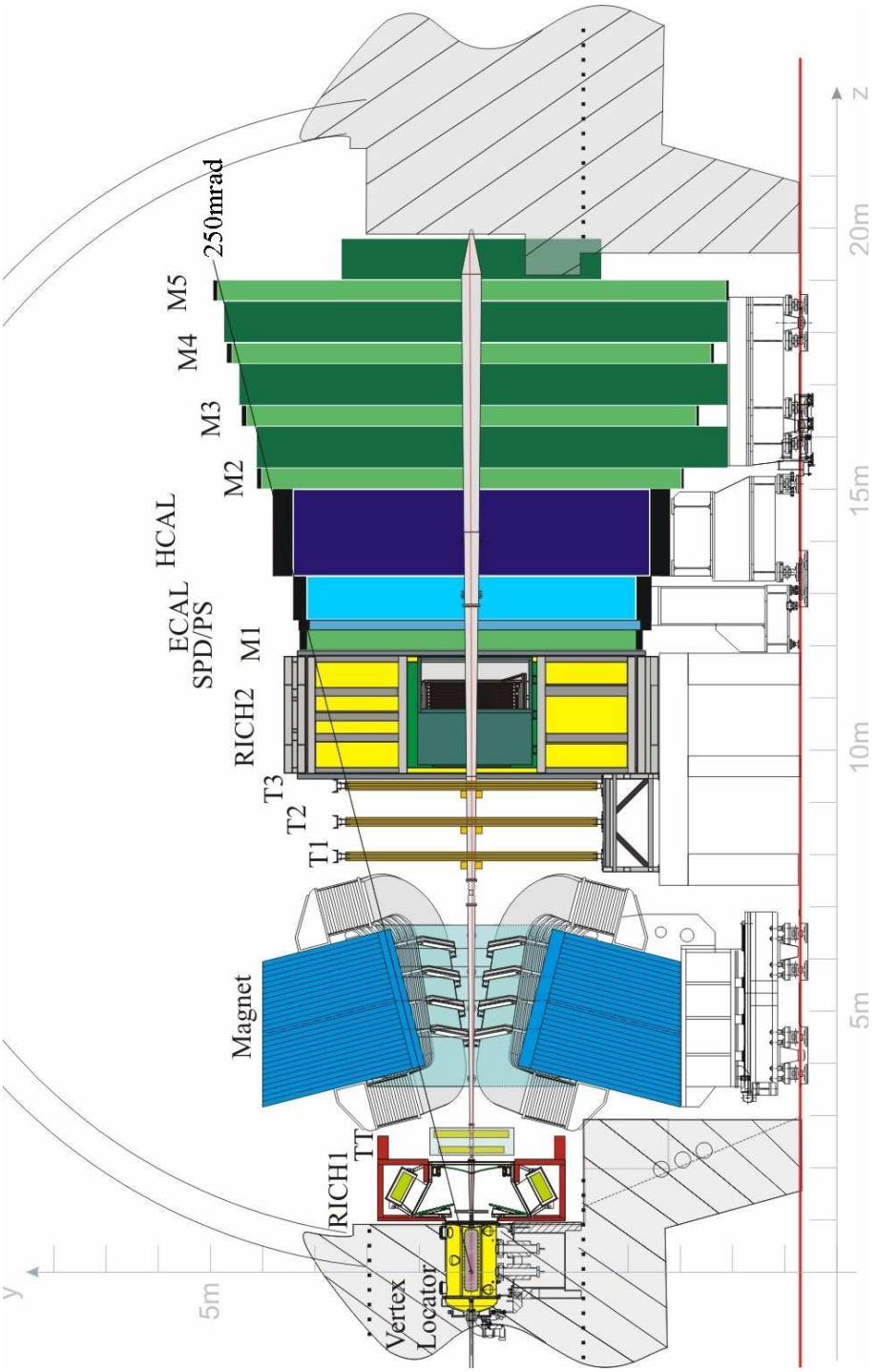


**Figure 3.8:** A cross section of the LHCb experiment in the $y - z$ plane. The interaction point is located inside the VELO, and the individual sub-detectors are labelled.

### 3.2.2 The Tracking Systems

Tracking systems are designed to make precision measurements of charged particles such as particle momentum, or primary vertex assignment, utilising the energy deposition of charged particles through material. The basic principles, and the silicon-specific aspects, are discussed in depth in Chapter 4. The tracking system in LHCb comprises the VELO, the Magnet [68], TT stations and the 3 T stations (T1, T2, T3) [61, 69, 70]. Each T station consists of an IT and OT sub-detector, which employ silicon strips and straw technology respectively. It is important the tracking detectors interact with the incident particles as little as possible, to provide the best possible reconstruction of the track parameters. Substantial effort was invested in reducing the radiation length in each of these sub-systems. For the definition of a radiation length, see the section on the calorimeters later in the chapter.

Tracks can then be extrapolated to hits in the RICH, calorimeters and muon stations to identify the type of particle. The track finding method and particle identification techniques employed in LHCb are documented further in Chapter 5. The important parameters of the tracking systems are summarised in Table 3.2.

| System | Design | $z$ position (m) | Resolution ($\mu$m) | Purpose |
|---|---|---|---|---|
| VELO | Silicon Strips | -0.2 $\rightarrow$ 0.8 | >4 | Tracking and Vertexing |
| TT | Silicon Strips | +2.33 $\rightarrow$ +2.63 | $\sim$ 50 | Triggering |
| IT | Silicon strips | $\sim$ 7.8 $\rightarrow$ 9.4 | $\sim$ 50 | High $\eta$ tracking |
| OT | Straws | $\sim$ 7.8 $\rightarrow$ 9.4 | $\sim$ 200 | Outer region tracking |

**Table 3.2:** A summary table of the key characteristics of the LHCb tracking sub-systems.

#### VELO

The VELO is a silicon strip tracking detector covering the interaction region in LHCb. It is the primary vertexing and tracking detector of the experiment. Tracks reconstructed in this detector are straight as no magnetic field is applied in the volume of the VELO, with only a small stray contribution from the LHCb magnet. A schematic diagram of the VELO is shown in Figure 3.9. The relevant aspects of the VELO for the radiation damage monitoring scheme presented in Chapter 4 will be discussed in depth.

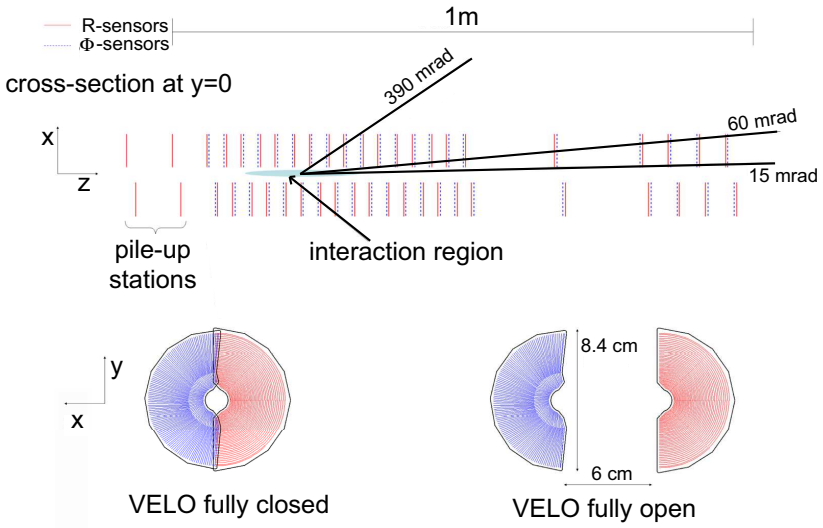


**Figure 3.9:** A diagram of the VELO station in the $xz$ plane, indicating the angular acceptance and the arrangement of the stations. The diagram below shows a VELO station in both the open, and closed, position in the $xy$ plane. Reproduced from [61].

*Geometry:* The VELO consists of 21 stations positioned along the $z$ axis. Each station consists of two modules which are centred around, and perpendicular to, the beam axis approximately forming a disc. The choice of silicon technology for the modules was made for the signal-to-noise ratio achievable, resistance to radiation damage and low mass. The silicon sensors, in the *closed* position, at their nearest point are 8 mm from the beams. The proximity of the innermost active elements of the sensors are designed to minimise the extrapolation distance of the track to the primary vertex, and the associated extrapolation uncertainties, for increased precision. During injection, variations in the beam positions and widths are much larger than when the beams are being used for physics collisions. This imposes the requirement that the VELO has the ability to retract itself into a safer (open) position 30 mm away from the beam axis during injection and other non-stable beam states.

The modules measure 2D spatial points, combining $r$ and $\phi$ measurements with the third $z$ coordinate established by alignment, to allow reconstruction of 3D tracks. A photograph of several VELO modules in one half is shown in Figure 3.10. The VELO

contributes an average of 16.2% of a radiation length for tracks [71], and a full schematic plot of the material budget as a function of $\eta$ and $\phi$[‡] is presented in Figure 3.11.

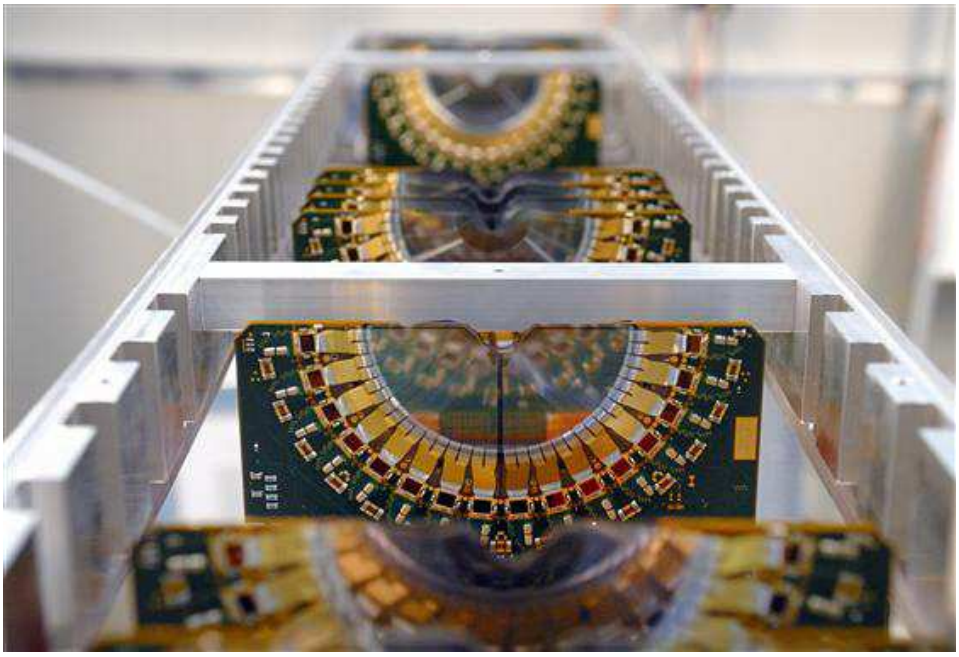

**Figure 3.10:** A photograph of several VELO modules, forming one half of the installed detector. Reproduced from [72].

*Sensors:* The VELO sensors [73] are single sided 300 $\mu$m thick silicon sensors with a semi-circular shape covering approximately 182°. There are two differing types of sensors; the R sensors, which provide radial measurements and the $\Phi$ sensors which provide azimuthal angular information. A sketch illustrating the VELO layout is shown in Figure 3.12. The R sensors contain four 45° segments, each containing 512 concentric circular strips. The strip pitch (e.g. distance between two strips) varies from 40$\mu$m at the inner radius, to 100 $\mu$m at the outer radius (42 mm). All but two of the sensors employ $n^+$-in-$n$ silicon technology (meaning $n$-doped silicon implants in $n$-doped silicon bulk), and the remaining two use $n$-in-$p$ technology, which utilises $p$-type bulk[§]. A more detailed explanation of silicon sensors can be found in Chapter 4.

*Mechanics:* The proximity of the sensors to the beam also imposes further requirements on the design of the VELO. The proton beams could induce radio-frequency (RF) pickup in the VELO, so an RF shield is necessary [74]. The VELO sits in its own vacuum in a secondary vacuum vessel, which is separated from the machine's primary vacuum

[‡] $\phi$ is defined as $\phi = \arctan(\frac{P_y}{P_x})$ where $P_y, P_x$ represent the $y$ and $x$ momentum components of the particle respectively.

[§] Note that the replacement build, VELO2, is built entirely from $n$-in-$p$ technology.

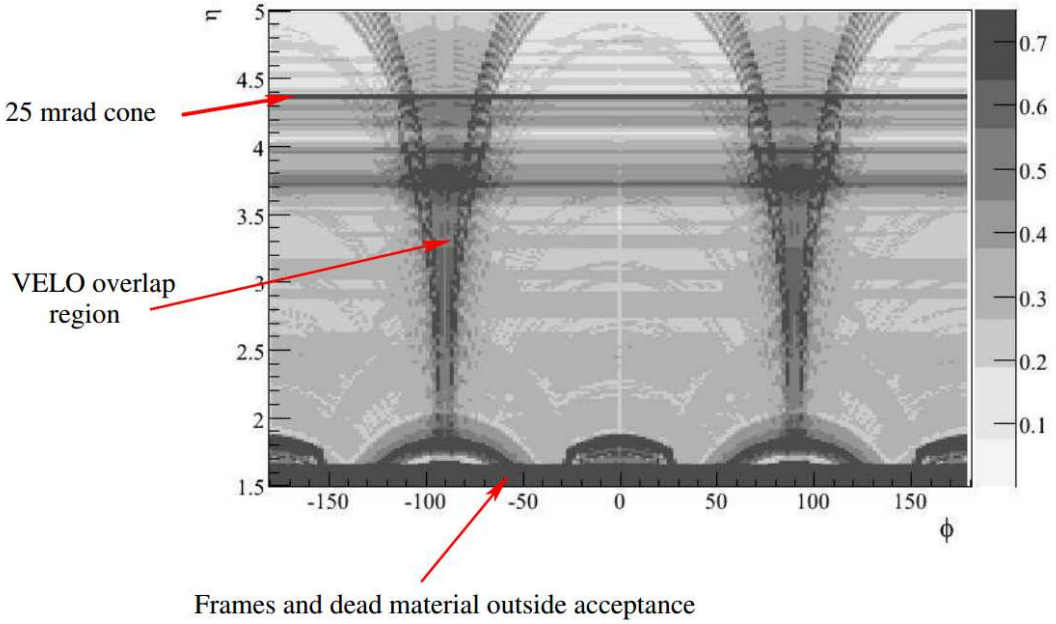


**Figure 3.11:** Radiation length as a function of $\eta$ and $\phi$, integrated up to $z = 270$ cm. The scale on the right hand side is in units of radiation lengths, $X_0$. Reproduced from [71].

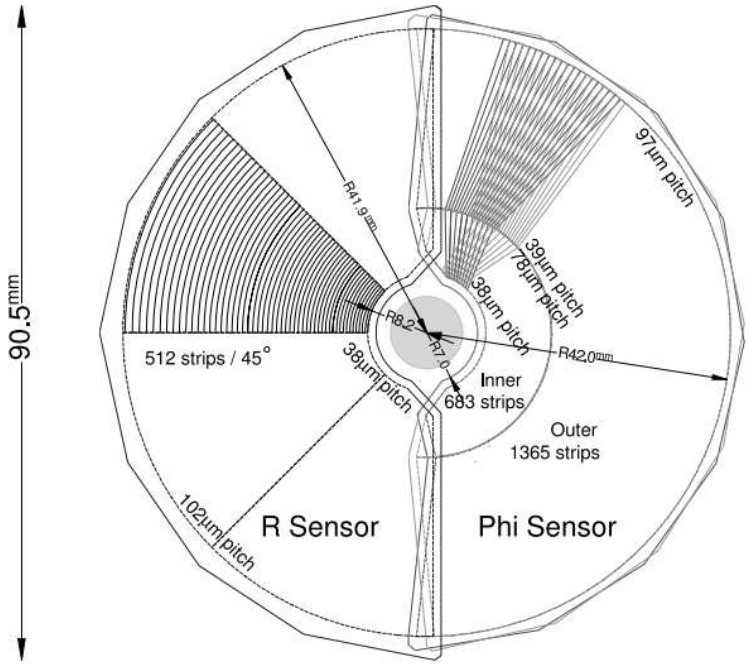


**Figure 3.12:** A sketch of two VELO sensors. Some of the strips are highlighted to illustrate their geometry. Reproduced from [61].

by two 300 $\mu$m thick aluminium boxes which serve as the RF shield. The design of the RF foil is shown in Figure 3.13. It is corrugated so sensors may overlap, allowing for a close measurement to the beam. A schematic diagram of the VELO and its support structure is illustrated in Figure 3.14.

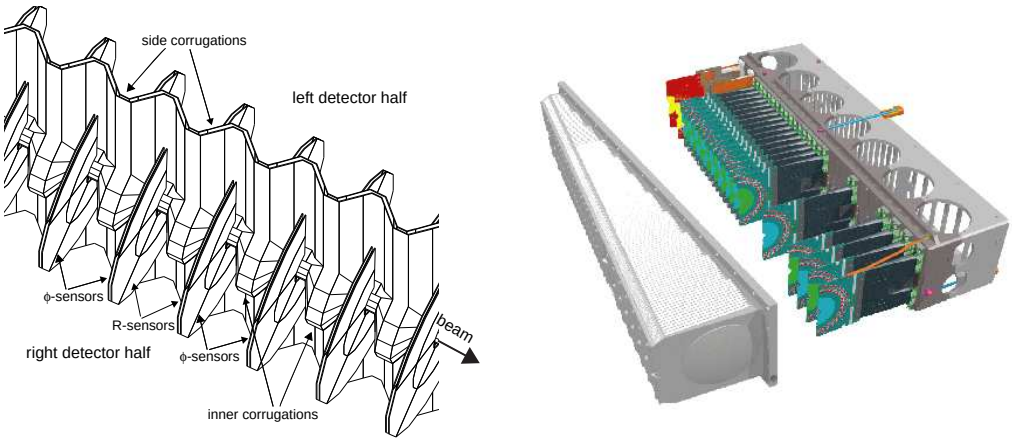


**Figure 3.13:** Left: A zoom-in diagram on the RF foil, showing the two halves of the detectors and the corrugation in the foil to allow the sensors to get closer. Right: A diagram of one completed half of the detector in its assembled state. The second half is removed for clarity in the diagram. Reproduced from [74].

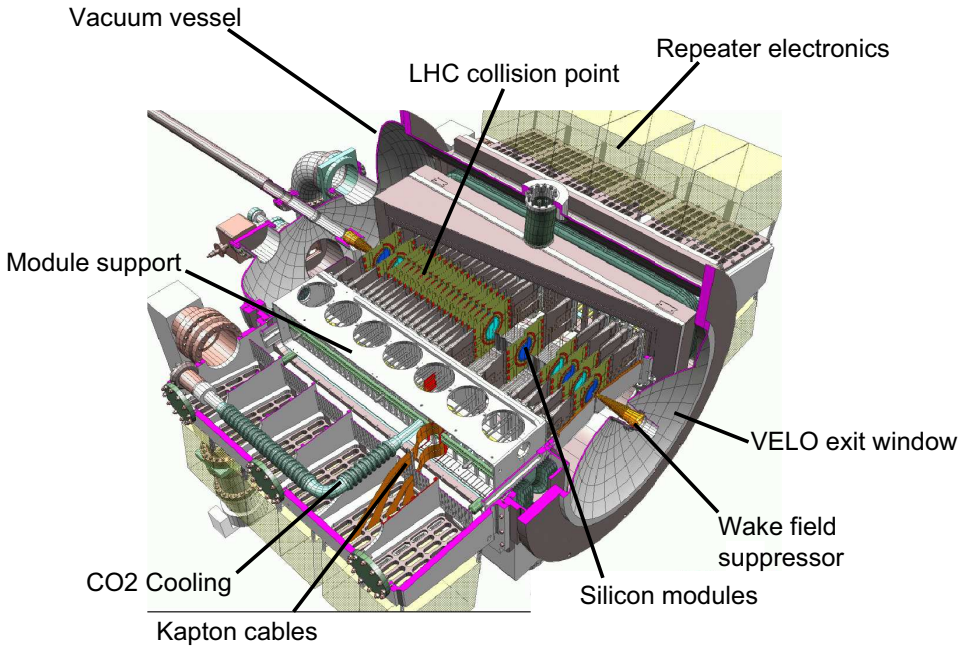


**Figure 3.14:** The VELO vacuum vessel. The modules are displayed in a closed position in the centre. The VELO exit window leads towards the rest of the LHCb detectors. Reproduced from [61].

The sensors are mounted to hybrids which in turn are supported by carbon fibre *paddles*, as illustrated in Figure 3.15. The hybrids have circuit boards laminated onto them, on top of which sit the readout ASICs, temperature sensors, and readout connectors.

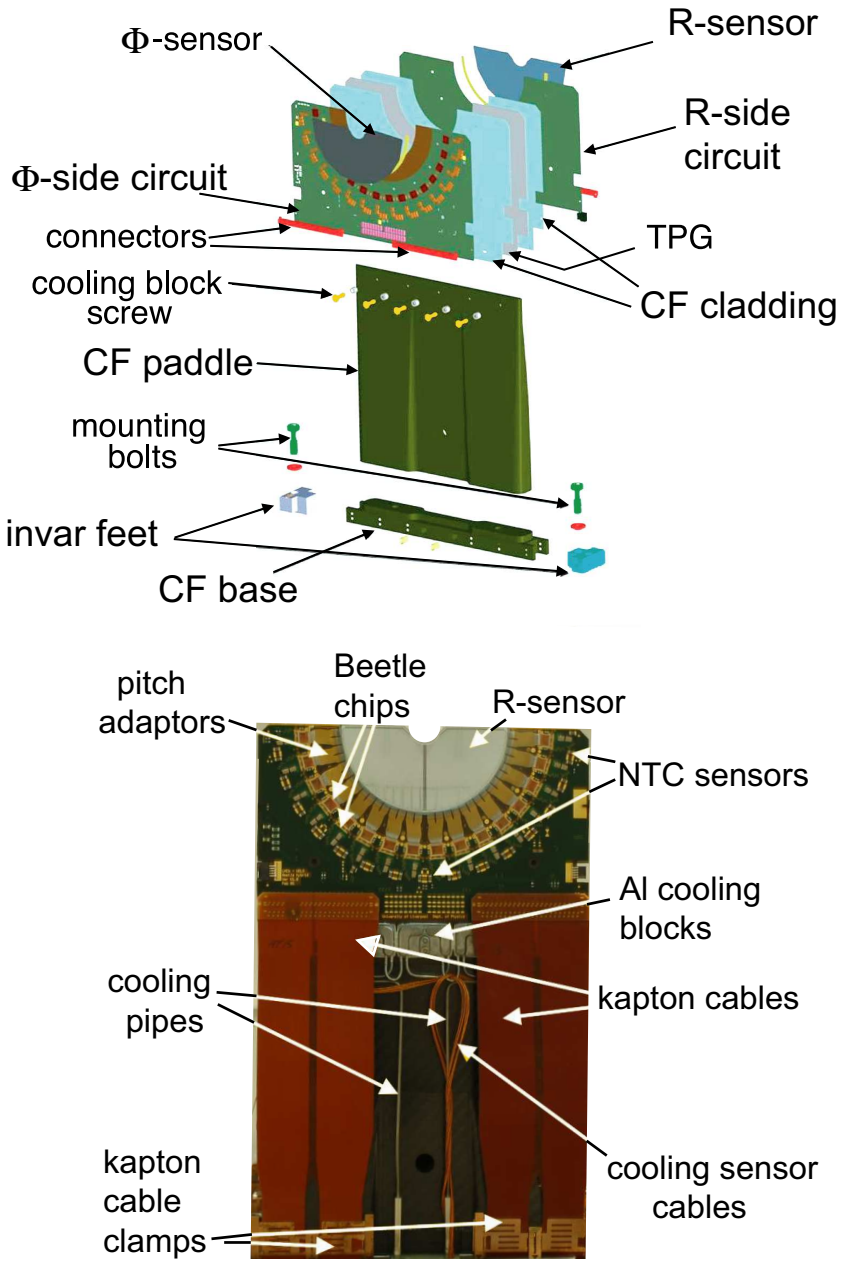


**Figure 3.15:** Top: A diagram of a VELO module and its components, showing the Φ,R combination and mounting. Bottom: A photograph of an assembled VELO module.

*Electronics:* LHCb utilises the Beetle readout chip, which is an analogue 128 channel ASIC [75, 76]. It has an analogue pipeline of 187 cells, and the frequency of the Beetle chip clock is 40 MHz, designed to match the nominal LHC bunch crossing rate. The pipeline has a latency fixed to 128 clock cycles, or 3.2 $\mu$s, which gives the triggering system the time necessary to execute the firmware necessary to decide whether or not an event should be kept. The readout of the chip's 128 channels and 16 bit header is broken down to four chains to increase readout speed, with a 4 bit header + 32 analogue cells readout in normal data taking mode per chain. An example of a Beetle readout data packet for all 128 channels in analogue mode is illustrated in Figure 3.16.

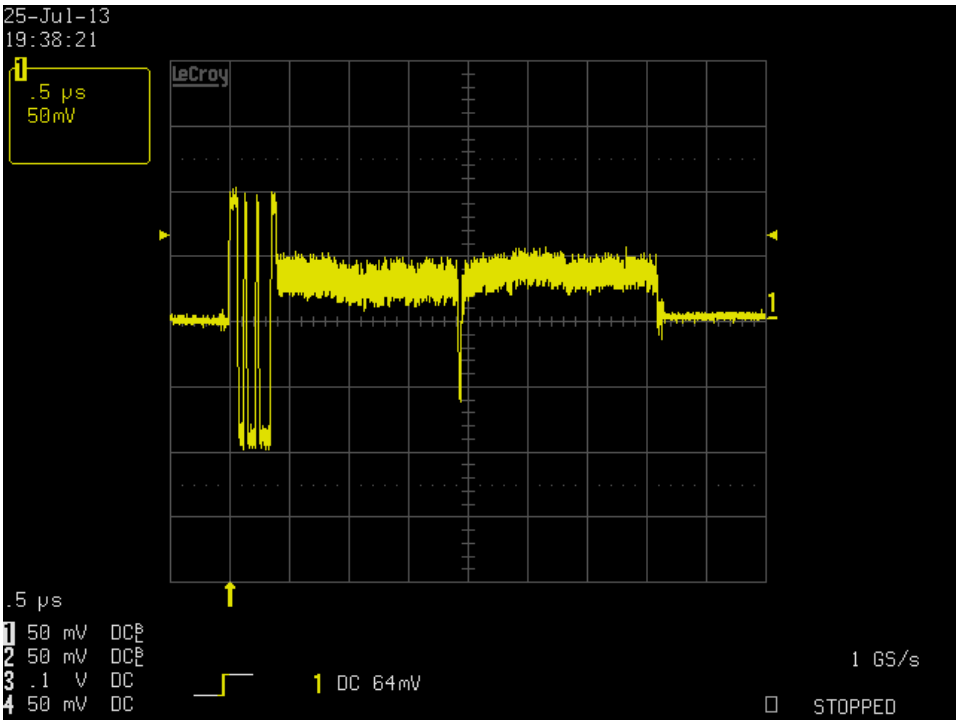


**Figure 3.16:** An example of a Beetle data packet. The digital pulses on the left hand side form the header of the data packet, followed by an analogue read out of all the strips for one event. The dip in the centre of the data packet is the charge deposited by an incident electron.

Mirror charges are induced from the silicon onto the aluminium strips, which are readout by the Beetle chip which is then sent to the repeater board, situated on the exterior of the VELO vacuum tank. The repeater board is responsible for amplifying and shaping the readout data prior to transmission over 60 metre analogue cables to the TELL1 [77]. The charge deposition process is described in more detail in Chapter 4. The TELL1 is a common readout board designed for LHCb, and hosts four A-Rx cards housing 10-bit ADCs which convert the output from the Beetle Chip to digital values.

After these values are converted, TELL1 firmware algorithms including the pedestal subtraction [78] and common mode subtraction algorithms [79] are utilised in order to process the signal. More detail on the algorithms employed can be found in [80]. The output of the TELL1 system is zero-suppressed, i.e. it outputs clusters. An example of the charge deposited in a sensor is presented in Figure 3.17. The signal-to-noise ratio is determined by the signal value divided by the noise ratio. In Figure 3.17, the signal peak has a value of $\sim$37.1, and the typical noise on a channel is $\sim$1.8 ADC counts, leaving a signal-to-noise ratio in excess of $\sim$20. The conversion of electrons to ADC counts are discussed further in Chapter 4.

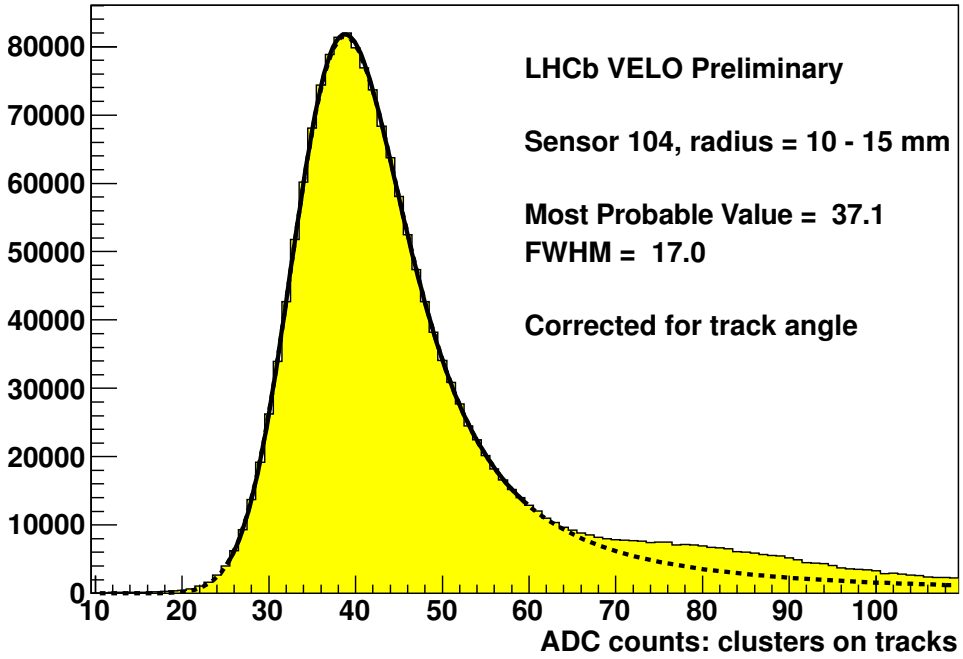


**Figure 3.17:** The charge deposition distribution for a particular sensor aggregated over a series of events. A Landau distribution [81] convoluted with a Gaussian to describe the noise is fitted to the data. The events in the dashed tail after the fit are conversions in material of $\gamma \to e^- e^+$. Reproduced from [82].

After the signal processing algorithms are applied, noise remains on the sensors due to intrinsic fluctuations such as amplifier noise or dark currents. An example of this is presented in Figure 3.18, where the noise from all 42 R sensors is aggregated to an average value and an RMS value. To separate potential signals from this noise, a seeding technique is implemented where strips which start a cluster candidate are required to pass a $6\sigma$ threshold - namely the ADC value of a strip after the processing algorithms must be at least 6 times higher than the typical noise of that strip. Once a seed candidate has been formed, strips either side of it are analysed for potential contributions. This

is performed by looking for neighbouring hits with at least 40% of the seed threshold. Once a full cluster has been found, it can then be passed to the algorithms used in the HLT farm to construct tracks, which are discussed in Chapter 5.

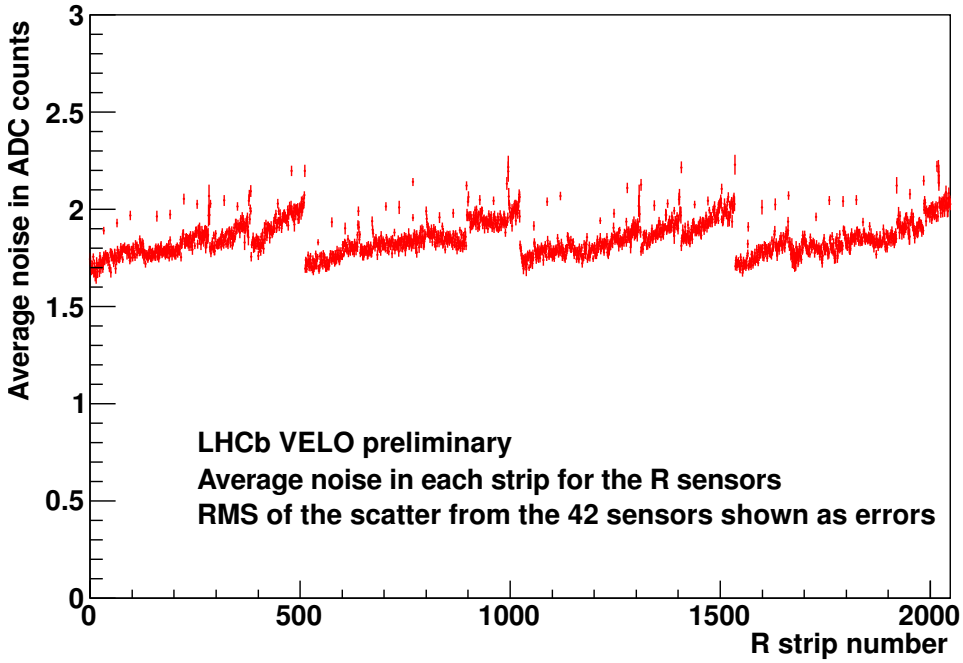


**Figure 3.18:** The average noise for all 42 sensors by strip number. The error on the value represents the RMS of the distribution of the noise for a particular strip between all 42 sensors. The regular structure seen reflect the capacitance of the strips and the electronic noise induced by the header bits in the Beetle readout ASIC. Reproduced from [82].

The depletion voltage, which is defined in Chapter 4, of the sensors changes with irradiation [83], so it is essential to be able to utilise a high voltage system capable of delivering several hundred volts. The high voltage system employed in the VELO has to cover the full potential range of use for the sensors with respect to the radiation damage it may be exposed to. The power supply used for the VELO is capable of delivering up to 700 V at 4 mA [84]. Initial operation is performed with the power supply delivering 100 V at $\sim$ 2 $\mu$A per sensor. Power is supplied to individual sensors, allowing the power requirements of each sensor to be studied in depth (for more detail please see Section 4.2.5).

*Cooling:* Each module requires 20 W of power during regular operation. If the only method of cooling was radiation to the environment, the heat output would raise the temperature in seconds and cause disastrous effects such as damage to the electronics, uncontrollable annealing and thermal runaway on the sensors [85]. Thus, the detector

requires cooling. This is performed through a bi-phase $CO_2$ system [86], which operates at a temperature of -30 °C, and is capable of delivering temperatures of approximately -7 °C on the active region of the sensors. An example thermal profile of one module, taken with an infrared camera, is presented in Figure 3.19.

On average 21.8 W of heat is dissipated per VELO module, increasing to a peak of 27.5 W. The nominal power dissipation for the entire VELO is 1048 W, with the cooling system capable of delivering up to 1600 W [87]. Heat is conducted from the silicon using a 400 micron TPG (Thermal Pyrolytic Graphite) core with a conductivity of 1700 W/m/K to the cooling connections. The capillaries bring the $CO_2$ coolant to the module stations, which are then equipped with aluminium cooling blocks known as *cooling cookies*. The capillaries are embedded into the aluminium by melting the aluminium around the capillaries [88]. The main source of heat in the VELO comes from the chips, which operate at 5 V and 4 A under running conditions.

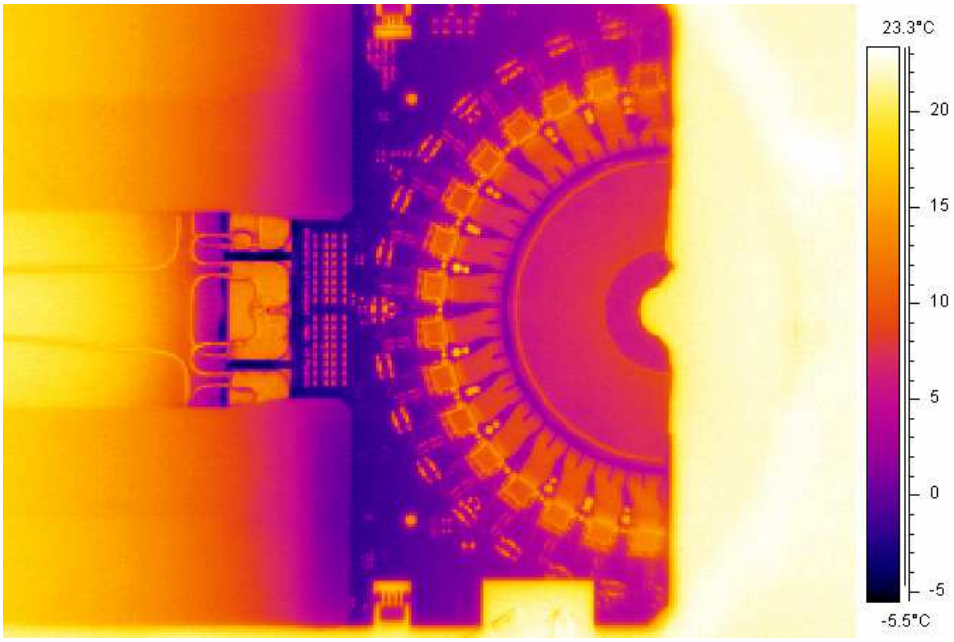


**Figure 3.19:** A thermal image for Module 14, reproduced from [89].

### Tracker Turicensis

The TT stations are located between RICH1 and the Magnet. They are formed of four silicon detector layers arranged in two pairs, $(x, u)$ and $(v, x)$. Each pair is composed of one layer of vertical readout strips and another layer of readout strips which are

rotated by an angle of $\pm 5°$ with respect to the $y$ axis, where $u$ corresponds to $+5°$ and $v$ corresponds to $-5°$ as illustrated in Figure 3.20. This arrangement allows for better measurement of the transverse momentum of particles. The TT contains 896 sensors, divided into 128 modules with seven sensors per module. Each sensor uses 500 $\mu$m thick $p^+$-in-$n$ technology (for more details on silicon and dopants please see Chapter 4), with dimensions $9.64 \times 9.49$ cm, with 512 readout strips where each strip has a pitch of 183 $\mu$m [90]. The modules are paired above and below the beam-pipe to create a full module.

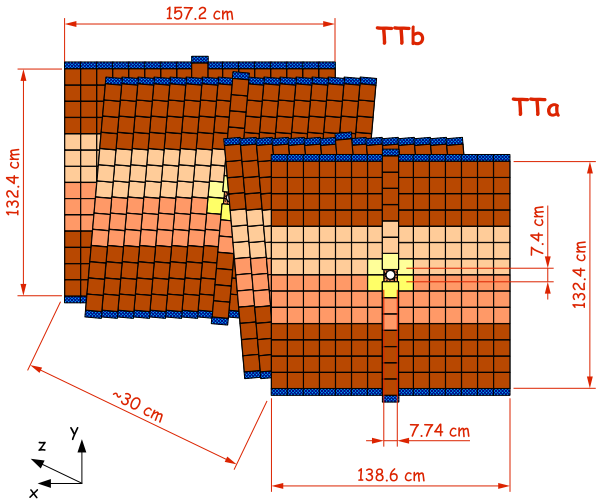


**Figure 3.20:** A schematic view of the four TT silicon layers, with TTa corresponding to the $(x, u)$ pair and TTb corresponding to the $(v, x)$ pair. Reproduced from [90].

### Inner Tracker

The Inner Tracker (IT) is a subset of three stations (T1, T2 and T3), each with four individual segments, which can be qualitatively described as being above, below, to the right and to the left of the beam pipe. Each station is approximately 125 cm wide by 40 cm high, and encompasses the beam-pipe. The modules are designed from silicon micro-strip technology. Similar to the TT stations, it also has stereo modules as shown in Figure 3.21. The IT is comprised of 504 sensors with 384 strips per sensor, with a strip pitch of 198 $\mu$m. The silicon sensors employ $p^+$-in-$n$ technology, with a thickness of 320 $\mu$m, and physical dimensions of 11.0 cm $\times$ 7.8 cm [69].

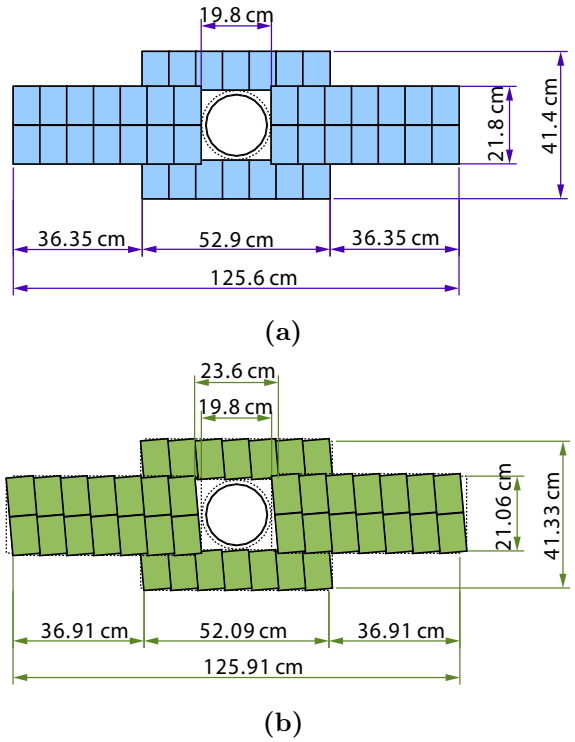


**Figure 3.21:** (a) An $x$ layer of an IT station. (b) An $u$ layer of an IT station. Each box corresponds to a silicon sensor. Reproduced from [69].

### Outer Tracker

The Outer Tracker (OT) surrounds the IT stations, covering the rest of the acceptance. It uses drift-time detectors to find charged particles between the vertex locator and the calorimeters. The choice of a straw system is due to the area coverage required by the outer tracker, and that the precision requirement is lower in the outer region than the inner region. Each module has two staggered layers of straw tubes, which provide a total of 8 detection layers per station [70]. A diagram of the OT in place around the beam-pipe and the inner tracker is shown in Figure 3.22.

Charged particles traversing one of the straw tubes will ionise the gas, a mixture of Ar, $CF_4$ and $CO_2$. The electrons will drift towards the anode wire in the centre of the straw tube. The electric field generates an avalanche affect as electrons drift towards the wire [91]. The drift-time is the delay between the particle ionising the gas and the electrons in the gas being collected by the wire. The drift time, $<$50 ns, can be used to calculate the distance from the anode where the particle traveled through the straw tube. The stations, similar to the TT and the IT, use an $(x, u)$ and $(v, x)$ geometrical pairing.

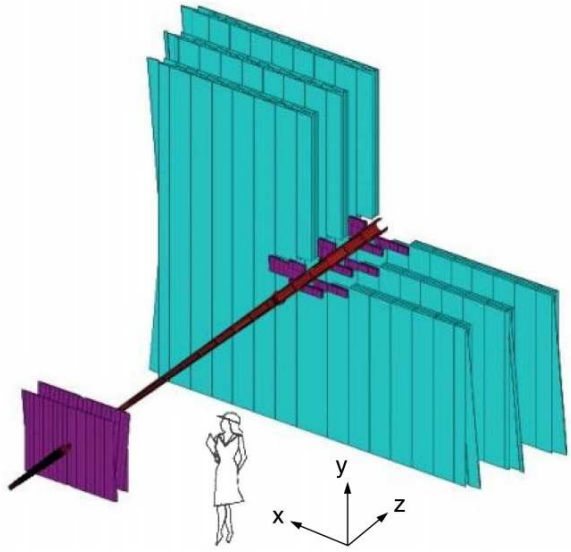


**Figure 3.22:** A diagram of the OT modules with a cut-out for the IT modules around the beam-pipe. Reproduced from [61].

#### The Magnet

The LHCb detector employs a dipole magnet for the bending of charged particles in the vertical plane. The choice of a non-superconducting warm magnet was taken to decrease the risks of failure and cost [68]. Analysis of particle tracks prior to the magnet, and after bending in the magnet, provides measurement of their momenta. Momentum values up to 200 GeV/c are obtained with an approximate resolution of $\sigma_p/p \approx 0.4\%$. An integrated magnetic field path length of 4 Tm is used to achieve this momentum resolution.

The magnetic field is by design uniform in the transverse ($x$) direction. A schematic figure of the magnet is displayed in Figure 3.23. Its polarity is regularly reversed during data taking to allow for the study of systematic effects of the magnet on data. The field strength of the magnet for a central track and a track at 197 mrad is presented in Figure 3.24.

### 3.2.3 Particle Identification (PID) Systems

This section discusses the different particle identification sub-detectors in LHCb and their operational principles. For details on how they combine to provide particle identi-

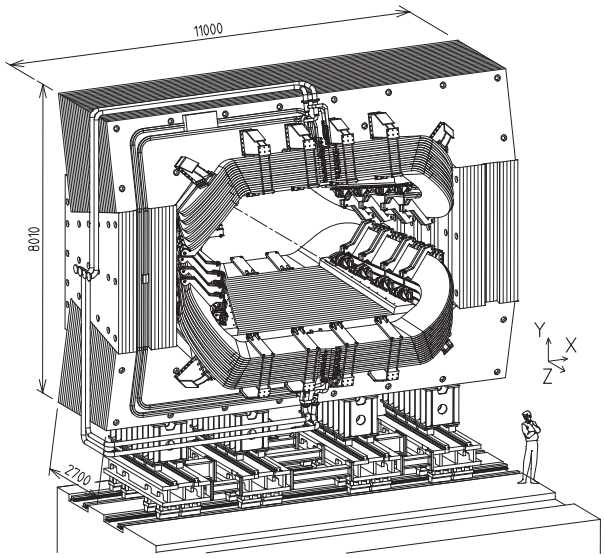


**Figure 3.23:** A schematic view of the LHCb detector magnet, reproduced from [61]. The units are in millimetres.

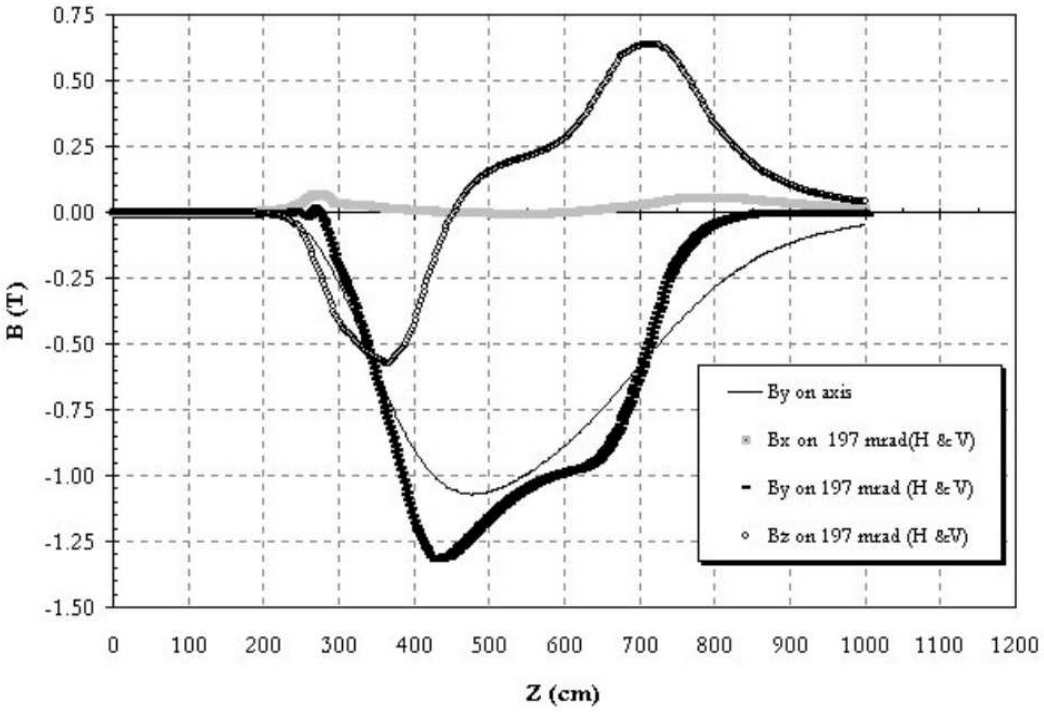


**Figure 3.24:** The field strength for the magnet for different tracks. Reproduced from [68].

fications in the reconstruction/analysis process, and the triggering system that utilises this information, please refer to Chapter 5.

### RICH Sub-detector

Particle identification in LHCb utilises the Ring Imaging CHerenkov detectors. These detectors operate on the principle of Čerenkov radiation [91], which arises when charged particles travelling at very high velocities interact with matter. A particle travelling through a detector at a speed greater than the speed of light in the medium of the detector, will emit electromagnetic radiation, analogous to a sonic boom. The electromagnetic radiation is emitted in a cone along the axis of the particle's direction, with a polar angle $\theta_C$, known as the Čerenkov angle, which is related to the particle velocity $v_p$ by

$$\cos\theta_C = \frac{1}{n\beta} \tag{3.4}$$

where $n$ is the refractive index of the material, and $\beta = v_p/c$, the ratio of the phase velocity of the particle to the speed of light.

Therefore, for different particles with the same momentum but differing masses, reconstruction of the conical radiation can be used to calculate the velocity of the particle. With known momentum information, this can be combined to determine the mass of the particle. There are two RICH stations at LHCb, RICH1 and RICH2, optimised for different momentum regions [92]. Photons are identified using a system of mirrors and phototubes (HPDs).

### Calorimeters

A calorimeter system is designed to make measurements of the energy of hadrons, electrons and photons. In LHCb, there are four different calorimeter stations located between M1 and M2 [93]. These are the electromagnetic calorimeter (ECAL), the hadronic calorimeter (HCAL), the preshower detector (PS) and the scintillator pad detector (SPD). The calorimeters are designed to assist in particle identification by primarily detecting specific subsets of particles; the electromagnetic calorimeter is designed for the measurement of energy of photons and electrons, and the hadronic calorimeter is designed for the detection of hadronic activity. The energy information obtained from

the calorimeters is then used in the Level 0 trigger to determine whether an event should be selected or not, as well as in the final physics analyses.

High energy particles traversing sufficient material will undergo a process known as showering, where interactions result in a cascade of secondary particles. After the process of several showers, a very high energy particle will have interacted sufficiently - and thus produced enough secondary showers - to result in a measurable fraction of its energy being transferred into these secondary showers. A secondary shower may in turn interact with the material, and deposit energy into it. The principle employed in the calorimeter is that the number of secondary showers is proportional to the energy of the incident particle.

Showers can be classified as either electromagnetic or hadronic. These have different properties. An electromagnetic shower is produced by a particle which primarily interacts through the electromagnetic force such as bremsstrahlung and pair production to create its shower of particles. The probability of showers is determined as a function of the radiation lengths travelled in the material ($X_0$) and is proportional to $Z^2$, where $Z$ is the atomic number [94]. After one radiation length, only $1/e$ of the particle's original energy remains.

Hadronic showers are governed by the strong interaction, which has many different processes contributing to the production of secondary hadrons. The probability of a shower in this case is determined by the nuclear absorption length of a material, $\lambda_l$, and is proportional to $A$, the nucleon number. After one interaction length, only $1/e$ of the particle's original energy remains.

A cut-away diagram of all four calorimeters in LHCb is presented in Figure 3.25[¶], and will be described individually below:

*SPD/PS*: The SPD (Scintillator Pad Detector) and PS (Pre-Shower detector) utilise scintillator pads readout by wavelength shifting fibres that are subsequently coupled to photo-multiplier tubes. The utilisation of wavelength shifting fibres is designed to maximise the efficiency of refracting incident light. A lead converter is placed between the SPD and PS detectors, and has a radiation length of $\approx 2.5\ X_0$. It has 12,032 channels and is of size 6.2 x 7.6 square-metres. The SPD is used to detect charged particles before the lead converter. The information from the SPD can be useful in discriminating photons from electrons. The pre-shower detector provides another measurement of show-

[¶]The author would like to thank Irina Machikhiliyan for making this graphic available in high resolution.

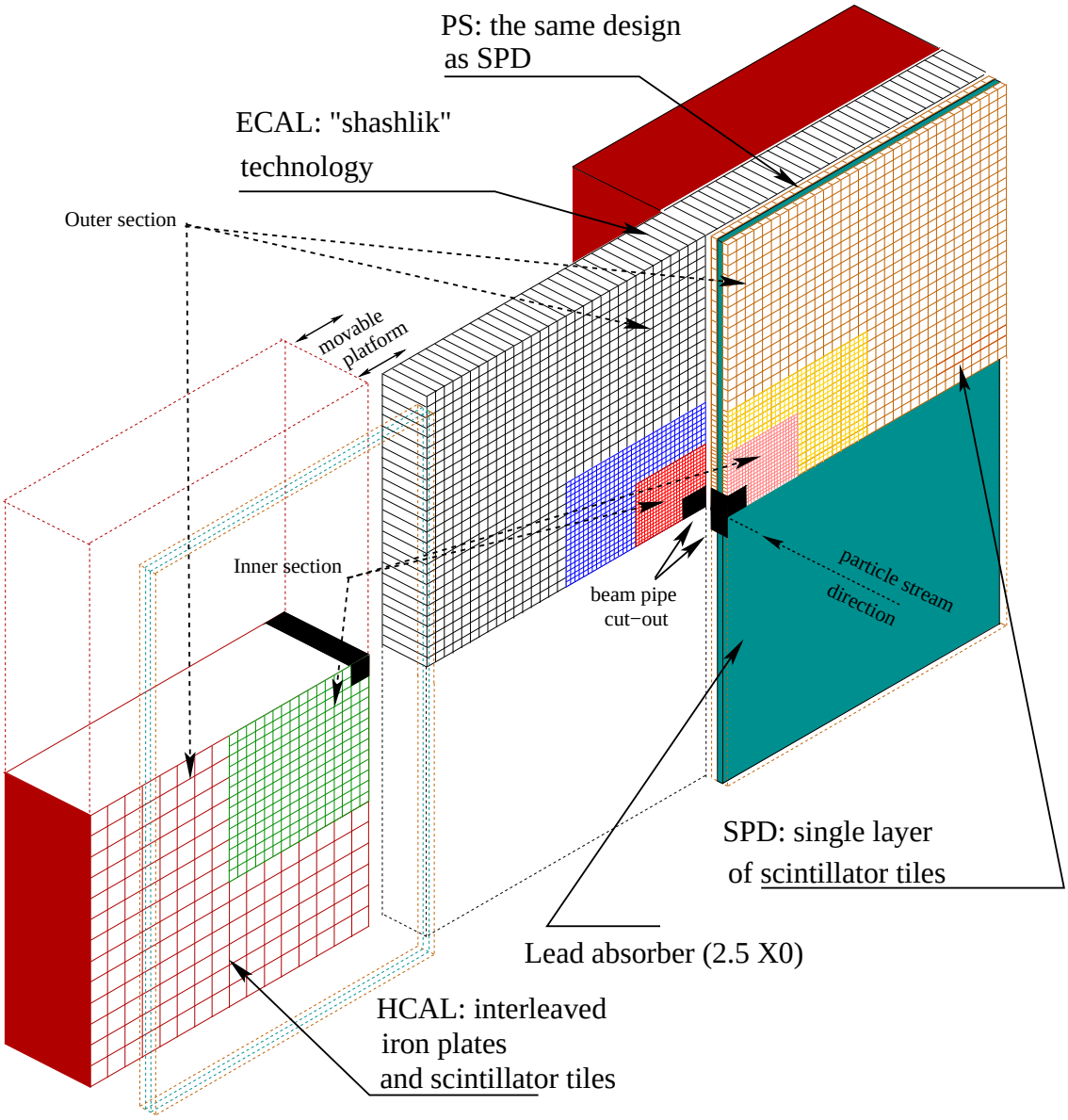


**Figure 3.25:** A cut-away diagram of all four calorimeter systems in place in LHCb. The segmentation referred to for the ECAL can be observed in further depth in Figure 3.26. Reproduced from [95].

ering effects before the relevant calorimeter (e.g. ECAL for electromagnetic particles, or HCAL for hadronic particles). The SPD also provides information for the trigger on the L0 level.

*Electromagnetic Calorimeter*: The ECAL operates by using a mixture of scintillating tiles and lead absorbers. It consists of 6,016 channels and corresponds to approximately 25 $X_0$, but only approximately 1.1 $\lambda_l$. It is divided into three sections, as illustrated in Figure 3.26 and Figure 3.27. The energy resolution of the ECAL is found to be $\frac{8\%}{\sqrt{E}} \oplus 0.8\%$ [96]. It is important to note that the ECAL resolution saturates by design as described further in [97] and [98]. For a 10 GeV/c incident electromagnetic particle, it has an approximate energy resolution of $\sim$ 2.7%.

*Hadronic Calorimeter*: The hadronic calorimeter uses scintillating tiles and iron absorbers. It corresponds to approximately 5.6 $\lambda_l$. The HCAL has an energy resolution of $67\%\sqrt{E} \oplus 9\%$ [99], which yields a result of $\sim$ 6.8% uncertainty for a 10 GeV/c hadron.

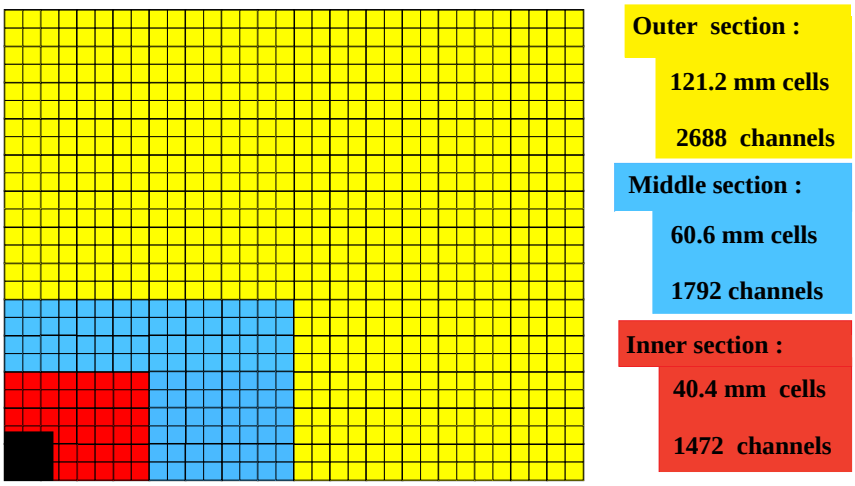


**Figure 3.26:** An illustration of the segmentation of the sections of the ECAL sub-detector. It is designed to have higher resolution in the central regions. The cells are not drawn to relative scale. Reproduced from [93]

### Muon System

LHCb employs five muon stations [100], labelled M1-M5, with the last 4 stations placed behind both electronic and hadronic calorimeters. The muon chambers M2-M5 are interleaved with the iron absorbers to suppress hadronic backgrounds, and M1 is placed in front of the PRS. Each station has four discrete *regions*, R1-R4, giving a total of twenty regions. A side view of the five muon chambers in situ is presented in Figure 3.28. An

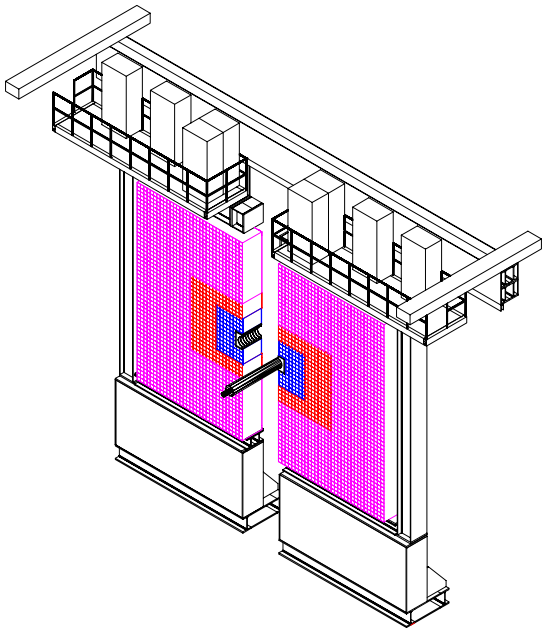

**Figure 3.27:** A schematic diagram of the ECAL around the beampipe in LHCb, with support structure. Reproduced from [93].

aggregate of 20 nuclear interaction lengths exist between the interaction point and M5, designed to decrease hadronic and electronic background contributions. The muon system is very important for the trigger, which will be documented further in Chapter 5. The momentum resolution of the muon chambers is optimised for efficient muon triggering $> 5$ GeV/c, which is the minimum momentum a muon is required to have to traverse all five stations.

The inner most stations of M1 is built using Triple-GEM detectors (Gas-Electron Multipliers) which consist of three layers of different GEMs designed to prolong detector lifetime [101], whereas Regions 2 to 4, and the subsequent muon chambers, are built with Multi Wire Proportional Chambers (MWPC) [102]. The acceptance of each region is designed to be approximately the same, and the granularity is designed such that the occupancy is approximately uniform over the detector. The MWPC system uses anode wires with cathode pads and a wire pitch of 1.5 mm, with a total distance from the anode wire to cathode pad of 2.5 mm on either side, and a gas mixture, similar to the Outer Tracker, of $CO_2$, $CF_4$, and Ar. The Triple-GEM system uses a similar mix of gas, and has a prolonged radiation hardness which allows it to handle the radiation flux exposed to the triple-GEM detectors in the innermost regions through a flushing mechanism [103].

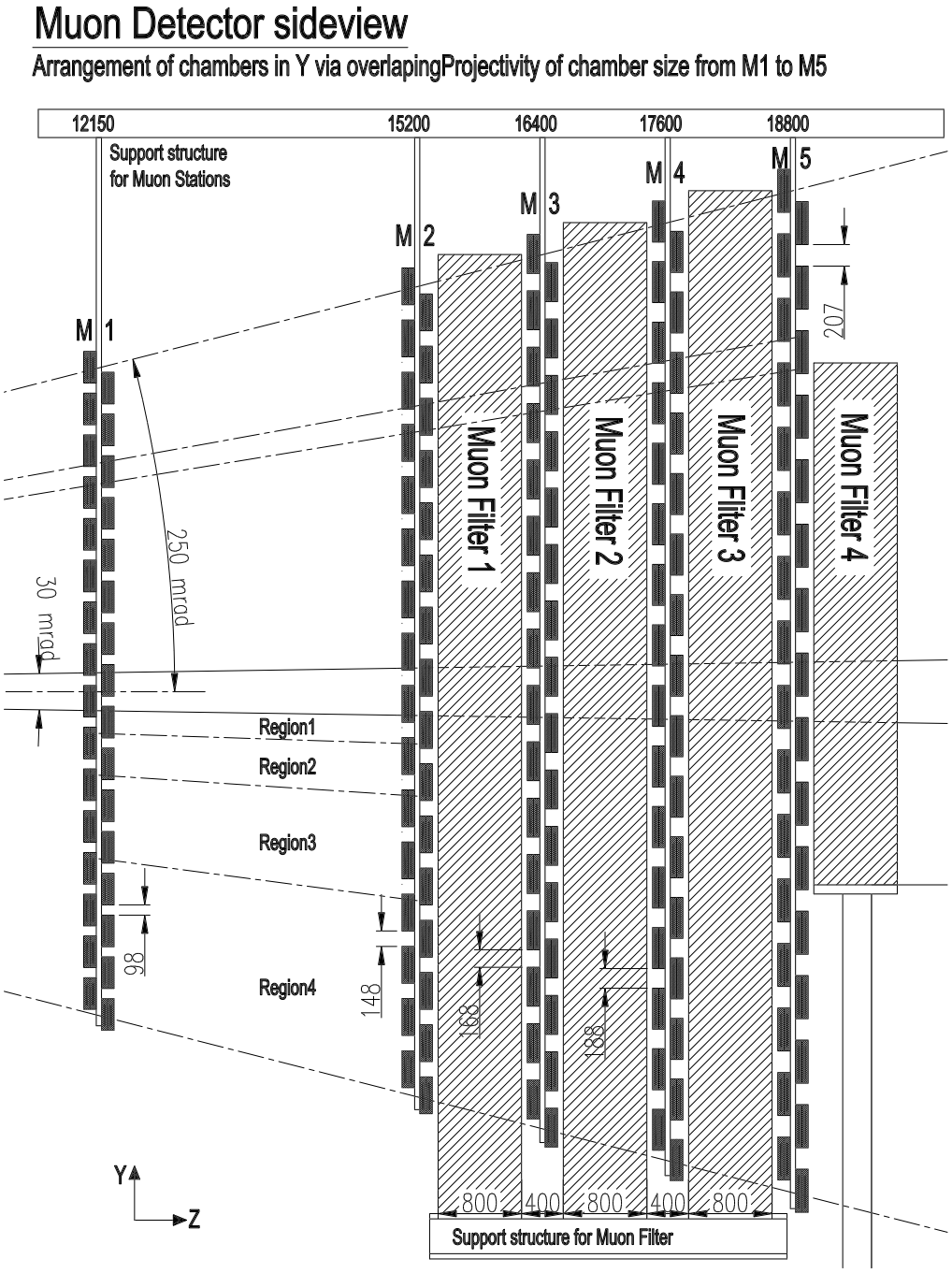


**Figure 3.28:** A side view of the muon chambers in LHCb. Reproduced from [100].

### 3.2.4 Summary

LHCb is a precision experiment at the Large Hadron Collider optimised for detailed measurements of $b$-hadrons. The sub-detectors that comprise the experiment have been described together with the fundamental physics principles on which they operate. The combination of the information from the sub-detectors to reconstruct tracks, particles and ultimately underlying physics processes is described further in Chapter 5. A more detailed discussion on the principle which govern the operation of the VELO, and a new study for the monitoring of radiation damage is presented in Chapter 4.

# Chapter 4

# Radiation Damage in the LHCb Vertex Detector

The VELO is designed to make precise measurements of tracks and vertices from LHC collisions. This requires, amongst other constraints, that the detector is very close to the interaction point and that it is as low mass as possible. The proximity to the interaction point implies a high fluence of particles through the active elements. The detector, as described in Chapter 3, uses silicon strip technology for its active sensors. The passage of particles through the VELO has a detrimental effect as the energy deposition causes damage in the sensors. To mitigate this damage, the VELO employs radiation hard technology to extend its operational lifetime. This chapter gives more information on the principles behind semiconductor detectors, their exposure to radiation and discusses the use of current-voltage (IV) scans to monitor radiation damage in the VELO.

## 4.1 Silicon Detectors

Silicon is a semiconductor material. A semiconductor material is a pure covalently bonded lattice, which does not conduct electrical charge at room temperature, as the electrons are not able to make the transition between the two distinct energy bands of the lattice, known as the valence band and the conduction band [104]. Electrons in the valence band are tightly bound to the atoms in the lattice. They cannot move freely and do not contribute to conduction. Electrons in the conduction band are, by contrast, effectively free and have a high mobility. The energy gap in silicon is the energy required to move an electron from the valence state to a conductor state and is

$\sim$ 1.2 eV in silicon. A graphical comparison of the bands in a semiconductor, conductor and insulator is presented in Figure 4.1.

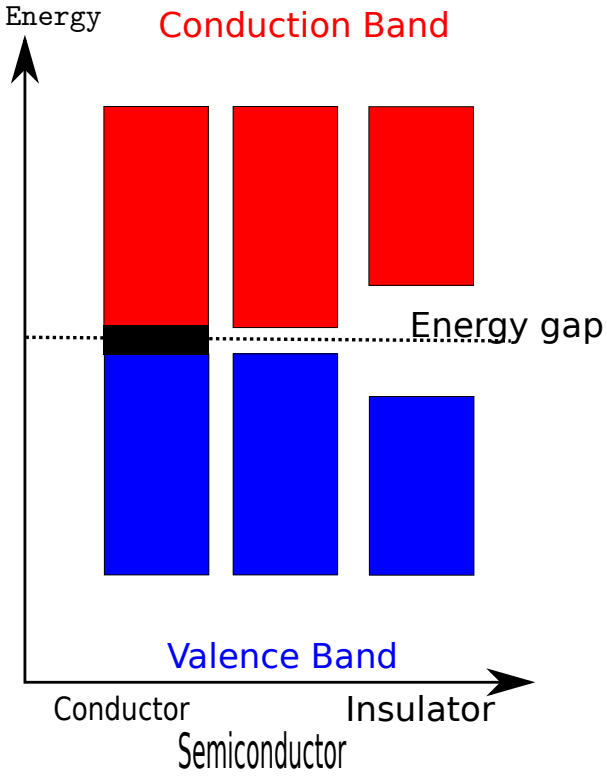


**Figure 4.1:** An illustration of the difference in the band gaps of semiconductors, conductors, and insulators. The process of doping a semiconductor introduces new levels in the energy gap.

By a process called *doping* [83] it is possible to increase the number of free charge carriers. There are two types of doping, called $p$ (positive) doping, and $n$ (negative) doping; $n$-type doping in silicon can be achieved through the introduction of phosphorus, and $p$-type doping can be achieved through the introduction of boron. In $p$-type doping, the doping material removes an electron from the silicon lattice and leaves a hole, resulting in an increase of the net positive free charges. In $n$-type doping, the dopant provides an extra conduction electron, which results in net negative free charge carriers.

A $p$-$n$ junction is formed at the boundary of a $p$-type and $n$-type semiconductor. The free charge carriers from each of these regions diffuse, resulting in a region depleted of free charge carriers. A reverse bias can be applied to this junction to increase the width of the depletion region.

The voltage required to deplete a thickness $d$ is given by [83]:

$$V_D = \frac{q}{2\epsilon}|N_{eff}|d^2 \tag{4.1}$$

where $V_D$ is the depletion voltage, $N_{eff}$ is the number of effective charge carriers, $q$ is the electron charge and $\epsilon$ is the permittivity of the material. When the depleted thickness $d$ is equal to the thickness of the sensor, full depletion is said to have occurred.

### 4.1.1 Charge Deposition

Charge deposition by ionising particles in material is governed by the Bethe-Bloche formula, Equation (4.2) [1]. It describes the expected energy deposition as a function of the material parameters (for example number of protons) and momentum of the incident particle,

$$-\frac{dE}{dx} = \frac{4\pi}{m_e c^2}\frac{nz^2}{\beta^2}(\frac{e^2}{4\pi\epsilon_0})^2[\ln(\frac{2m_e c^2\beta^2}{I(1-\beta^2)}) - \beta^2] \tag{4.2}$$

where $\frac{dE}{dx}$ represents the change in energy of the incident particle over the distance travelled, $m_e$ is the mass of the electron, $z$ is the charge of the incident particle, $n$ is the number of charged nucleons, $\beta$ is $v/c$, $\epsilon_0$ is the vacuum permittivity constant, and $I$ is the mean excitation potential for the electrons in the atom. A minimum ionising particle will create typically $\sim$80 electron-hole pairs per micron in silicon [105].

### 4.1.2 A *p*-*n* Junction as a Particle Detector

Providing that a sufficiently high reverse voltage is applied to the junction, the electron-hole pairs created by ionising radiation may be separated before they have time to recombine. After separation, they are attracted to their respective electrodes. This forms the basis of a practical detector. In the specific implementation of a $n$-type single-sided readout silicon micro-strip detector, such as Figure 4.2, the motion of the electrons and holes to the implants induces a mirror charge in the aluminium strips, which are separated from the bulk by a layer of silicon dioxide. This charge is then readout by the front-end electronics for further processing.

The configuration of the sensor chosen for LHCb detects electrons away from a negatively charged backplane. This means that negative charge are effectively collected by

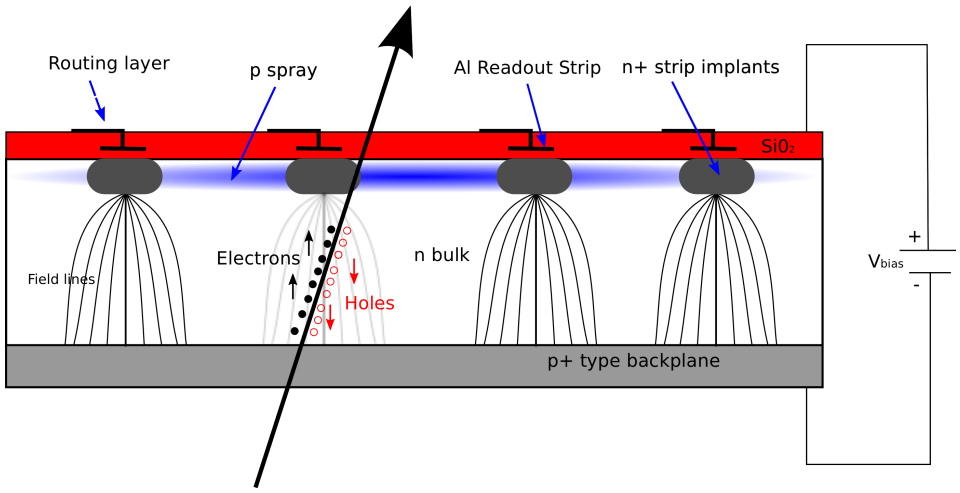


**Figure 4.2:** A diagram of a $n$-in-$n$ silicon micro-strip sensor. The diagram is an example of a VELO $R$-type sensor, with routing lines for carrying the signal to the readout chips. The $p$ spray is an additional layer of $p$-type material to help prevent the formation of an excess of positive charge on the surface layer. Reproduced from [97].

the segmented part of the sensor. The reason for this choice is that the electrons have higher mobility and show less evidence of trapping under radiation than holes. The deposited charge is readout and then converted by the electronics chain into Analogue-to-Digital Converter (ADC) counts. An example plot of the charge deposition is shown in Section 3.2.2. One ADC count is approximately equivalent to 650 electrons.

## 4.2 Radiation Effects

### 4.2.1 Radiation Damage Overview

Particles passing through the silicon can damage the sensor. The mechanisms behind the damaging process are, non-ionising energy loss (NIEL) and ionising energy loss (IEL). The two basic types of radiation damage, are known as *displacement* and *ionisation*. Displacement damage occurs when incident radiation displaces silicon atoms from their lattice sites. The displaced sites can then trap charge, which alter the internal electric fields of the lattice. Variations in the electric fields change the mobility of the electrons and holes in the lattice, and therefore the speed, and amount, of charge that is collected. An example of displacement damage would be when an incident particle transfers sufficient energy to atoms to dislodge them from the lattice. In the example used in [83],

a 1 MeV neutron could transfer 60-70 keV to a recoil silicon atom, which in turn could displace $\sim$ 1000 additional atoms, creating a defect cluster. Defect clusters can leave sites in the lattice which can "trap" electrons. By trapping these electrons rather than allowing them to move towards their electrode, this degrades the signal performance of the detector and can significantly decrease the signal-to-noise ratio achievable, and hence the tracking performance. Ionisation damage occurs when ionisation electrons drift or diffuse into locations such as the previously described displaced sites, which can cause concentrations of charge, and as a result, parasitic fields [83].

Since the energy deposition of particles at different masses and different momenta can vary greatly, calculations must be standardised. The standardisation used is a reference of 1 MeV neutron-equivalents, which allow for the comparison of radiation damage from different particles and momenta. This results in fluences being stated as, for example, $1.5 \times 10^{13}$ 1 MeV-$n_{eq}$ / cm$^2$ to allow for comparison between different beam compositions and energies. An example of the damage factors, which is the ratio of the damage between the particle and the reference point, between different particles of different energies is presented in Figure 4.3.

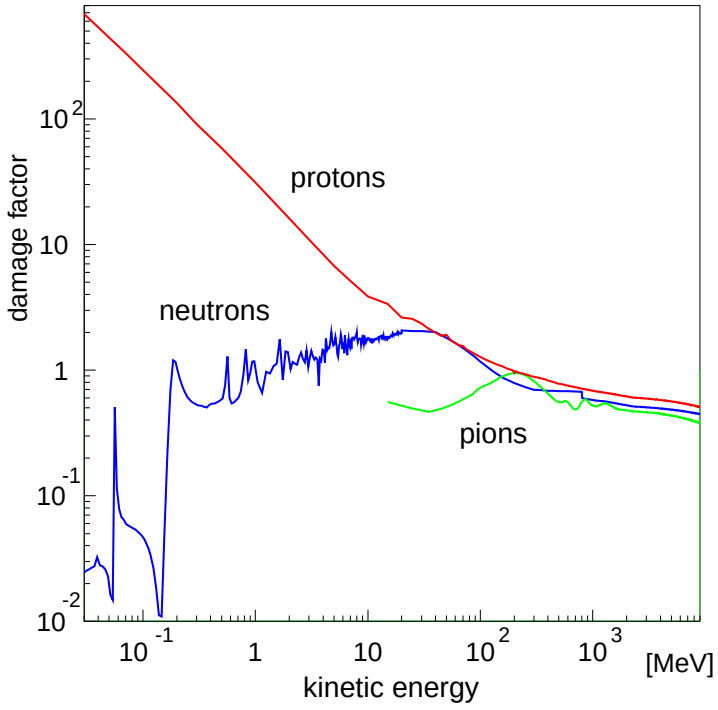


**Figure 4.3:** The damage factors between a range of particles and energies. The reference value is chosen such that a 1 MeV neutron has a damage factor of one. Reproduced from [74].

The VELO is exposed to a high particle flux of both charged and neutral particles. The flux of these particles is simulated in order to allow for a calculation of the approximate radiation damage to which the VELO will be exposed. The radiation damage is then modelled for each VELO sensor with a radial dependence [84]. This model is described through two parameters:

$$\phi = Ar^{-\beta} \tag{4.3}$$

where the constant, $A$, describes the 1 MeV neutron-equivalent fluence per fb$^{-1}$ at $r = 1$ cm, and an exponent $\beta$ describes the radial dependence. A plot of these two quantities for 1 fb$^{-1}$ of integrated luminosity is presented in Figure 4.4. These values are subsequently used in Equation (4.3) to calculate the rate of NIEL fluence per fb$^{-1}$, which can be used later to calculate macroscopic quantities such as the expected current for the sensor at its depletion voltage*. Detailed discussions on the mechanisms of radiation damage can be found in [106] and [83].

### 4.2.2 Leakage Current in the VELO Sensors

The leakage currents observed in the sensors may be phenomenogically split into two separate components. The first, the *bulk* current, has a known temperature dependence discussed further in Section 4.2.3, and arises from the current through the volume of the sensor. The second current, typically called the *surface* current, does not follow the same temperature dependence and can arise from irregularities introduced during sensor production such as processing errors or scratches on the silicon surface. Leakage current increases noise in the detector, which decreases the signal-to-noise ratio, and also heats the sensor, which can potentially cause problems such as uncontrolled annealing. Annealing is described in more detail in Section 4.2.4.

The bulk current in a sensor may be calculated as a function of the fluence by Equation (4.4) [108]:

$$I = \alpha V \phi \tag{4.4}$$

where the quantity $I$ is the current at depletion voltage (A), $\alpha$ is the constant for relating changes in the current to a fluence (A/cm), V is the active volume of the sensor (cm$^3$),

*The ionising energy loss is exactly the signal contribution, and only effects regions where signal is not desired - such as the silicon dioxide.

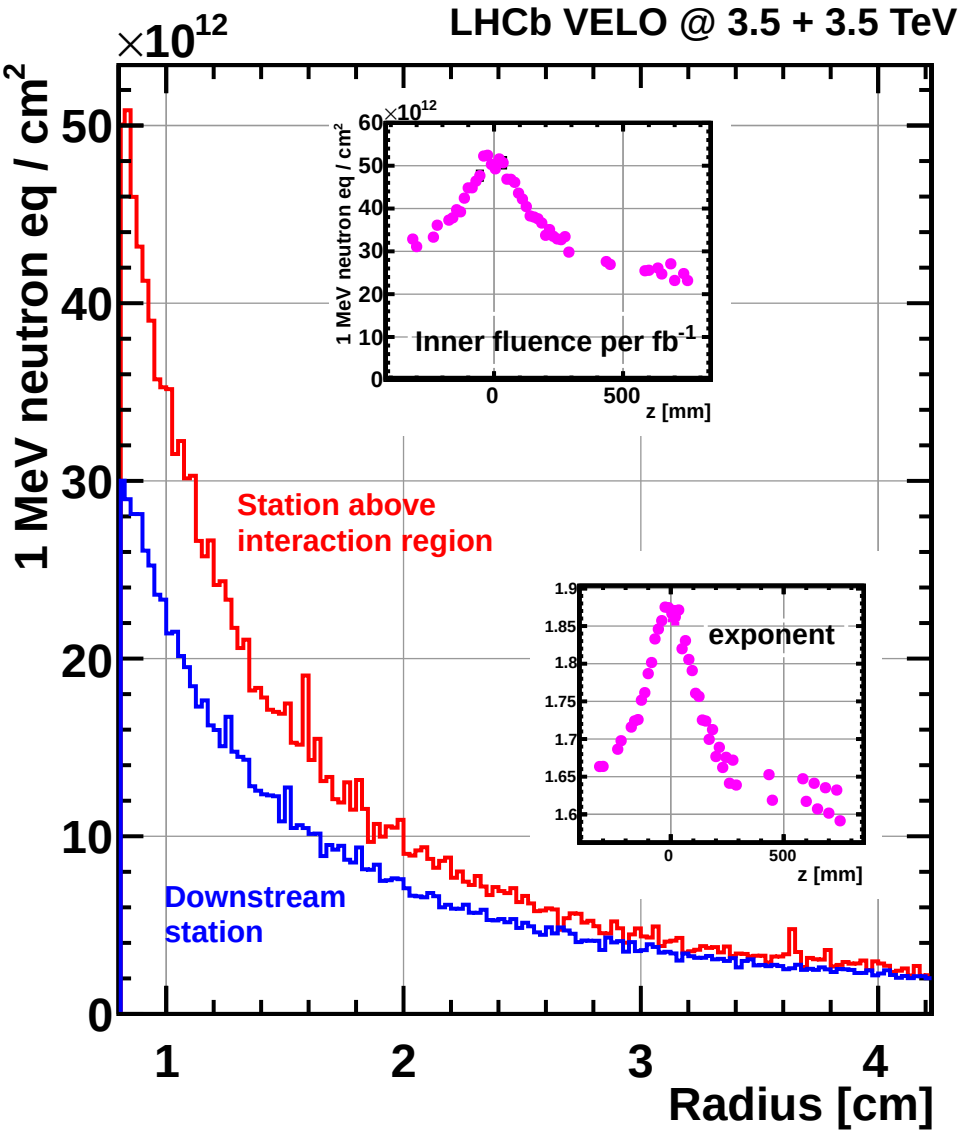


**Figure 4.4:** The LHCb VELO fluence (from simulation) profile for 1 $\text{fb}^{-1}$ of integrated luminosity. The primary plot contains two example fluence distributions for sensors in different $z$ locations. The upper plot contains the inner fluence (at r=8 mm) for the sensors as a function of their $z$ location, and the bottom right plot contains the value of the $\beta$ exponent. This plot is reproduced from [107].

and $\phi$ is the fluence profile for the sensor as described in Equation (4.3) with units of 1 MeV neutron-equivalent. To couple Equation (4.4) with Equation (4.3), the sensors can be modelled as a series of infinitesimal strips of width $\delta$r at a radius $r$, and it can be shown that by substituting in the volume of an infinitesimal strip, the increased current

for this infinitesimally small strip will be:

$$\delta I = \alpha \pi r \delta r t A r^{-\beta}. \tag{4.5}$$

After integrating this equation with respect to the radius, the equation becomes:

$$\Delta I = \frac{A \pi t \alpha}{2 - \beta} [r^{2-\beta}]_{r_i=0.8}^{r_o=4.2} \tag{4.6}$$

where the values $r_o$ corresponds to the outer radius of the active region (in cm) of the detector, and $r_i$ corresponds to the inner radius of the active region.

The depletion voltage of the VELO is variable across a single sensor after irradiation, as the particle flux exposed is heavily dependent on the region of the detector. The innermost parts of the detector have significantly higher depletion voltages than the outermost parts. To avoid complications arising from this, the VELO is operated at a voltage higher than the anticipated depletion voltage, to ensure the entire detector is fully depleted. Currents, as can be observed in Figure 4.5, saturate past the depletion voltage. The current at 150 V is less than 3% greater than the current at 60 V.

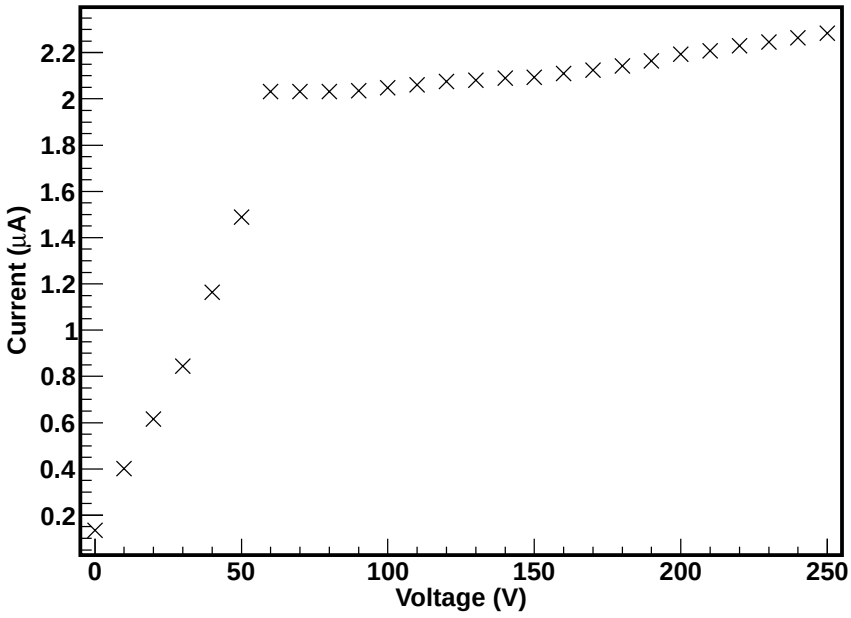


**Figure 4.5:** An IV scan for a sensor at production. The depletion voltage has been measured from a CV (capacitance-voltage) scan to be $\sim$ 50 V. Data reproduced from [109].

### 4.2.3 Temperature Compensation

The bulk current drawn by silicon sensors is heavily dependent on the temperature at which they operate. The proportionality is described by Equation (4.7) [110].

$$I(T) \propto T^2 e^{-(\frac{E_{ef}}{2kT})}. \tag{4.7}$$

The predictions documented in Equation (4.6) are obtained for a temperature of T = 273 + 21°K, which is significantly different from the operational temperature of the sensors, and the temperature at which the scans are taken. Thus, it is important to scale this prediction down to the operational temperatures, using Equation (4.8). The thermal compensation equation only applies for the bulk current in the sensor and currents arising from other sources such as surface damage will not be accurately modelled by this equation. The parameters for Equation (4.8) are listed in Table 4.1.

$$\frac{I(T_1)}{I(T_2)} = (\frac{T_1}{T_2})^2 \times e^{-\frac{E_{ef}}{2k} \times (\frac{1}{T_1} - \frac{1}{T_2})} \tag{4.8}$$

| Parameter | Description | Value |
|---|---|---|
| $E_{ef}$ | Silicon band gap | 1.21 eV $\times$ $1.6 \times 10^{-19}$ J/eV [110] |
| k | Boltzmann's Constant | 1.38 $\times$ $10^{-23}$ $m^2$ kg $s^{-2}$ |
| $T_2$ | Reference temperature | 273+21 °K |
| $T_1$ | Target temperature | 273-8.3 °K |

**Table 4.1:** Parameters for the temperature compensation, in Equation (4.8). The reference and target temperatures are chosen to match the current predicted using $\alpha$(T=273+21°K) and the operating temperature of T=273-8.3°K.

### 4.2.4 Annealing

Annealing in silicon is a process where thermal energy modifies the damaged lattice. Beneficial annealing effects will be manifested as a decrease in the currents for the bulk-current dominated sensors. Annealing is empirically modelled by Equation (4.9) [111], which is obtained from a parameterised fit to experimental data as shown in Figure 4.6. For the latest results in annealing and its effects, see [112], or for a discussion on the mechanisms behind annealing, see Section 3.5 of [111]. The annealing time-dependent $\alpha$ factor can be calculated from this parameterised fit with the following equation:

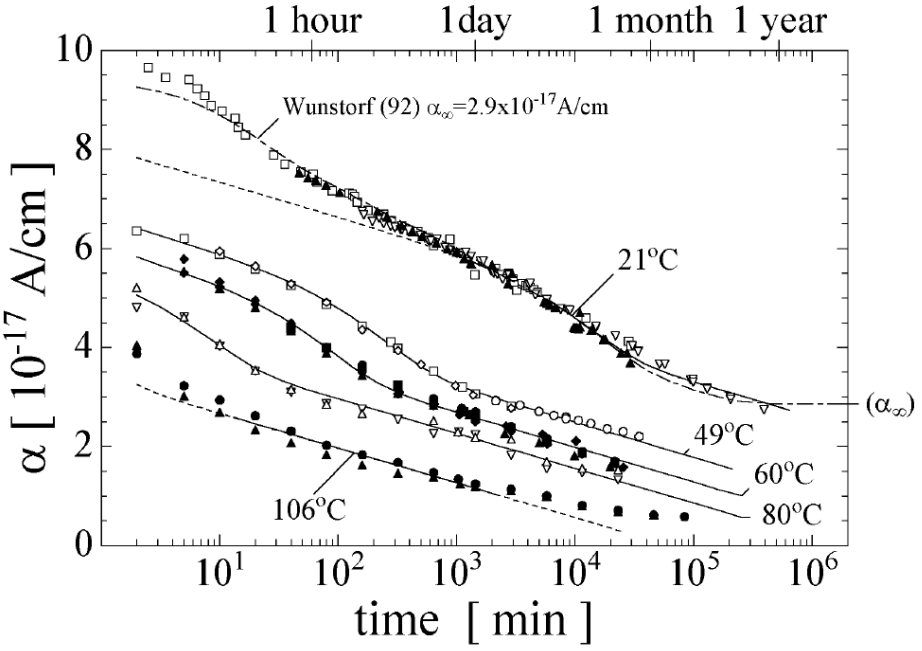


**Figure 4.6:** Annealing results which drive the empirical fit of Equation (4.9). Data is plotted for a series of annealing temperatures, but only the 21°C results are considered for this study. Reproduced from [111].

$$\alpha(t) = \alpha_I \times e^{-\frac{t}{T_I}} + \alpha_0 - \beta \ln(\frac{t}{t_0}) \tag{4.9}$$

where the parameters are defined in Table 4.2.

| Parameter | Value |
|---|---|
| $\alpha_I$ | $1.23 \times 10^{-17}$ A/cm |
| $T_I$ | $1.4 \times 10^4$ minutes |
| $\alpha_0$ | $7.07 \times 10^{-17}$ A/cm |
| $\beta$ | $3.29 \times 10^{-18}$ A/cm |
| $t_0$ | 1 minute |

**Table 4.2:** Parameters for Equation (4.9), for an $\alpha$ value at T=273+21 °K.

In practice, due to the granularity of the IV scans, an approximation is made that the total luminosity between two scans is injected in a single $\delta$-function, halfway between the two scan periods. This approximation takes advantage of LHCb's luminosity levelling, which provides for a relatively constant radiation damage profile over time. For example,

if in a week between two IV scans, there are 10 LHC fills for a total integrated luminosity of 300 pb$^{-1}$, this will be modelled as a single fill of 300 pb$^{-1}$ halfway between the two scans, and the annealing time is half of the operational time of the sensors between these two scans. The operational temperature is taken to be $-8.3$°C. The uncertainty on this method is considered in Section 4.2.8. This approximation allows for a simplification in the annealing calculation.

The time spent annealing is normalised to the 21°C annealing equivalent, which can then be used to calculate, using Equation (4.9), the $\alpha$ value described in Equation (4.5). This calculation is performed using Equation (4.10) [111]:

$$k = e^{-\frac{E_a}{kT_1}} / e^{-\frac{E_a}{kT_2}} \tag{4.10}$$

where $k$ is Boltzmann's constant, the activation energy, $E_a$, is $1.31 \times 1.6 \times 10^{-19}$ Joules, with the temperature being extrapolated from $T_1$ to $T_2$. This represents the scaling of annealing at -8.3 °C to an equivalent annealing at 21 °C. This $k$-factor[†] is then incorporated by scaling the amount of time spent at $T_1$ and multiplying it by the scale-factor

$$t_{T_2} = k \times t_{T_1} \tag{4.11}$$

where the quantities $t_{T_i}$ represent the time spent annealing at temperature $T_i$. The $k$-factor is calculated with reference to +21°C. There are four periods of significant *fast* annealing taken into account in this analysis, with the addition of operational annealing i.e. allowing for the annealing effects when running the silicon sensors at their nominal data taking temperatures. Fast annealing refers to periods where the detector is warmer than its typical operational temperature, thus inducing rapid annealing effects. A summary of the most significant annealing periods is presented in Table 4.3. Figure 4.7 illustrates the fourth annealing period in Table 4.3, from the control system.

### 4.2.5 Current Voltage (IV) Scans

Current-Voltage scans are one of the variety of methods available at LHCb to monitor the VELO. It uses the detector control software to perform a high voltage ramp on the sensors, pausing to take measurements of the current and temperatures at pre-

[†]This $k$-factor is not to be confused with the one used in the analysis later for scaling from LO to NLO ratios.

| Period | Date | Temperature °C | Time | $k$-factor |
|---|---|---|---|---|
| 1 | Christmas 2010 | +21 | 40 days | 57600 |
| 2 | 28th March 2011 | +21 | 6 hours | 360 |
| 3 | 29th April 2011 | +21 | 4 hours | 60 |
| 4 | 6th July 2011 | +5 | 4 hours 30 minutes | 13.8 |
| 5 | Operational | -8.3 | 1 hour | 0.20 |

**Table 4.3:** The different annealing periods in the data range presented, and how they are modelled.

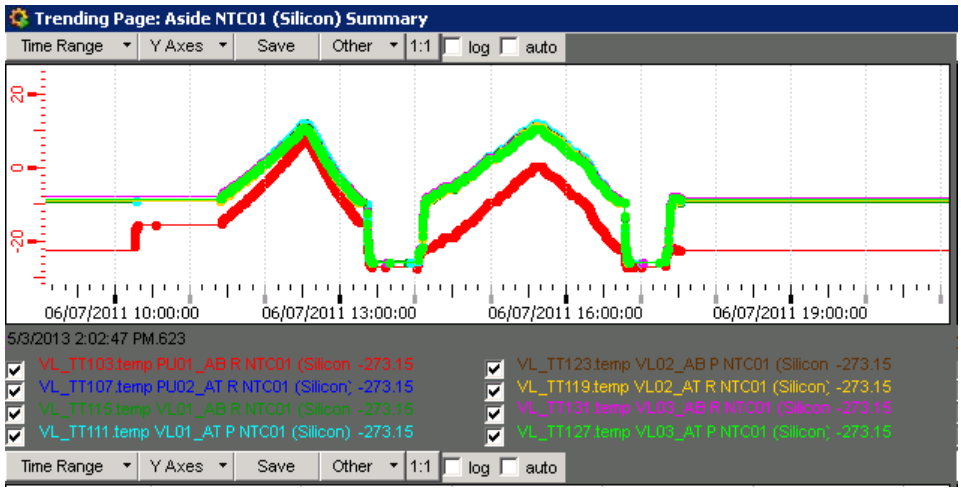


**Figure 4.7:** A thermal plot from the control system for the fourth annealing period studied in this analysis, the approximation is made that it corresponds to 4 hours and 30 minutes of +5°C annealing.

selected steps. The scans are performed nominally once every two weeks, but the scan is comparatively quick, requiring 15 to 20 minutes, and can be done between an LHC beam and injection. The ability to perform these scans quickly is also used for control studies, such as performing an IV scan before and after a fast annealing period without additional luminosity being delivered. The scans for the data period, which cover from May 2010 to end of running 2011, are carried out from 0 V to 150 V in 10 V steps, with the ramp up to 150 V and the ramp down back to 0 V stored.

The use of currents, and their relative changes, allow for understanding of the environment the VELO is exposed to, and provides information vital for future decisions such as annealing strategy, lifetime estimates, or setting operational voltages.

### 4.2.6 Measurements

The IV results are presented at the voltage of 150 V which corresponds to the operational voltage for these sensors[‡] during the time period analysed. The current at this voltage can then be plotted as a function of several parameters such as the number of days elapsed since $t_0$, which corresponds to the start time (11th of May 2010). An example of this is provided in Figure 4.8, where the trend in the majority of the sensors is clear. The temperatures correspond to the temperature sensor (NTC-2) at the closest point to the silicon active region, and this allows for correcting the temperature variation from sensor to sensor.

The location of the NTC sensors are illustrated in Figure 3.15. They are corrected to a value of -11.6 °C, which is the mean temperature of the NTC temperatures in a control environment. The first step is to "smooth" out current fluctuations arising from temperature variations between sensors, which is performed by this normalisation.

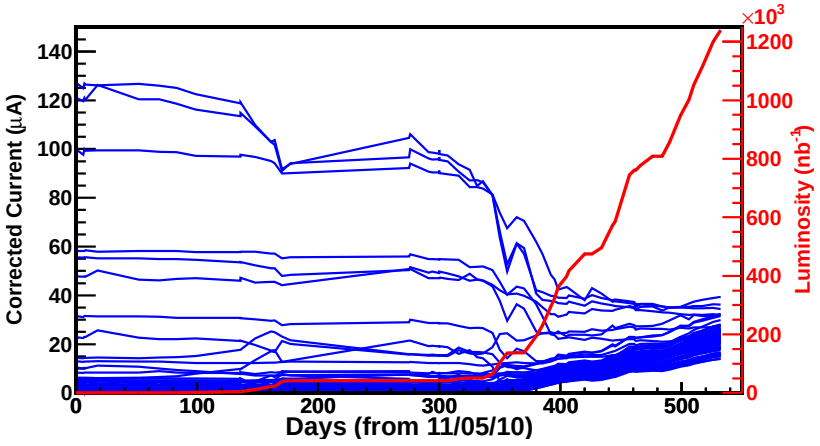


**Figure 4.8:** The current of all sensors at 150 V (blue) versus the delivered luminosity (red) over the analysed time period. The x-axis represents the number of days elapsed relative to the first scan used.

It is possible to plot the corrected sensor currents as a function of the luminosity delivered, as shown in Figure 4.9. The rapid decrease in the high current sensors with irradiation can be observed, as they tend to normal behaviour. The sensors that present high initial current correspond to the surface damaged sensors.

[‡]Please note that three sensors, VL04CB (to 70 V), VL16CB and VL23CT (100 V) were dropped to lower operational voltages for the 2010 period.

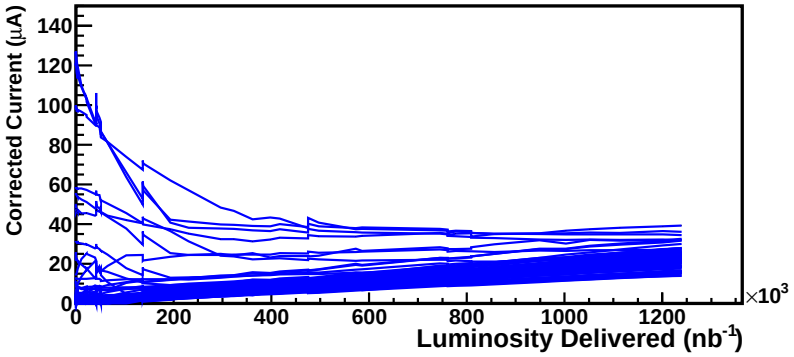


**Figure 4.9:** The current of all sensors at 150 V (blue). The x-axis represents the total luminosity delivered to the detector.

The scans can be analysed with finer granularity, as previously discussed. Due to the $\alpha$ value being measured at +21°C, the predicted currents are calculated for this value and then normalised by Equation (4.8) to -8.3°C which is the nominal operating temperature. The temperature approximation from +21°C to -8.3°C also introduces the largest source of uncertainty.

### 4.2.7 Current Calculations Without Annealing

It is possible to predict the currents a sensor would have without accounting for the accelerated annealing or the operational annealing. The unannealed calculations are simple and provide a starting point for choosing the operational temperature of the sensor. For example, if the sensor is run at too high a temperature, then the currents during irradiation will reach their operational limits much faster than if a lower temperature is chosen.

These calculations are performed for three representative different sensors, corresponding to one upstream (VL01AB), one close to the IP (VL07AT), and one downstream (VL25AT), in Table 4.4. For this calculation an $\alpha$ value of $10 \times 10^{-17}$ A/cm is used.

It is possible to look at the impact of the fast annealing (accelerated annealing due to temperatures exceeding standard operation) on the current predictions and the VELO operation. This is performed by running the model including only the operational

| Sensor | A (1 MeV $n_{eqv}/fb^{-1}$) | $\beta$ | $\Delta$I unannealed ($\mu$A) | $\Delta$I ($\mu$A) | $I_{meas}$ ($\mu$A) |
|---|---|---|---|---|---|
| VL01AB | $2.62 \times 10^{13}$ | 1.72 | $31.7^{+4.0}_{-3.5}$ | $21.2^{+2.6}_{-2.4}$ | $21.5 \pm 0.5$ |
| VL07AT | $3.49 \times 10^{13}$ | 1.88 | $37.9^{+4.7}_{-4.2}$ | $25.3^{+3.2}_{-2.8}$ | $27.1 \pm 0.5$ |
| VL25AT | $1.86 \times 10^{13}$ | 1.64 | $23.7^{+3.0}_{-2.7}$ | $15.8^{+2.0}_{-1.8}$ | $15.7 \pm 0.5$ |

**Table 4.4:** Comparisons between current predictions with and without annealing, as well as measured values.

annealing periods. The result of this study is that the inclusion of the fast annealing periods makes a $\sim$ 2% impact on the basic current calculations. The $\alpha$ value, as can be seen in Figure 4.6, decreases proportionally to log $t$, thus after an initial period of fast changes in $\alpha$, the rate of decrease diminishes significantly. The results of this study are presented in Table 4.5.

| Sensor | $\Delta$I operational ($\mu$A) | $\Delta$I full ($\mu$A) |
|---|---|---|
| VL01AB | $21.4^{+2.7}_{-2.4}$ | $21.2^{+2.6}_{-2.4}$ |
| VL07AT | $25.6^{+3.2}_{-2.9}$ | $25.3^{+3.2}_{-2.8}$ |
| VL25AT | $16.0^{+2.0}_{-1.8}$ | $15.8^{+2.0}_{-1.8}$ |

**Table 4.5:** A comparison of the effects of the full operational and fast annealing in contrast to just the operational annealing.

### 4.2.8 Model Uncertainty

The simplification of the delivery of luminosity to the detectors introduces an uncertainty. Where, for example, 100 $pb^{-1}$ of data may be taken between two IV scans with a total of 100 hours of operational time, the model is to assume this as 100 $pb^{-1}$ with 50 hours of operational annealing. This uncertainty is estimated by increasing the granularity by 100 times. In the previous example, it would now be modelled as 100 injections of 1 $pb^{-1}$ after every operational hour. The calculations performed with the increased granularity, due to the requirement of re-calculating the current change for every injection, quickly approaches the order of minutes per sensor. An alternative estimation is utilised to simplify the computational intensity of the higher granularity.

A bin-by-bin correction mechanism is used, where a comparison in predicted currents is made between the high granularity and low granularity models to produce scale-factors for each scan period. The bin-by-bin corrections have an average value of 0.988, with a

maximum deviation from this value of 0.017. The uncertainty on the bin-to-bin correction is small compared to the luminosity uncertainty, and thus is neglected.

### 4.2.9 Sensor Classification

The VELO sensors are classified into three categories with distinct behaviour to simplify the comparison of data with a meaningful theoretical model. The characteristics of these are documented in the following pages, as well as definitions of the criteria for the categories. A summary of the different categories of sensors, and the number of occurrences of each category is listed in Table 4.6.

| Category | Number of Sensors | Proportion [%] | Action |
|---|---|---|---|
| Normal | 73 | 86.9 | Kept |
| High Production Current | 8 | 9.5 | Removed |
| Anomalous | 3 | 3.6 | Kept |

**Table 4.6:** The three different categories of sensors, and the proportion of sensors in each category.

#### Normal Behaviour

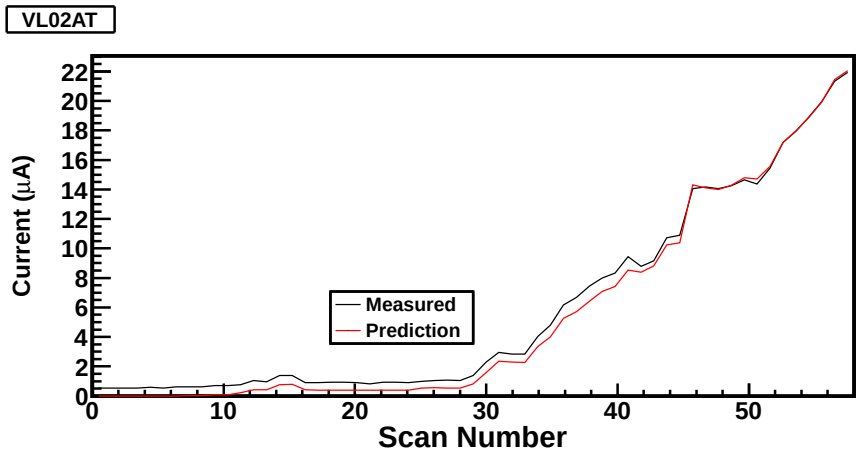


**Figure 4.10:** A sensor that displays normal operational behaviour. This is characterised by compliance to the radiation damage model.

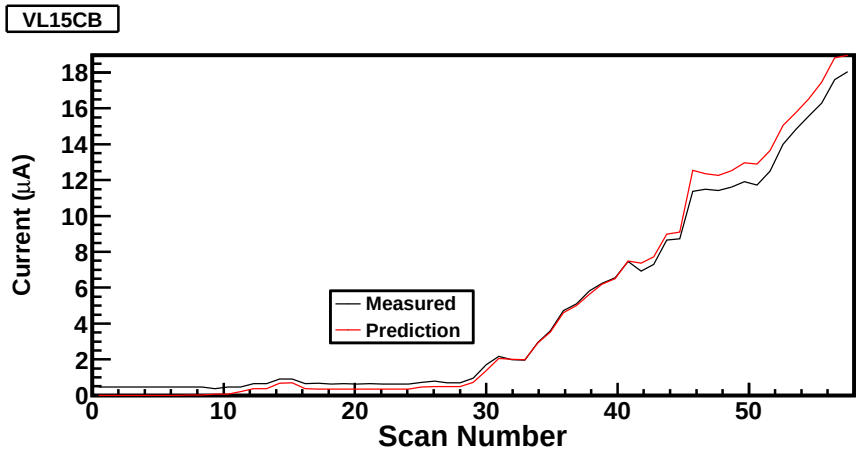


**Figure 4.11:** A second example of a sensor which has normal operational behaviour.

Sensors with *normal* behaviour are characterised by having low initial current, and subsequently following the current predictions. It is important to note that the power supply used is not optimised for low current measurements, so certain sensors may initially have artificially large measured currents. As the currents increase with radiation damage, they can be measured well. Two examples of these are presented in Figure 4.10 and Figure 4.11.

### High Production Current Sensors

*High current* sensors are defined as having a higher current at installation than the final IV scan. These were known to be faulty at production, but were tested under photon irradiation and improvements were observed. Therefore the decision was taken to install them into the experimental environment, with the expectation that they would function as anticipated after sufficient irradiation. Two examples of this are included in Figure 4.12 and Figure 4.13. A total of 8 sensors are found to qualify under this category, and the full list of affected sensors are presented in Table 4.7.

### Other Anomalous Behaviour

Three remaining sensors are grouped into the remaining anomalous category. These are defined as the sensors with significant variances from ideal behaviour, but do not

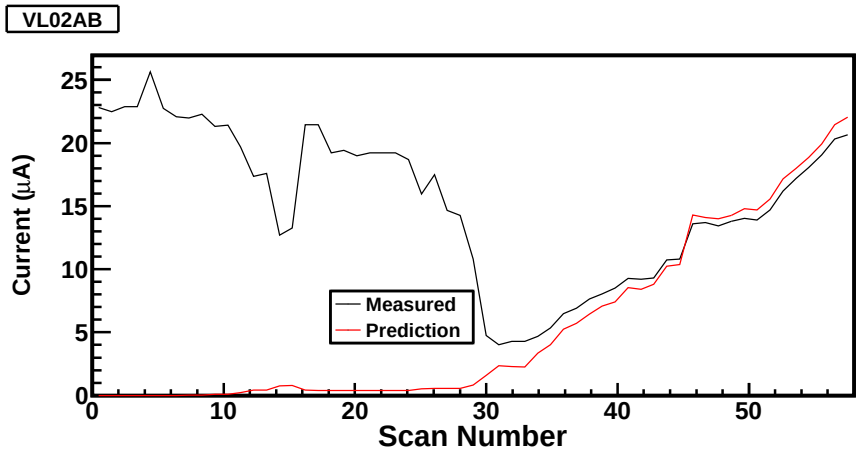


**Figure 4.12:** A sensor displaying unusual behaviour. This is characterised by having a high production current, which subsequently falls with irradiation rather than increasing.

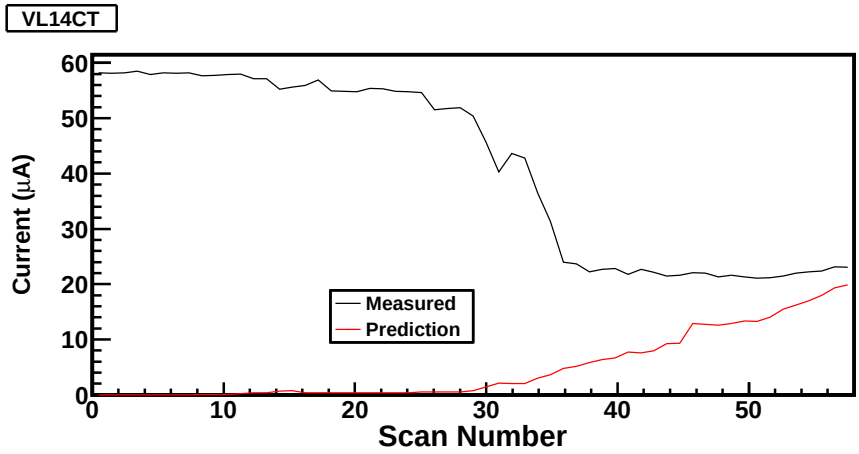


**Figure 4.13:** A second example of a sensor with anomalous current behaviour, with significant decrease with irradiation before tending towards the ideal model.

| Sensor | $I_i$ [$\mu$A] | $I_f$ [$\mu$A] |
|---|---|---|
| VL01AT | 48.3 | 39.8 |
| VL02AB | 23.3 | 20.8 |
| VL01CT | 123.7 | 35.6 |
| VL10CB | 102.1 | 37.2 |
| VL14CT | 59.5 | 23.6 |
| VL14CB | 130.0 | 33.0 |
| VL24CT | 32.2 | 20.6 |
| VL24CB | 56.8 | 27.6 |

**Table 4.7:** All eight sensors removed from the sample for having high production currents. Their initial currents and final currents are also listed.

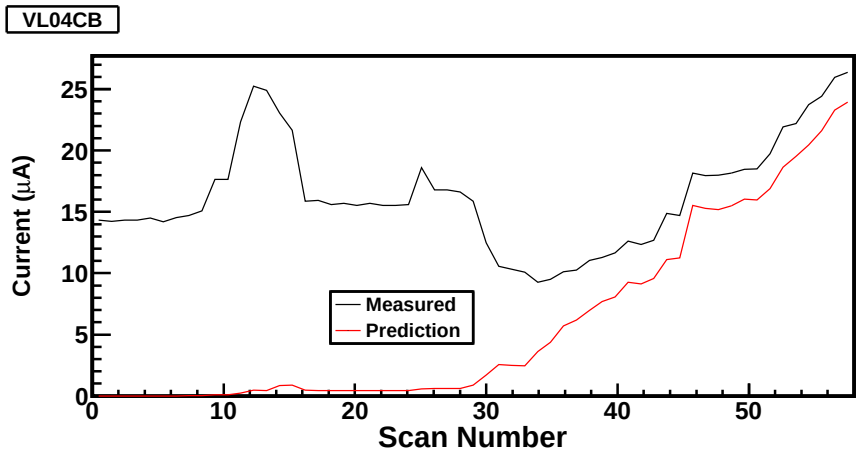


**Figure 4.14:** A few remaining sensors display very unexpected behaviour. For example this one here shows significant current increase during low levels of initial irradiation, before a decrease during a technical stop, and subsequently progressing towards typical behaviour.

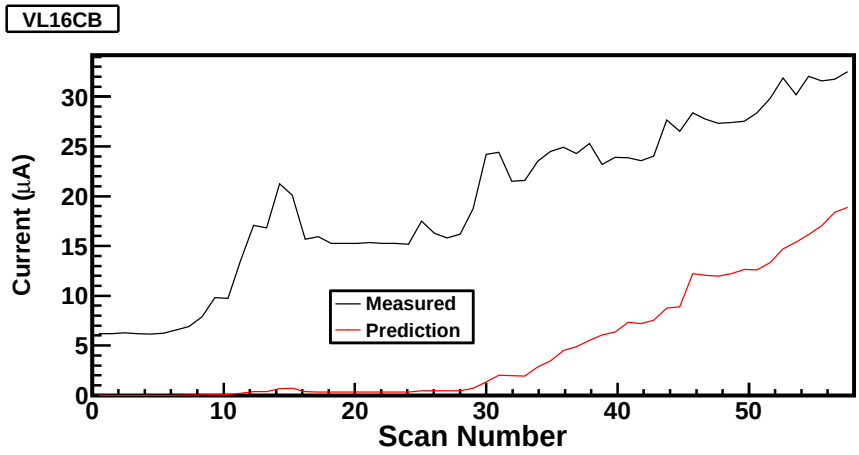


**Figure 4.15:** This anomalous sensor shows rapid increase with initial irradiation, and subsequently displays a large offset to the predicted current, but follows the anticipated gradient.

satisfy the high production current sensor criteria. One possible explanation is that the two sensors (Figure 4.14 and Figure 4.15) display surface oxide charge saturation, which subsequently discharges over time. The characteristic features often present in the scans are a decrease in the current whilst receiving no additional luminosity or fast annealing periods. A more detailed discussion on surface oxide charges, and its causes and effects, may be found in [113–115].

### 4.2.10 Systematic Uncertainties

The most significant systematic uncertainty in this analysis is the temperature extrapolation from the NTC2 temperature used to the silicon temperature. This is calculated from [89] to be $\Delta T = 1.1°\text{C}$, which is estimated from the variance of the thermal difference between the silicon temperature and the NTC2 temperature. The contribution of this uncertainty is calculated by extrapolating the current to $T + \Delta T$ and $T - \Delta T$. The full distribution of $\Delta T$ is available in Figure 4.16.

A source of systematic uncertainty is the difference between the average NTC temperature in the test environment and the experimental environment, which obtains a result of 1.1°C. The distributions for both of these are presented in full in Figure 4.17 and Figure 4.18.

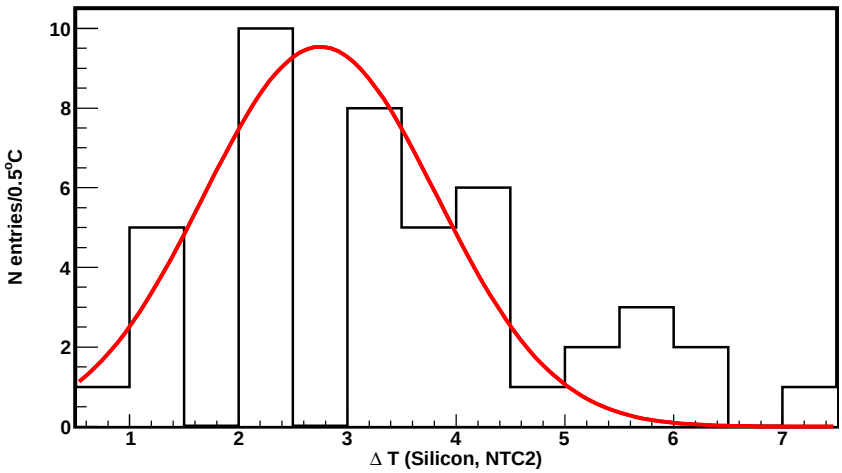


**Figure 4.16:** The temperature difference between silicon and NTC2, data sourced from [89]. A Gaussian is fitted with a mean of +2.8°C and a width of 1.1°C. The empty bins reflect a problem in the readout of NTC2 in the assembly of the modules and is not physical.

The extrapolation temperature for the thermal fluctuations is set to the NTC average temperature in the test environment, of -11.6°C. This is done so it may be compared to the silicon temperature in the test environment, which is the only source of data for a direct measurement of the silicon temperature. The mean silicon temperature in the test environment is found to be -8.3°C. The silicon temperatures for the test environment are presented in Figure 4.19.

A fluence uncertainty is taken of 8% [107] arising from the uncertainties of the composition of the fluence that the sensors are exposed to, and a luminosity uncertainty of 5%. Only the temperature extrapolation uncertainty is plotted on the histograms. The previously mentioned two sources of uncertainties are added in quadrature with the thermal uncertainty, to result in an increase from approximately 20% to 22%. A further source of uncertainty arising from the VELO in/out time, where the irradiation profile is difficult for when the VELO is in the open position, can be assigned from the LHCb Run Database [116], which is taken from the inefficiency time on "VELO IN", which is $\sim 1\%$ for the time period in question. A summary table of all the uncertainties considered is listed in Table 4.8.

The annealing effects of the silicon when not in data taking mode (i.e. when the chips are not powered) is ignored, as the contribution of annealing at $-30$°C is insignificant

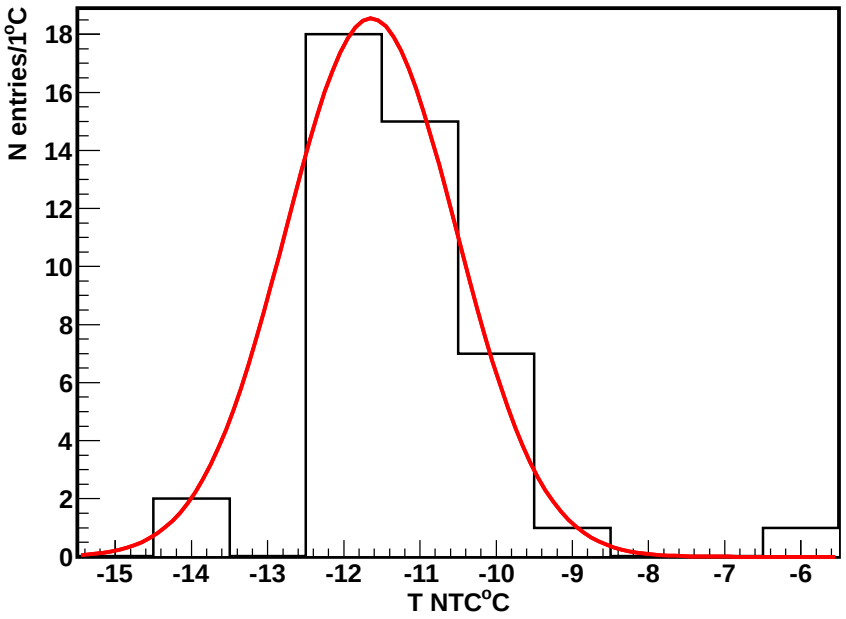


**Figure 4.17:** The NTC temperature distribution in the test environment. A mean value is obtained of -11.6°C.

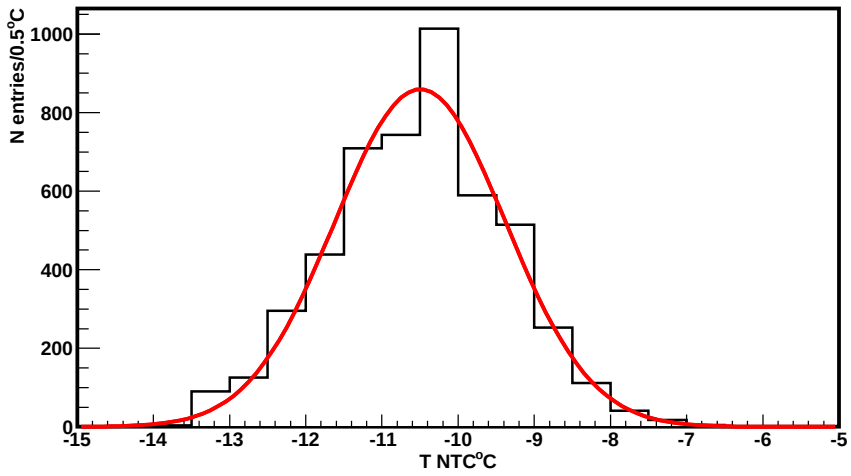


**Figure 4.18:** The NTC temperature distribution in the experimental environment for the full data sample. A mean value is obtained of -10.4°C.

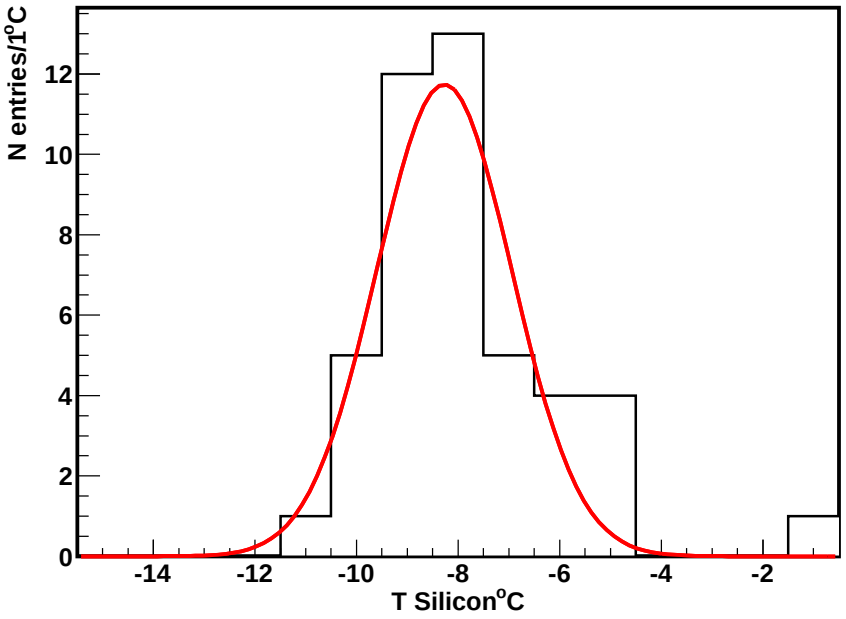


**Figure 4.19:** The silicon temperature in the test environment. A Gaussian is fitted to obtain a mean of -8.3°C.

compared to that of the data taking mode of approximately −8.3°C, with 1 minute at the warmer temperature equating to approximately 161 minutes at −30°C.

| Source | Value affected | Estimated uncertainty | Uncertainty on current |
|---|---|---|---|
| VELO In | Luminosity | ± 1% | ± 1% |
| Luminosity | Luminosity | ± 5% | ± 5% |
| Fluence | Luminosity | ± 8% | ± 8% |
| ΔT(NTC,Si) | Temp. comp. | ± 1.1°C | +13% -11% |
| ΔT(test,exp) | Temp. comp. | +13% -11% | |
| Total uncertainty | $I_{pred}$ | | +21% -18% |
| Total uncertainty | $I_{meas}$ | | ± 0.5 $\mu$A |

**Table 4.8:** A summary table of the dominant systematic uncertainties in this analysis.

### 4.2.11 Results

Using the annealing equation Equation (4.9), the VELO radiation damage model Equation (4.6) and the temperature compensation calculation Equation (4.8), it is possible to

calculate predicted currents as the sensor undergo changes from radiation damage. The results for all sensors in the experiment and the predicted current $\pm 1\,\sigma$ is presented in Figure 4.20.

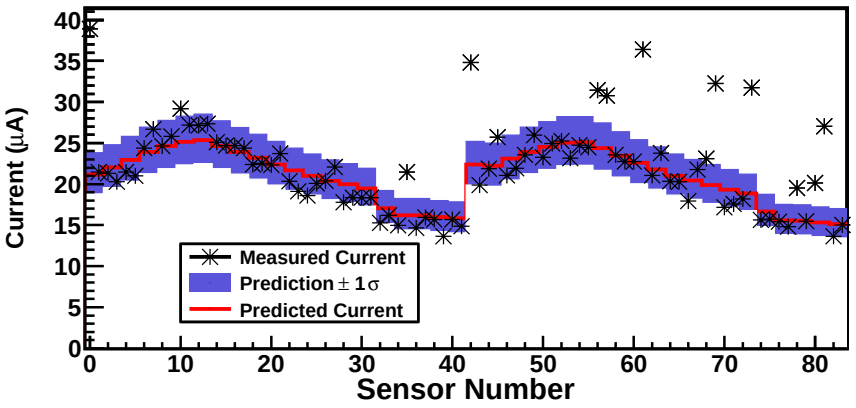


**Figure 4.20:** The predicted currents against the measured currents for all VELO sensors. Sensors 0→41 correspond to the A side, and 41→83 correspond to the C side. The interaction point is at $\sim 12$ and $\sim 53$.

A few anomalies are found corresponding to sensors with high currents at production, and these are removed from the data sample. The previous plot, with these anomalous sensors removed, is presented in Figure 4.21. The average "pull" of the sensors, with respect to the theoretical prediction, is presented in Figure 4.22.

A Gaussian is fitted with a mean of -0.31 and a width of 0.52. An ideal Gaussian would have parameters of mean=0.00 and width=1.00. The smaller fitted width when compared to the ideal Gaussian is an indication that the thermal extrapolation uncertainty has been overestimated in this analysis. The offset in the pull strongly suggests an unknown systematic shift. For example, if the luminosity was underestimated by 5%, then this could give rise to an offset in the mean. Another potential source of uncertainty: the differences in the test environment and the experimental environment, could also contribute to this observed effect. In the test environment the cooling cookies were designed to be removable, whereas in the experimental environment the cooling cookies are fixed in place. This could potentially change the thermal profile of the detector in the operational environment. Further possible sources include the "self-cooling" of the modules in-situ, where in the test environment the modules were housed in a room temperature vacuum tank, in contrast to the experimental environment where they are

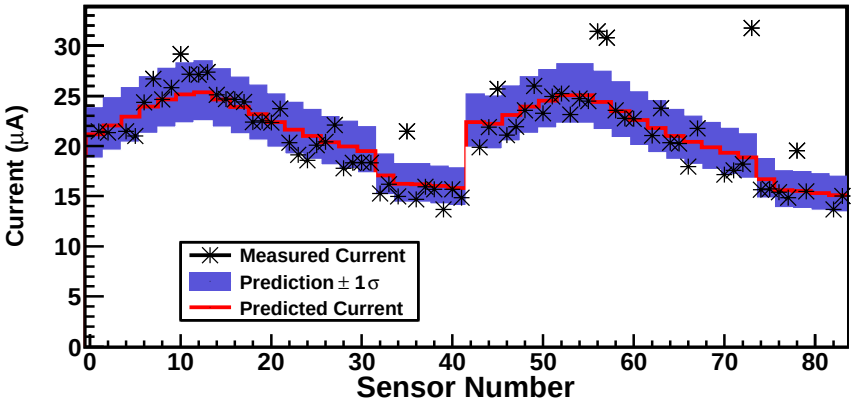


**Figure 4.21:** The predicted currents against the measured currents for all VELO sensors, with any sensors satisfying the anomalies requirement removed. The $x$-axis displays all the sensors on the two halves of the detector, the A-side followed by the C-side respectively.

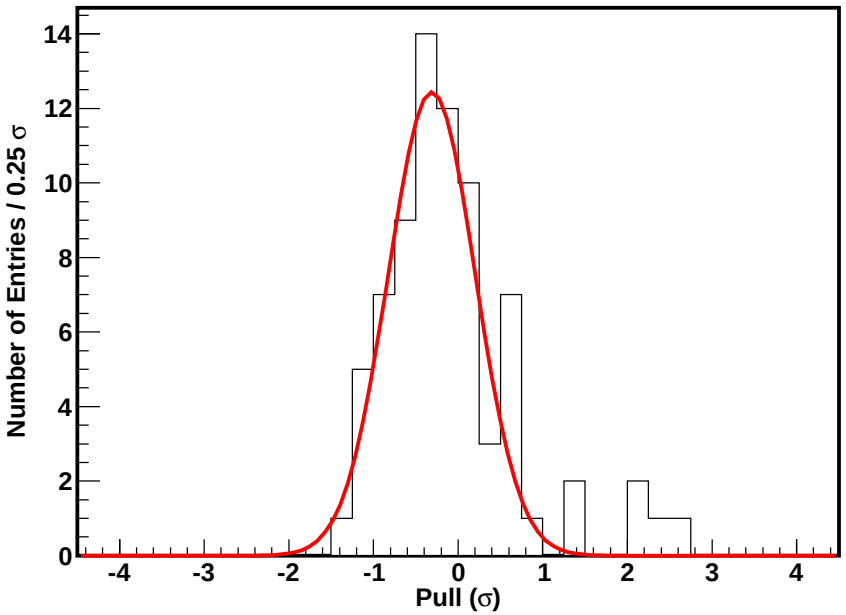


**Figure 4.22:** The pull of variation observed in the sensors, with the anomalous sensors removed. Only the thermal extrapolation uncertainty is considered. A Gaussian is fitted to test the quality of the data.

in close proximity to other cooled modules. The observed off-set is consistent with a $\sim 0.5$°C cooler experimental environment hypothesis.

### 4.2.12 Outlook

It is possible to calculate projections for the long term operation of the VELO. Using the data starting from the last significant annealing period, it can be calculated that an approximate annealing factor of 2.2 seconds of +21°C of annealing per 100 pb$^{-1}$ of luminosity. Using this quantity, and assuming no fast annealing periods, projections may be calculated for the VELO after a total of 6 fb$^{-1}$ of delivered luminosity, using the data current to the 1.239 fb$^{-1}$ already delivered. The choice of 6 fb$^{-1}$ corresponds to anticipated lifetimes during the construction of the VELO [117]. The projections are presented in Figure 4.23. The currents are also compared to naive predictions without annealing from operation considered for the additional delivered luminosity, in Table 4.9. The comparison shows the importance of the consideration of operational annealing in projective models. Under the bin-by-bin correction method, the current sensors are corrected using a value of 0.988 (the average correction value) for the projections.

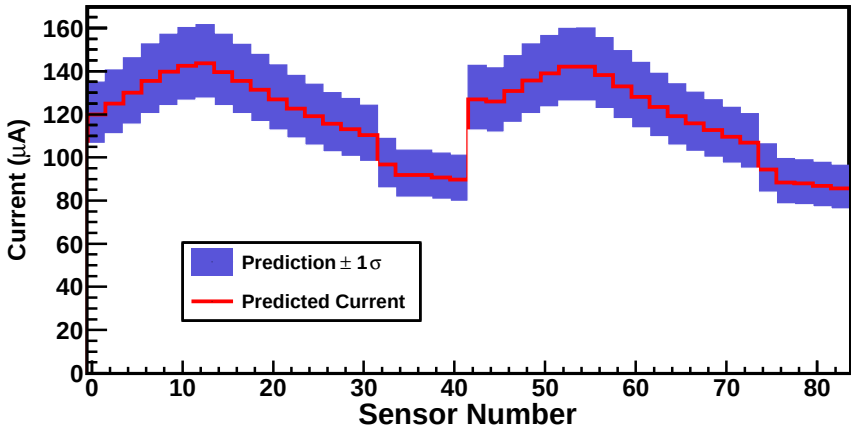


**Figure 4.23:** Prediction for currents after a total of 6 fb$^{-1}$ of delivered luminosity. Only thermal uncertainties are plotted.

It can therefore be anticipated that after 6 fb$^{-1}$ of total delivered luminosity, the anticipated depletion voltage is $< 400$ V [117] where the approximate currents of the sensors range from $\sim 90 \rightarrow \sim 150$ $\mu$A. This is within the operational range of the power

| Sensor | Predicted Current ($\mu$A) | Unannealed Current ($\mu$A) |
|---|---|---|
| VL01AB | $120.0^{+15.0}_{-13.4}$ | $172.8^{+21.6}_{-19.4}$ |
| VL07AT | $143.6^{+18.0}_{-16.1}$ | $206.8^{+25.9}_{-23.2}$ |
| VL25AT | $89.7^{+11.2}_{-10.1}$ | $129.2^{+16.2}_{-14.5}$ |

**Table 4.9:** Current predictions for three sensors after 6 fb$^{-1}$ of delivered luminosity.

supply. This limit can further be enhanced by utilising additional fast annealing on an as-needed basis.

It is estimated from simulation [118] that the VELO sensors go into thermal runaway at $\sim 1 \pm 0.2$ mA. Thermal runaway is the result of large Ohmic heating of the sensors, causing the temperature of the sensor to increase, resulting in a larger current, in a positive feedback loop. A more detailed explanation of thermal runaway can be found in [83]. The model detailed above is used to project the point at which the VELO would reach currents of 1 mA. The results of this are presented in Figure 4.24, where a delivered luminosity of 50 fb$^{-1}$ is used. The detector currents at this point range from $\sim 680$ $\mu$A $\rightarrow$ $\sim 1.08$ mA. The highest current sensors are $\sim 0.6\sigma$ above the 1 mA threshold. Note that this projection is exclusively for the currents, and does not consider the depletion voltage or thermal stability of the modules[§].

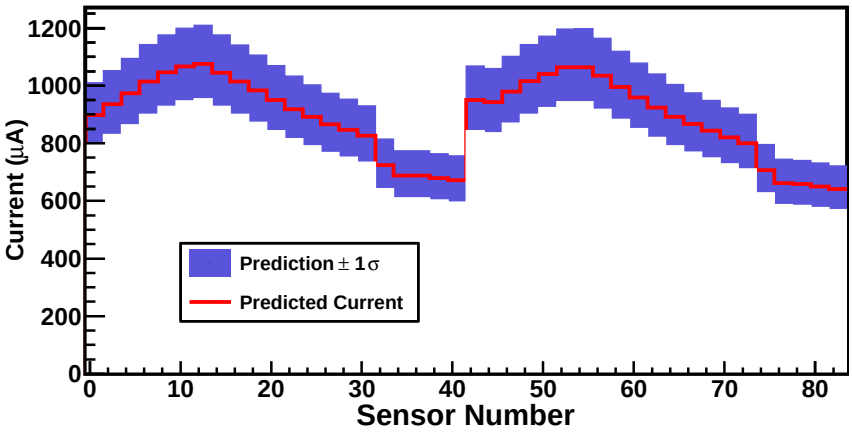


**Figure 4.24:** Predictions for currents after a total of 50 fb$^{-1}$ of delivered luminosity. It is estimated that 1mA is approximately the regime where the VELO sensors go into thermal runaway.

[§]The increased currents could potentially result in the VELO silicon temperatures being warmer than they are during operation now. This would in turn increase the current.

### 4.2.13 Summary

It is found that the model implemented for the description of the effect of radiation damage upon the IV performance of the sensors is consistent with the observations in data. The implementation of the run time annealing makes a significant impact on the predictions with regard to the sensors. Some anomalous sensors manifest as having a high current at production, were removed to enhance the purity of the sample with respect to the subset of "ideal" sensors. It is found that the samples correspond well with the model expectations for the sensors, with most "ideal" sensors falling within $\pm 2\sigma$ of their expected current values.

The predictions are found to agree well with the data anlysed, and therefore they can be utilised to generate predictions for future operation of the VELO. It is anticipated that after a total delivered luminosity of 6 fb$^{-1}$, the sensors operate at a depletion voltage of $<$400 V, and a current range between 90 and 150 $\mu$A. These values are within the operational limits of the power supply. It has also been estimated that the sensors can survive a total of $\sim$50 fb$^{-1}$ of delivered luminosity before reaching their thermal runaway limits.

# Chapter 5

# Particle and Jet Reconstruction

Reconstruction is the mechanism of processing electronic signals from individual sub-detectors and utilising the information to reconstruct the particles, or energy flow, within each event. This is accomplished by means of two separate categories of algorithms, known as *online* and *offline*. The first, the *online* algorithms, are designed to be used during data taking. They act upon information stored temporarily from the detector, and are focused on basic particle reconstruction and providing information for the decision making process as to whether an event should be stored or ignored. Offline algorithms are designed to process data which has already been stored to perform complete particle reconstruction with all the available detector information and to provide the highest quality final state information possible. The chain of particle reconstruction is first described, followed by a description of the three stage trigger system in LHCb, and then the packages available in LHCb for both offline data analysis and event simulation.

## 5.1 Reconstruction

### 5.1.1 Track Reconstruction

As charged particles travel through the tracking stations of LHCb, they leave *hits* along their path as they interact with the sub-detectors. These hits can then be used to reconstruct the motion of travel of the original particle by being fit to a trajectory. Using this trajectory, for tracks in a magnetic field, the momentum of the particle can be measured. The reconstructed path is called a track, which is stored as a set of *states*. The states record the tangential information of the particle's track at various $z$ positions

where sub-detectors make measurements. A state, $\vec{x}$, is defined as:

$$\vec{x} = \begin{pmatrix} x \\ y \\ t_x \\ t_y \\ q/p \end{pmatrix}$$

where $x$ and $y$ are the Cartesian co-ordinates relative to the interaction point representing the origin at $(0, 0)$, the $z$-axis is aligned into the detector along the beam axis, and the $y$-axis in the direction of the magnetic field. The values $t_x$ and $t_y$ are the slopes of the track in the $x$ and $y$ planes respectively, defined as $t_x = \frac{dx}{dz}$ and $t_y = \frac{dy}{dz}$, and $q/p$ is the charge divided by the magnitude of the momentum, where the charge is assumed to be $q$=+/-1.

### Track Reconstruction Algorithms

LHCb uses five different categories of tracks, as illustrated in Figure 5.1[119]. These track definitions depend on which sub-detectors contribute measurements for the reconstructed track, and are listed below:

*Long Tracks*: traverse the full LHCb tracking system, and are optimal for physics analyses due to the full availability of information, providing the most accurate momentum information.

*Velo Tracks*: only have measurements in the VELO sub-detector, which results in no momentum information. They can be used, however, for primary vertex reconstruction. An example of a potential VELO track would be a particle that travels in away from the main detectors.

*Upstream Tracks*: are tracks that have only left hits in the VELO and TT-stations, but do not continue further to the T-stations. These typically occur because a track is outside of the acceptance for the T-stations.

*Downstream Tracks*: are tracks that only leave hits in the TT and T-stations. They can be used, for example, to reconstruct a particle outside of the VELO's acceptance, or to reconstruct a neutral particle which decays after leaving the volume of the VELO.

*T Tracks*: are tracks that only traverse the T-stations. This can occur when, for example, a long lived neutral particle travels through a substantial portion of the detector volume before decaying.

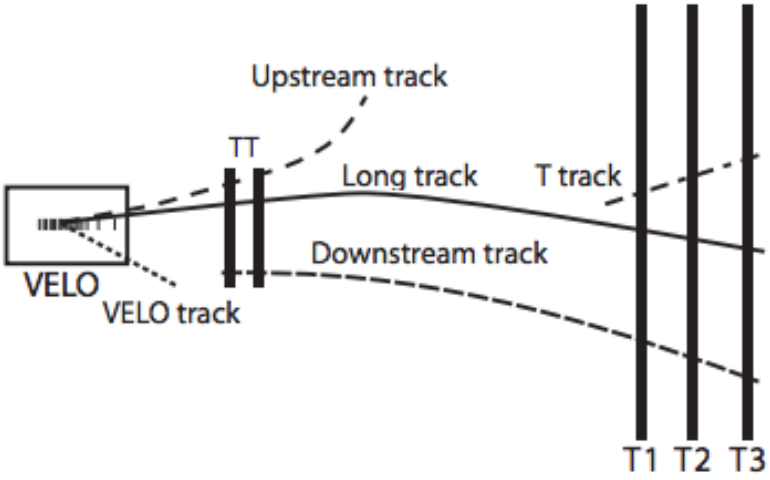


**Figure 5.1:** The five different track types used in LHCb. Reproduced from [119].

A pattern recognition procedure is used to reconstruct the tracks. Six algorithms are implemented to identify the largest possible number of tracks of each variety. The 6 algorithms are documented in the following list:

*VELO Seeding*: The VELO pattern recognition reconstructs two dimensional patterns where hits in sequential sensors are used to create a straight line. This straight line is then extrapolated in both directions to look for other additional clusters. It does not provide momentum information, and can reconstruct both backwards and forwards tracks for PV information. Once tracks are constructed, known as VELO seeds, they can be used as a seed for other pattern recognition algorithms [120].

*T-Station Seeding*: Seeds are formed using the T-stations. Due to the location of the stations after the magnet, tracks are considered in the $x, z$ plane. The resulting track formed is known as a T-Seed [121].

*Forward Tracking*: This algorithm uses the VELO seeds information (before the magnet) and then matched to T-station hits (after the magnet) to measure the momentum of the track. With T-station hits and the VELO seed, it is possible to then define the trajectory [122].

*Upstream Tracking*: Upstream tracking, also known as short tracks, are formed from VELO seeds and TT-station hits. This is performed by taking all VELO seeds, but not assigned to any long tracks, and then matched to at least 3 TT-station hits. [123]

*Track Matching*: This algorithm takes as inputs VELO seed tracks and T-seeds. These are then extrapolated to a central plane in the magnet. If the two extrapolated seed tracks are compatible, then a search is performed for TT-station hits which can be added [124].

*Downstream Tracking*: A downstream track is formed by starting from a T-Seed, and scanning for potentially useful TT measurements around the extrapolated track estimate, which is then used to create the track. This track is then checked against potential matching long tracks [125]. See Figure 5.2 for an example.

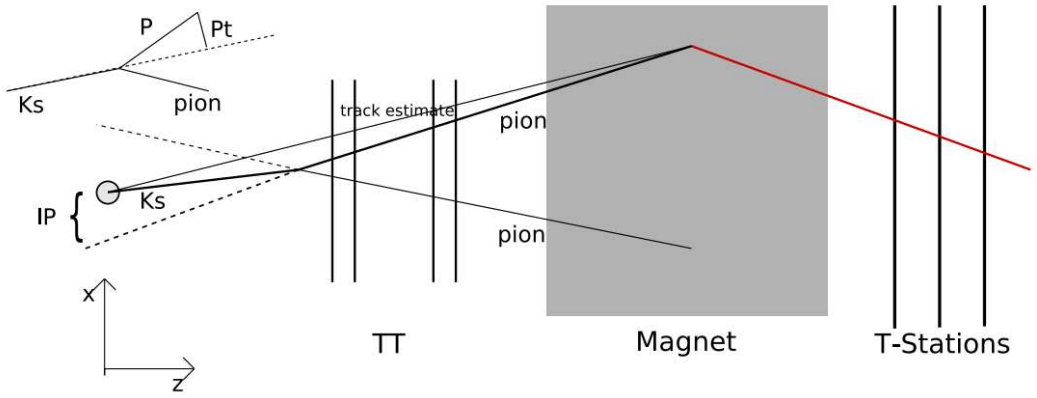


**Figure 5.2:** An example of a downstream track being created from a T-Seed and then extrapolated back with a window of uncertainty, in the example of a $K_s \rightarrow \pi\pi$ decay. Reproduced from [125].

Once a set of measurements have been identified by the pattern recognition, it is then fitted to a trajectory. A Kalman Filter is used to reconstruct the track states at each measurement [126]. The Kalman Filter algorithm is a process iterating over the measurements, and in specific application in particle physics is designed to take into account effects like scattering and material interactions, as well as being designed to discard missing hits [127]. The Kalman Filter was first described in [128], and specific applications to PP experiments can be found in [129].

### 5.1.2 Particle Identification

Particle identification (PID) is the process of taking the previously reconstructed tracks and assigning particle types to them using the PID subsystems. These are the RICH detectors, the muon system and the calorimeters. Different particles will interact in unique ways with certain sub-detectors and the PID process is the utilisation of these different interactions. For example, the RICH detectors can separate pions and kaons of the same momentum. The physics of the sub-detectors is discussed in Section 3.2.3, and this section will discuss the utilisation of information from the sub-detectors to classify particles. This information is subsequently combined to form likelihood variables for the different potential particle hypotheses.

#### Muon Identification

Muons are identified by extrapolating tracks with $p > 3$ GeV/c into the muon stations. The tracks are required to be within the acceptance of M1 and M5. A Field of Interest (FOI) is used to search for hits in each detector, which is parameterised as a function of momenta for each region and station [130]. A track is considered to be a candidate for a muon when a minimum requirement is satisfied, which is defined in Table 5.1 [131].

| Momentum Range (GeV/c) | Required Hits |
|---|---|
| p < 6 | M2+M3 |
| $6 < p < 10$ | M2+M3+(M4 or M5) |
| $p > 10$ | M2+M3+M4+M5 |

**Table 5.1:** List of requirements for forming muon candidates in LHCb.

These conditions create the definition for preliminary muon candidate tracks. After this, a discrimination variable is constructed with the distance from the extrapolated track in each of the muon stations to the closest hit inside the FOI [132].

A further category of muons are introduced, *Loose Muons*, which is designed to increase efficiency. The requirements for this category are defined in Table 5.2 [133]. The efficiency, calculated from a $b$-inclusive sample, is $\epsilon$(Tight Muons) = 95.6 $\pm$ 0.2% and $\epsilon$(Loose Muons) = 97.2 $\pm$ 0.1%. The mis-identification rate for particles with $p > 10$ GeV/C increases from $\epsilon$(MisID-Tight Muons) $\approx$ 2.8% and $\epsilon$(MisID-Loose Muons) $\approx$ 4.9%. A more comprehensive plot as a function of momentum is available in Figure 5.3.

| Momentum Range (GeV/c) | Required Hits |
|---|---|
| $3 < p < 6$ | 2 of M2+M3+M4 |
| $p > 6$ | 3 of M2+M3+M4+M5 |

**Table 5.2:** List of requirements for forming loose muon candidates in LHCb.

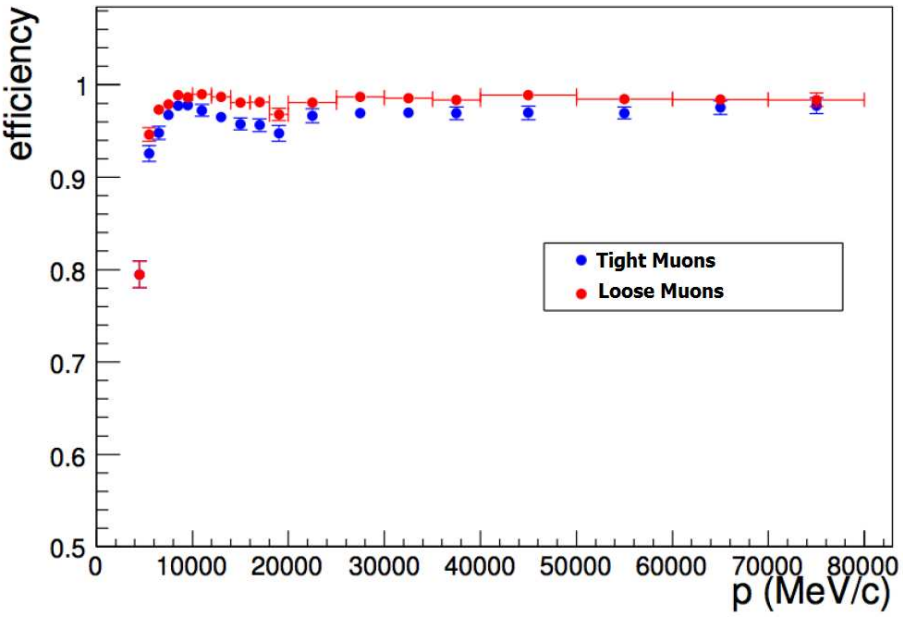


**Figure 5.3:** Efficiency of $\mu$ identification as a function of momentum. Reproduced from [133].

### Photon Identification

In the selection of photon candidate, it is necessary to remove energy deposits which may be associated to reconstructed tracks. The first process is to extrapolate all reconstructed tracks to the calorimeter, and to calculate a parameter to estimate the cluster-track matching, $\chi^2_{\gamma,min}$, for each cluster. This parameter gives the proximity of the closest track extrapolation and the cluster under consideration. It is required that a photon candidate cluster is at least $\chi^2_{\gamma,min} > 4$ to create a photon cluster [134]. These photon clusters are then subsequently used in the electron identification. This is utilised as photons do not leave tracks, whereas the electrons do.

### Electron Identification

Electron identification uses a process similar to the photon identification procedure, by analysing clusters in the electromagnetic calorimeter. An ECAL estimator, $\chi^2_e$, comes from a matching procedure between reconstructed tracks and clusters in the electromagnetic calorimeter. In the first step of the procedure, all reconstructed tracks are extrapolated to the calorimeter, and then the matching procedure is performed. The photon estimator, $\chi^2_{\gamma,min}$ is constructed. Charged clusters are defined as clusters where the estimator $\chi^2_{\gamma,min}$ satisfies the condition $\chi^2_{\gamma,min} < 49$ [135].

Energy corrections are applied for energy losses in materials before the ECAL and dead material between ECAL modules. It is also important to perform identification of electrons with bremsstrahlung photons, which are photons emitted by the electron as it is bent by a magnet, as illustrated in Figure 5.4. Due to the lack of material in the magnetic region, it is possible to accurately predict the location of the bremsstrahlung photons. This is due to the fact that the electron track can be well reconstructed from the VELO, and any bremsstrahlung photon should be collinear with the electron's original direction. Photon candidates are then used in this bremsstrahlung recovery process. Information is further combined from the RICH, HCAL and PRS detectors to construct a likelihood variable. An example of electron identification using information from the RICH is illustrated in Figure 5.5. Due to the required variables for the likelihood calculation for electron identification, and the lack of information on certain variables at higher momenta, it is necessary to construct a custom identification method for high momentum electrons such as those from $W$ boson decays. This identification method is outlined in Section 6.4.4.

### RICH Identification

The RICH detectors identify particles covers a momentum region ranging from 2 GeV/c to $\sim$100 GeV/c. The identification uses the Čerenkov photons registered by the photomultiplier tubes. These are then matched to a track which is extrapolated into the region of the RICH. The patterns are subsequently compared to the expected Čerenkov cone angles for particles with different mass hypotheses, and a likelihood variable is constructed for each hypothesis [137]. The Čerenkov angles for different particles as a function of momentum is presented in Figure 5.6, and an example physics analysis with and without the use of RICH information is presented in Figure 5.7.

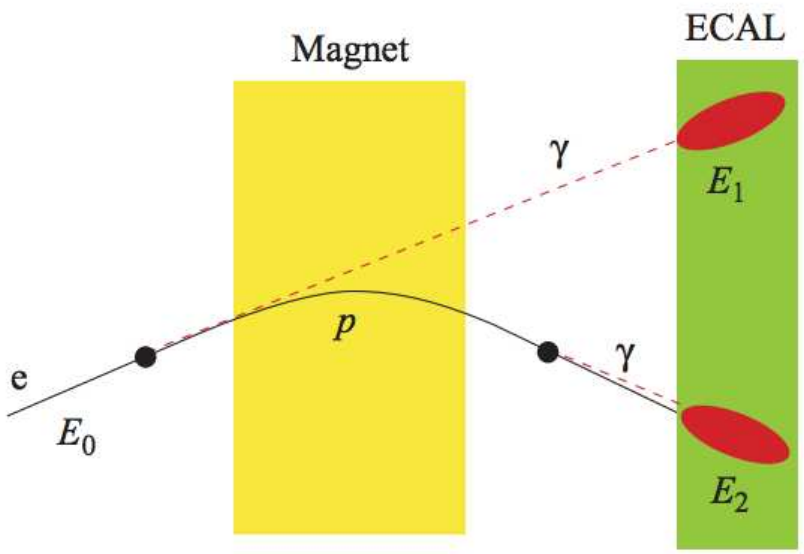


**Figure 5.4:** A schematic diagram of bremsstrahlung recovery. The electron will initially be identified with $E = E_2$, whereas the originating electron had $E_0 = E_1 + E_2$, so it is necessary to add the energy in the photon candidate $E_1$ onto the electron. Reproduced from [90].

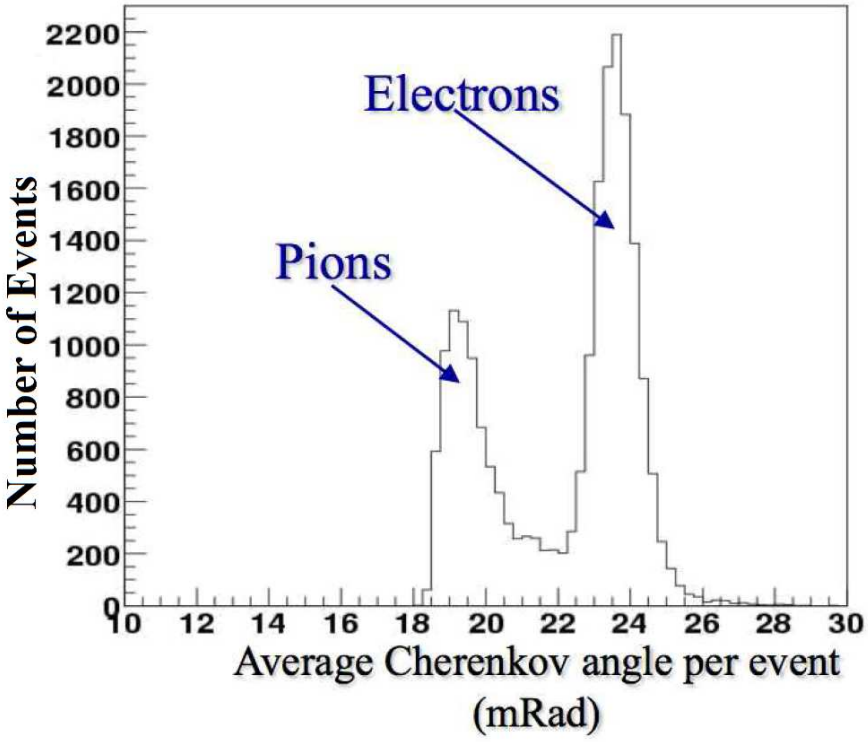


**Figure 5.5:** Electron versus pion separation in the RICH sub-detector. Reproduced from [136].

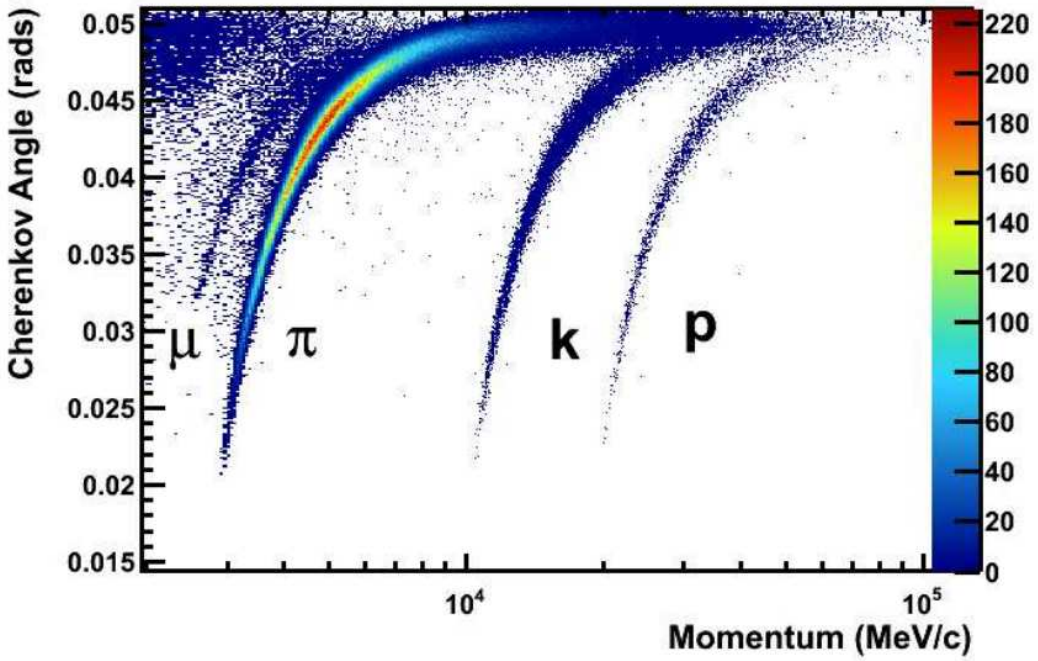


**Figure 5.6:** The angle of the Čerenkov cone for different particles as a function of momentum in $C_4F_{10}$ (the gas in the RICH1 sub-detector). Reproduced from [137].

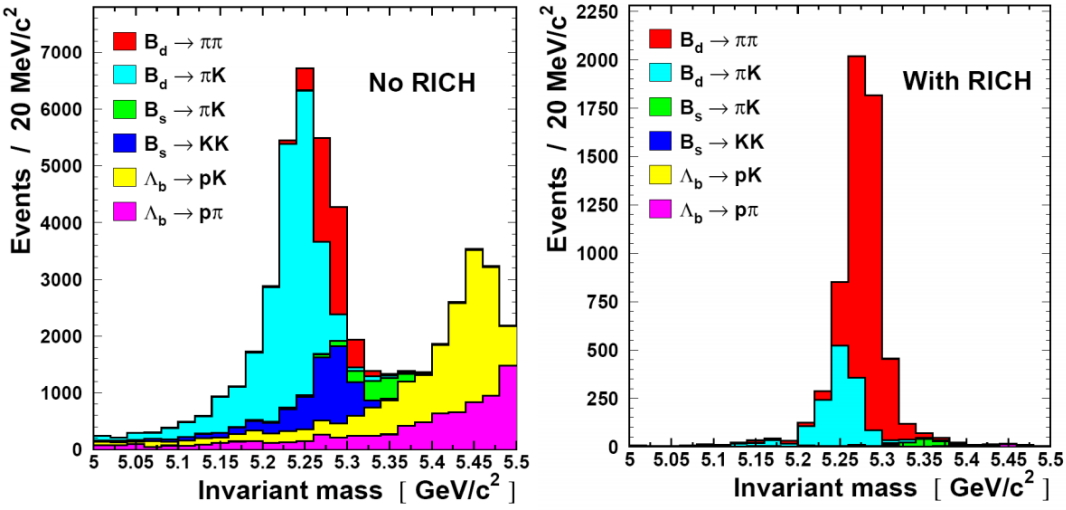


**Figure 5.7:** Several decay modes which result in final states with $\pi$ or K hadrons. Left: Without the use of information from the RICH sub-detectors. Right: With information from the RICH sub-detectors. Reproduced from [136].

## 5.2 Triggers

The trigger in LHCb is a hardware and software system designed to rapidly filter out uninteresting events. This is required as the high collision rate in LHCb, a design rate of 40 MHz, exceeds the limitations imposed by data storage capacity and disk I/O speeds. The LHCb data acquisition system was designed to record events at a rate of approximately 2-3 kHz [138], with a reduction from $\sim$10 MHz arising from a three-tier series of triggers which impose various requirements upon the event [139]. Only events passing all three stages will be recorded. The three-tier triggering system is split into the L0, or Level 0, hardware trigger, and is followed by two separate stages of the Higher Level Trigger (HLT) [90].

### 5.2.1 Level 0 Trigger

The L0 trigger is a hardware level trigger designed to reduce the rate to 1 MHz. It uses four components to make a decision about an event in 3.2 $\mu$s. The four components are the L0 calorimeter trigger, the L0 muon trigger and the pile up system, and the L0 decision unit. The decision unit combines the information from the triggers to make the decision as to whether an event should be stored or not [140].

#### L0 Calorimeter Trigger

The L0 Calorimeter trigger uses information from the SPD, PS, ECAL and HCAL sub-detectors. The SPD, PS and ECAL sub-detectors have the same geometry and are projective*. The L0 Calorimeter trigger computes the transverse energy deposited into clusters of $2 \times 2$ cells, using only cells located in the same zone. Candidates are created for different particle types [140], and the highest transverse energy candidates are used in the trigger decision. The different candidates are as follows:

*Hadron candidates* are formed from the highest $E_T$ HCAL cluster. If there is a highest $E_T$ ECAL cluster in-front of the HCAL cluster, then the $E_T$ of the hadron candidate is the sum of the $E_T$ of both the HCAL and ECAL clusters.

*Photon candidates* are constructed from information combined from the ECAL, SPD and PRS detectors. These are then identified as photons if there are only one or two

*This means the sub-detectors have the same angular projection to the interaction point.

PRS cell hits in front of the ECAL cluster and no hit in the SPD cells corresponding to the PRS cells. For an inner zone candidate, an ECAL cluster with 3 or 4 PRS cell hits associated to it can also be accepted as a photon. The total $E_T$ of the candidate is just the $E_T$ of the ECAL cluster.

*Electron candidates* are formed the same way as a photon candidate, except with the additional requirement of at least one SPD hit in-front of the PRS cells.

The $E_T$ of the candidates are compared to a fixed threshold, and events containing at least one candidate passing the requirement is retained by the L0 trigger.

### L0 Muon Trigger

The L0 muon trigger searches for hits defining a straight line through the five different stations pointing towards the interaction point [141]. For each hit in M3, the straight line passing through both the hit and the interaction point is extrapolated to M2, M4 and M5. A FOI is calculated in each station, and when at least one hit is found inside the FOI, a muon track is flagged and the pad hit in M2 closest to the extrapolation point is selected for subsequent use. This extrapolation is then extended to M1, where M1 and M2 are subsequently used to calculate the $p_T$ of the track. This is illustrated in Figure 5.8.

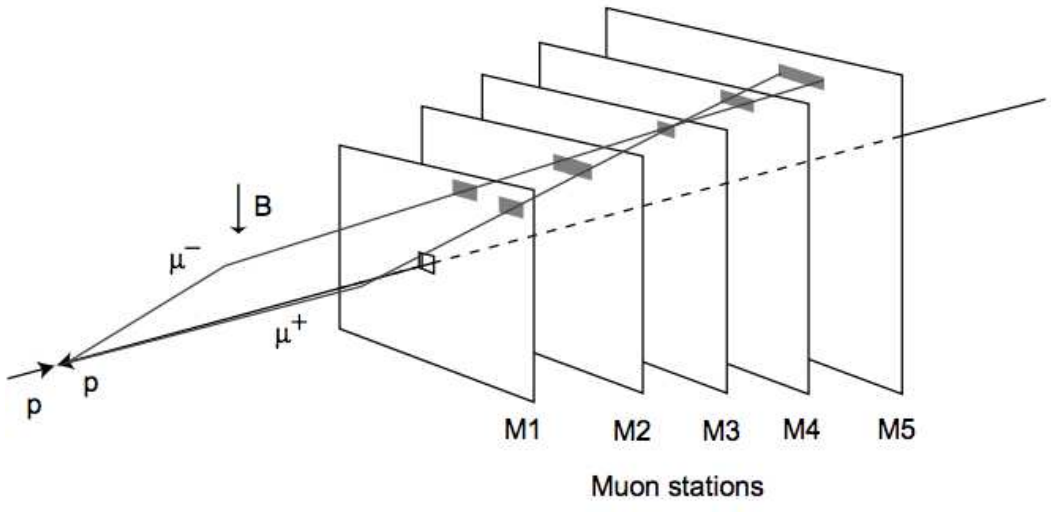


**Figure 5.8:** An example of the track finding algorithm used in the L0 muon trigger. In this particular example, a $\mu^+\mu^-$ event crosses in the same pad in M3. The grey areas highlight the field of interest used to search the other muon stations. Reproduced from [141].

A momentum estimate is calculated on the assumption that the particle originated from the interaction point. The $p$-kick method is based on the idea that the effect of the particle traversing the magnetic field can be considered as a single kick of the momentum vector in the centre of the magnetic field region. The generalised form is:

$$\Delta\vec{p} = q \int d\vec{l} \times \vec{B} \tag{5.1}$$

The variable with the highest sensitivity is the change of momentum in the bending plane, $\Delta p_x$, has the relation [126]:

$$\Delta p_x = p_{x,f} - p_{x,i} = p \left( \frac{t_{x,f}}{\sqrt{1 + t_{x,f}^2 + t_{y,f}^2}} - \frac{t_{x,i}}{\sqrt{1 + t_{x,i}^2 + t_{y,i}^2}} \right) = q \int |d\vec{l} \times \vec{B}|_x \tag{5.2}$$

where the variables $t_x$ and $t_y$ are the slopes of the path in $x$ and $y$ co-ordinates, with the subscript $f$ and $i$ referring to whether the quantity is evaluated before or after the kick at the magnet centre. The magnetic field is given by $\vec{B}$, and the charge and path of the track are given by the quantities $q$ and $d\vec{l}$ respectively.

An estimate of the initial track slopes, and the magnetic field, allows the track momentum to be calculated. This method has an approximate momentum resolution of $\delta_p/p = (0.696 \pm 0.005)\%$. The L0 muon trigger looks for as many as two high $P_T$ muon tracks in an event, or the highest two where more than two are present, and these enter the trigger decision, where different triggers can either select or reject the event. The $p$-kick mechanism is illustrated in Figure 5.9.

### L0 Pile-Up Trigger

The pile-up trigger is designed to search for events with a large number of interactions. It operates by using the Pile-Up system, which consists of two VELO R sensors (labelled A and B) perpendicular to the beam axis, and are located in the -$z$ direction from the interaction point [142]. The following relation is used to determine the $z$ position of the originating vertex for a single track [143]:

$$\frac{R_B}{R_A} = \frac{Z_B - Z_{PV}}{Z_A - Z_{PV}} = k \tag{5.3}$$

where the quantities $Z_B$ and $Z_A$ are the detector positions and thus well known, the quantity $Z_{PV}$ is the (unknown) position of the track origin in $z$, and $R_B$ and $R_A$ are

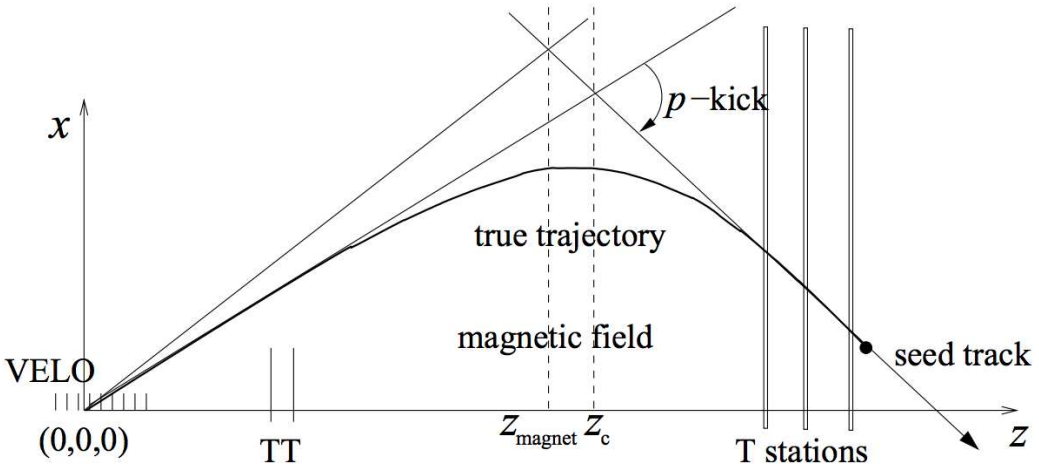


**Figure 5.9:** An illustration of the 'p-kick' technique used in estimating the momentum of the track for the muon trigger. Reproduced from [126].

the radial positions of the track hits. Peaks in the $Z_{PV}$ distribution are indicative of primary vertices, and so events containing multiple peaks can be identified as those with more than one interaction in the event. The pile-up trigger is capable of rejecting these events and selecting events with single primary vertices by identifying these secondary peaks in the $Z_{PV}$ distribution[†].

### L0 Decision Unit

The information gathered from the triggers are then processed at the hardware level by a purpose-built decision unit. Events passing any of the momentum thresholds and criteria in the decision unit are passed to the Readout Supervisor at 40 MHz which makes the final decision on whether an event should be stored or rejected [144]. Trigger lines include, but are not limited to, whether an event has a single muon with a $P_T$ threshold, two muons with different $P_T$ thresholds, and whether a high $E_T$ hadron candidate is present in the event or not. There are also thresholds on the event activity to stop events with too much activity, and thus requiring large processing times, from getting through. This is done through, in most cases, an upper limit on the number of hits in the SPD detector.

[†]Whilst the intention of this system was to reject events with more than one interaction per event, it is not necessarily employed in this manner as the experiment now runs with a higher instantaneous luminosity for the benefits of increased data gathering.

### 5.2.2 Higher Level Trigger

The Higher Level Trigger (HLT) is the two-component (HLT1 and HLT2) final stage of the triggering system. It is a software trigger which analyses the events passing the L0 decision units. The HLT has access to all the data in a particular event, and is designed to reduce the readout rate from 1 MHz to a few kHz. Given this large reduction factor, the HLT is designed to reject events efficiently whilst utilising as little data as possible to decrease the processing times, and is contained in a farm of approximately 2000 CPU cores [138].

#### HLT1

HLT1 uses an *alley* system, which correspond to the different types of trigger present in the L0 system. Where the L0 system has, for example, a high $P_T$ muon, HLT1 uses a $\mu$-alley. This is illustrated in Figure 5.10. Its primary purpose is to use extra input information from sub-detectors not utilised in the L0 decision making process and to confirm the L0 decision. One example of this is the L0+VELO information. This is using the VELO seeding process described previously to create long tracks and then a 3-dimensional $\chi^2$ value is calculated between the reconstructed track and the triggered L0 object. Events are output from HLT1 at a rate of a few tens of kHz.

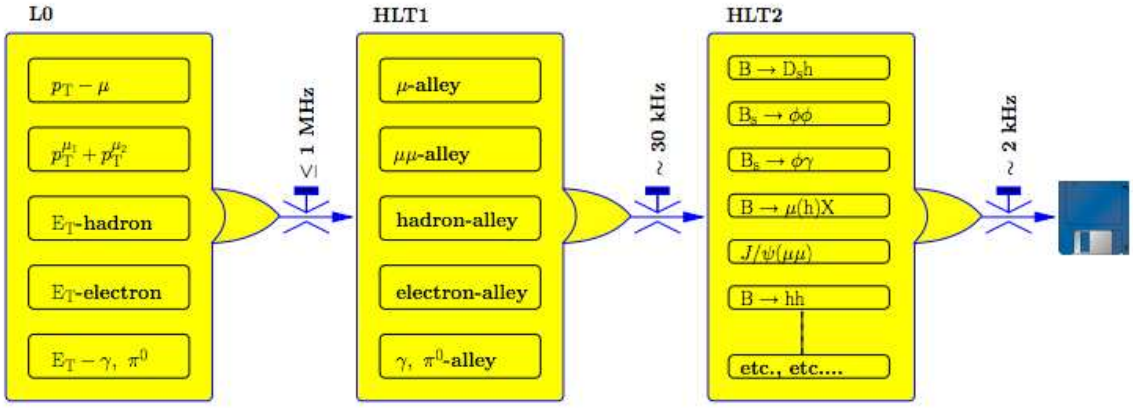


**Figure 5.10:** A schematic diagram of the LHCb trigger system, going from the five L0 decision units to the five HLT1 alleys to the full range of HLT2 lines. Reproduced from [145].

#### HLT2

The HLT2 stage of the trigger fully reconstructs all events it receives. Events at the HLT2 stage are subsequently divided into different physics process, or *stripping*, lines. This means that different thresholds and lines are set for individual physics processes, and this is designed to reduce the rate to $\sim$ 2 kHz, with events passing the selection written to storage for later offline analysis. One example of relevance to the physics analysis presented later in this thesis is a high transverse momentum line, known as the *SingleHighPTMuon* line, which utilises the L0 Muon trigger (*L0MuonDecision*), the HLT1 and HLT2 muon decision lines (*Hlt1MuonDecision* and *Hlt2MuonDecision* respectively).

## 5.3 Software

LHCb software [146] is built upon the Gaudi [147] framework. It contains a number of subset software applications (*Gauss*, *Boole*, *Moore*, *Brunel* and *DaVinci* as shown in Figure 5.11) which are specialised for different tasks, with the aim of taking raw data produced from the experiment to an output format, as well as the simulation of data.

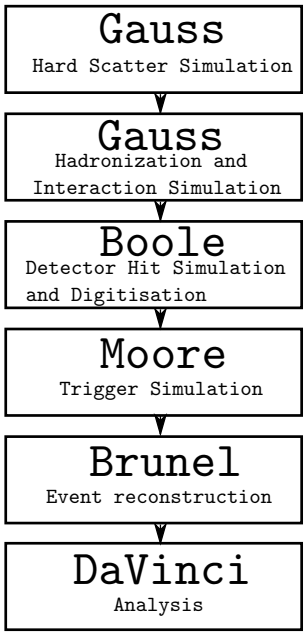


**Figure 5.11:** A schematic diagram of the flow of packages in the LHCb software framework.

### 5.3.1 Simulation

It is essential in a particle physics experiment to understand the underlying processes that may be occurring, and the detector's response to these processes.

At LHCb the simulation of physics processes, and its interactions with the detector, is performed by the Gauss application. Gauss can either use an external Monte Carlo generator, or read in Les Houches Event format files[148], and simulate the hadronisation and subsequent decay, of the physics processes generated. After the simulation of the hard process, GEANT4 [149] is used to propagate the particles through the detector. This stage also reads in a virtual representation of the LHCb detector, and simulates effects such as multiple scattering, conversions in material, and the decay of longer-lived particles through the volume of the detector.

The application Boole then emulates the electronics deployed in the experiment to convert the interactions produced by Gauss to create readout data in a format identical from the actual experiment. Moore is utilised after Boole to simulate trigger requirements on the events produced.

### 5.3.2 Reconstruction

The offline full event reconstruction process is performed in the Brunel application. It uses the output from either the Boole application, or the detector, as input. It creates tracks and vertices in the event as well as creating objects known as *proto-particles*. These proto-particles are particles with no definitive assigned PID, but instead store information from the calorimeters, muon chambers and RICH. This information is then used at a later stage to produce particle candidates. After the Brunel process is finished, it stores its output in the format of a *data summary tape* (DST), for offline analysis.

### 5.3.3 Analysis

Offline analysis is performed by using a software package known as DaVinci, and then user made algorithms written typically utilising an analysis package such as ROOT [150]. It reads events from the DSTs produced by Brunel, and imposes user-specified particle combination and selection requirements. For events that pass the user-specified requirements, it then writes out information that has been specified by the user, such as the

momentum of the final state particles, or its impact parameter, into a ROOT file, known as an *nTuple*, which is analogous to a database. Users can then place the additional requirements on top of the selections made in DaVinci. The results can then be formatted into graphical representations of the data.

## 5.4 Event Variables and Jet Construction

In the search for rare processes, often there are many SM backgrounds that can provide similar or identical final states. One example would be a $H \rightarrow \tau\tau$ search, for which $Z \rightarrow \tau\tau$ is a background that is much larger than the signal. In order to eliminate or reduce the contributions of backgrounds, parameters are constructed for events and/or the particles in them to provide discrimination between signal and background. Event-wide variables are quantities such as *missing transverse energy* or MET, a quantity used in many of the GPDs' searches for top quarks in leptonic channels.

This section will first describe some of the potentially useful discriminating variables between signal and background, before moving on to describe the jet reconstruction and identification procedure.

### 5.4.1 Candidates and Primary Vertex

In the presence of more than one PV, for example in a $Z \rightarrow \mu\mu$ analysis, it is important to ensure that both the $\mu$ leptons originate from the same vertex. Other processes, which produce particles that are long lived, may not impose such a requirement - such as reconstructing long-lived particles. It is also useful to impose a candidate requirement. For example in a $Z \rightarrow \mu\mu$ event, it would be possible for the event to be mis-identified as two $W \rightarrow \mu\nu$ events.

### 5.4.2 Transverse Momentum

The transverse momentum of a particle is given by:

$$P_T = \sqrt{P_x^2 + P_y^2}. \tag{5.4}$$

Leptonic decays from a $W^{\pm}$ boson, for example, are expected to have high transverse momentum due to the high mass of the boson. This is in contrast to QCD events where a lepton from a $b$-hadron decay would typically have a much lower transverse momentum. This is because the threshold energy for $b\bar{b}$ production is $2 \times m_b$, whereas the threshold energy for $W$ production is $m_W$. Transverse momentum is a useful discriminator for eliminating many backgrounds.

### 5.4.3 Invariant Mass

For a two body decay of $X \rightarrow YZ$, the invariant mass of $X$ is the magnitude of the sum of the momentum four-vectors of $Y$ and $Z$. The magnitude of a four-vector is (assuming *c=1*):

$$m = \sqrt{E^2 - (P_x^2 + P_y^2 + P_z^2)}. \tag{5.5}$$

For certain processes, such as $Z \rightarrow \mu\mu$, the invariant mass of the two final state muons is a meaningful quantity as it reconstructs the original mass of the $Z$ boson. For processes such as $Z \rightarrow \tau\tau \rightarrow \mu e \nu_\mu \nu_e \nu_\tau \overline{\nu_\tau}$, the invariant mass of the $\mu$,e leptons will be correlated with the original parent's invariant mass, but be smeared by not reconstructing the missing neutrino(s).

### 5.4.4 Isolation

Processes such as a $W \rightarrow \mu\nu$ decay should produce an isolated lepton. Other processes such as the semileptonic decay of a $b$-hadron, have final states that may include much more activity. To increase the purity in selecting decays of a $W$ boson, for example, an isolation quantity can be useful. This quantity is defined as:

$$I_l = \frac{E_l}{E_l + \sum_{i=0}^{i=n} E_i} \tag{5.6}$$

where the index $i$ refers to all tracks within a cone of $\Delta R < 0.5$ of the lepton ($\Delta R$ is defined as $\Delta R = \sqrt{(\Delta\ \phi)^2 + (\Delta\ \eta)^2}$).

### 5.4.5 Impact Parameter

A property of a massive particle like the $W$ boson is that it has a very short life-time. This short life-time has the effect of causing decays of the bosons to occur at the primary vertex at which the boson was created. This characteristic can be exploited in the search for *primary vertex* leptons - leptons that can be tracked back to the origin. Due to effects arising from the detector's intrinsic resolution, it is impossible to extrapolate these tracks back to the primary vertex without any uncertainty. Due to this, selecting for primary vertex leptons generally requires a maximum IP value (typically of the order of tens of microns). The distance of closest approach of the lepton's extrapolated track to the closest primary vertex on that track is called the impact parameter (IP). Particles which are long lived - for example $\tau$ leptons, or $b$-mesons, will typically travel $\sim$ 1 cm before decaying[97], thus calculating the impact parameter for leptons arising from these decays will yield high IP values.

The impact parameter is calculated in an unbiased method - the candidate track is removed from the vertex reconstruction, and the vertex is re-fitted and the impact parameter is calculated based on this refitted vertex. A diagram representing the impact parameter calculation is presented in Figure 5.12, with the line noted $d$ representing the impact parameter.

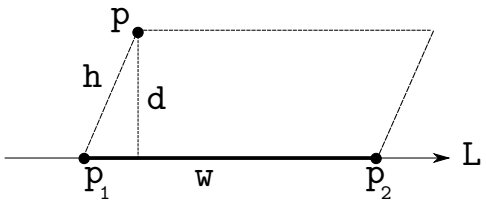


**Figure 5.12:** A diagram illustrating the impact parameter calculation for the closest approach between a line (L) and a point (P). The cross product between the line and the vector of $P_2$-$P_1$ is taken, and the formula for the area of a parallelogram is used to calculate the quantity $d$.

The mathematical calculation to perform this is

$$\mathbf{w} = \mathbf{P_2} - \mathbf{P_1} \tag{5.7}$$

$$|\mathbf{h} \times \mathbf{w}| = A \tag{5.8}$$

where $A$ is the area of the parallelogram formed by the thinner lines. The area of a parallelogram can also be related to its height and its width by

$$A = \mathbf{d} \cdot \mathbf{w} \tag{5.9}$$

thus it is possible to combine the two equations to give

$$d = \frac{|\mathbf{h} \times \mathbf{w}|}{|\mathbf{w}|}. \tag{5.10}$$

### 5.4.6 Impact Parameter Closest Approach

The impact parameter closest approach is a measure of the impact parameters between two particles, and the $\Delta\phi$ that separates their momenta. This is a useful variable as $Z$ boson decays, in the $Z$ rest frame, creates lepton pairs at 180°, whereas in the $t\bar{t}$ rest frame, the $WW$ bosons do not necessarily have the same angular correlation, when considering the lepton decay products. This value is diluted slightly by the intermediate stage of $\tau$ leptons from the Z boson, which can not be fully reconstructed due to the loss of the neutrino information. This provides an additional angular "kick" to the leptons, which smears the $\phi$ distribution. The formula used to calculate this is:

$$IPCA^2 = IP_1^2 + IP_2^2 - 2 \times IP_1 \times IP_2 \times \cos(\Delta\phi) \tag{5.11}$$

where $\Delta\phi = \phi_1 - \phi_2$. A diagram of the IPCA calculation is presented in Figure 5.13 for $\Delta\phi \approx 180°$, and for a $t\bar{t}$ event with a significantly lower $\Delta\phi$ value. Cases in which cos $(\Delta\phi) \sim -1$ reduce to

$$IPCA^2 = IP_1^2 + IP_2^2 + 2 \times IP_1 \times IP_2 \tag{5.12}$$

and cases where cos $(\Delta\phi) \sim 0$, the formula reduces to a simple Pythagorean

$$IPCA^2 = IP_1^2 + IP_2^2. \tag{5.13}$$

By requiring the same magnitude on the IPCA as the individual IPs, it is possible to eliminate the cases of cos $(\Delta\phi) \sim -1$ substantially.

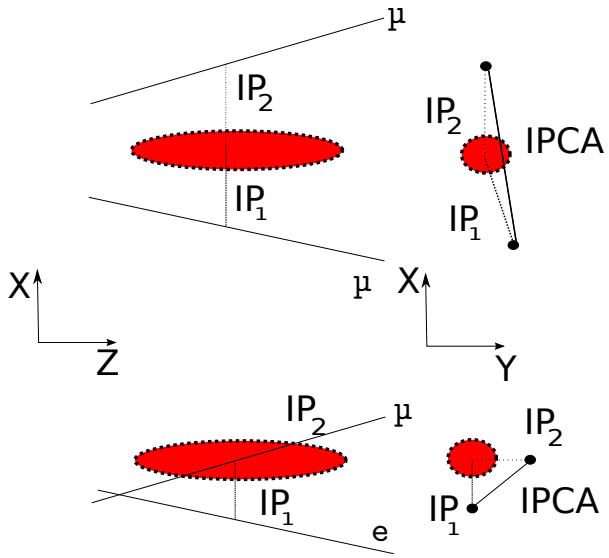


**Figure 5.13:** An illustration of the impact parameter closest approach variable. Top: Example of a $Z \rightarrow \mu\mu$ event where the leptons are separated by $\sim 180°$. Bottom: an example of an event where two leptons originate from $W$ boson decays, and thus are not necessarily correlated in angular distribution.

### 5.4.7 Jet Reconstruction

Jets are a shower of particles that are created during the hadronisation of hard scattering final state partons, for example in the specific case of $t\bar{t}$, both $b$-quarks. More information on the jet hadronisation process can be found in [151]. This section will describe the techniques employed at LHCb to identify jets [152].

The LHCb technique utilises a two-stage process. The first step is to construct a particle flow, from charged particle tracks and calorimeter clusters. This particle flow produces a list of four vectors in the event, with discrimination for $\pi$, $K$, $p$, $e$ and $\mu$ charged particles as well as neutral clusters. The list of four vectors is then fed into the jet clustering algorithm. The jet clustering is performed using the anti-k$_t$ algorithm [153], with an $R$ parameter of 0.5 where $R = \sqrt{\Delta\phi^2 + \Delta\eta^2}$. To optimise the computing time, the FastJet implementation of anti-k$_t$ is used [154, 155]. A further imposition is made that jets have a minimum $P_T > 5$ GeV/c. Anti-k$_t$ is a theoretically favoured jet clustering algorithm over traditional pairing algorithms such as the Cambridge/Aachen [156] or the k$_t$ algorithm [157]. More information can be found on the comparisons of the anti-k$_t$ algorithm to other jet clustering algorithms in [153].

### 5.4.8 *b*-tagging

The identity of a jet is often labelled by its original parton. For example, a $b$-jet is one that originated from the hadronisation of a $b$-quark. This section will describe the method of $b$-tagging utilised specific to the analysis presented later in Chapter 6.

In the identification of a $b$-jet, many variables may contribute to discrimination between signal and background. For example, it can be anticipated that a track originating from a $b$-hadron would typically have a large impact parameter, and transverse momentum. These variables can be correlated, which means that sequential requirements can be inefficient. Therefore a multi-variate approach is utilised to optimise the discrimination.

A neural network method is employed for the decision process in the $b$-tagging. The specific neural network implementation used here is NeuroBayes [158, 159]. The network trained for $b$-tagging in LHCb cascades one network, the track-network, which is used to discriminate the probability of whether or not a track originated from a $b$-hadron, into a second network, the jet-network, which aggregates the information for every particle as well as some jet variables to make a decision. The output of this network is a classification parameter, which ranges from -1 to +1. Events at or near +1 are most likely to be signal events, whilst events at -1 are most likely to be background events [160].

The requirement imposed upon the final jet network output is that the value must be $\geq 0.90$. This corresponds to an efficiency for correctly identifying $b$-jets of $\epsilon_b \approx 60\%$ and a light flavour acceptance of $\approx 1\%$. These quantities are independently evaluated in Section A.3.7. An example plot of the output of the $b$-tagger is illustrated in Figure 5.14. The efficiency versus purity for the $b$-tagger is illustrated in Figure 5.15.

### 5.4.9 Summary

The powerful discriminating variables which have been identified as useful for the top analysis presented in Chapter 6 have been described. Imposing requirements on these variables can significantly enhance the purity of a sample used for an analysis. The method of constructing jets at LHCb has also been described, as well as the framework of the $b$-tagging used in this particular analysis.

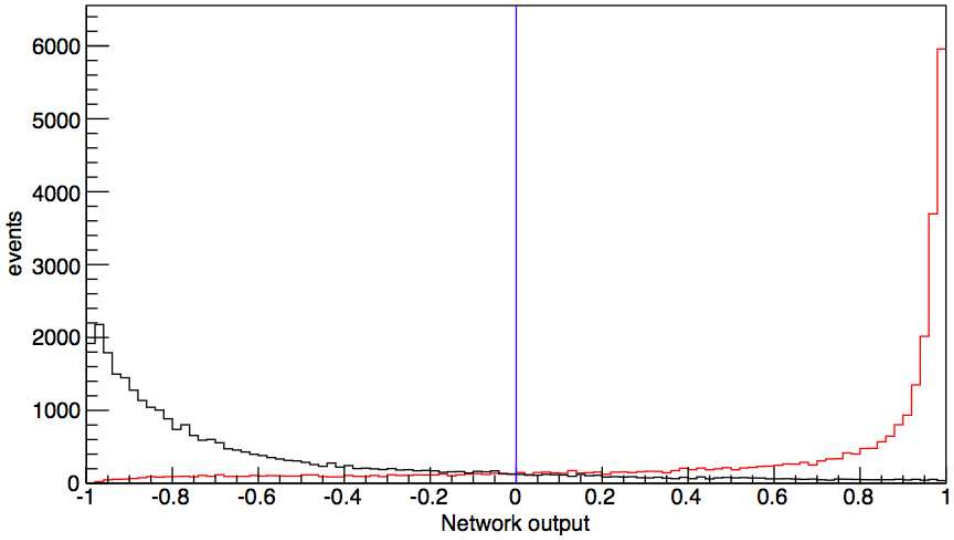


**Figure 5.14:** An evaluation of the jet network $b$-tagger performed on $b\bar{b}$ Monte Carlo and minimum bias data. The red line corresponds to events from the $b\bar{b}$ sample and the black line corresponds to the minimum bias data. Good separation between the signal and background is found. Reproduced from [160].

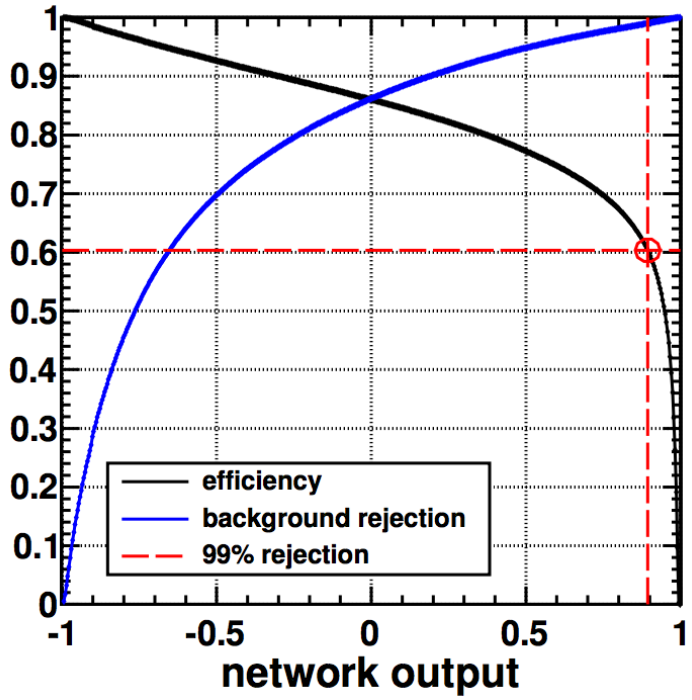


**Figure 5.15:** The evaluated efficiency versus purity of the $b$-tagger for $b\bar{b}$ Monte Carlo against minimum bias data. Reproduced from [160].

# Chapter 6

# Top Pair Production

## 6.1 Motivation

A forward region ($\eta > 2$) $t\bar{t}$ cross-section measurement has yet to be performed at the LHC. Such a measurement would be an essential foundation towards the goal of measuring the asymmetry, which may have potential signs of BSM physics. The analysis presented here is performed on the $\sqrt{s}$=8 TeV, $\mathcal{L}$=2.01 fb$^{-1}$ 2012 LHCb data sample, using a dilepton+$b$-jet signal*. The decay mode employed in this search is: $t\bar{t} \rightarrow b\,W^+\,\bar{b}\,W^-$ with the additional requirement that $W^+\,W^- \rightarrow \mu^\pm\,e^\mp\,\nu_e\,\nu_\mu$ and is illustrated in Figure 6.1. This signal is chosen as it removes background contributions from events such as $Z \rightarrow \mu\mu$ +$b$-jet.

A cross-section measurement can also set limits on other processes, such as: the decay of a heavy Higgs ($H \rightarrow t\bar{t}$), for which the branching ratio as a function of $M_H$ is shown in Figure 6.2, or the decay of $t \rightarrow bH^+$, where a light charged Higgs boson replaces the $W^+$ boson in the decay of a top quark [161], as is illustrated in Figure 6.3.

A typical $t\bar{t}$ event simulated in Monte Carlo is shown in Figure 6.4. The signal characteristic is a muon with high transverse momentum, and an electron with a large $E_T$ ECAL cluster, as well as a $b$-jet.

*The 7 TeV data sample of 1 fb$^{-1}$ is neglected because of the significantly lower size of the data sample and the lower cross-section of the $t\bar{t}$ production process.

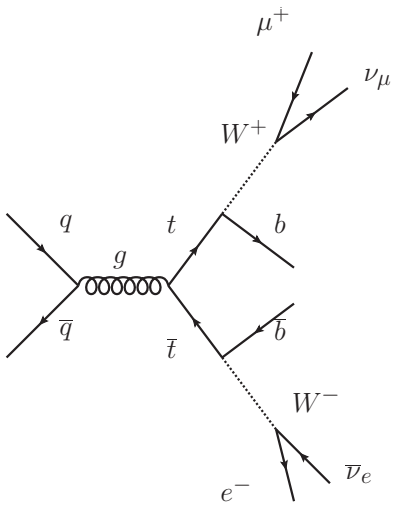


**Figure 6.1:** The tree level Feynman diagram of the full decay of $t\bar{t}$ pairs into the specific channels used for this analysis.

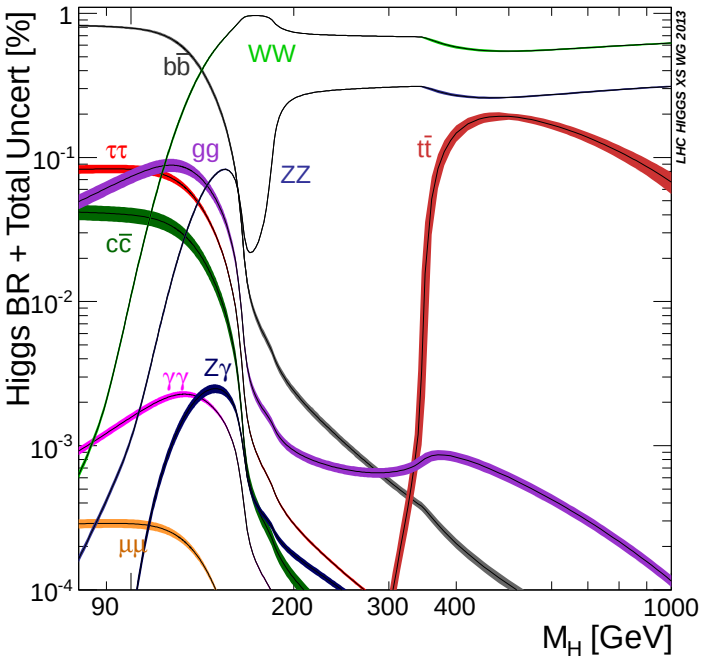


**Figure 6.2:** Branching ratio of the Higgs Boson as a function of $M_H$. For higher mass Higgs Bosons, $H \rightarrow t\bar{t}$ is the third most dominant channel. Reproduced from [162].

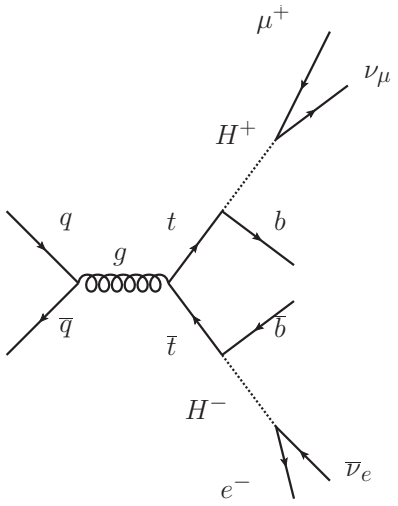


**Figure 6.3:** An example of a top quark pair both decaying through a Light Higgs mechanism into the channel used for this analysis.

## 6.2 Fiducial Cross-section

In this analysis the cross-section for $t\bar{t}$ production will be presented in terms of a *fiducial cross-section* $\sigma_{\text{fid}}$. The fiducial cross-section is the cross-section into the acceptance of LHCb subject to specific lepton and jet requirements, rather than the full inclusive cross-section. In a forward arm spectrometer, this helps to remove uncertainties arising from extrapolation of samples to the full solid angle production cross-sections. For this measurement, we define $\sigma_{\text{fid}}$ to be the cross-section for the production of $t\bar{t}$ pairs where both the leptons have a transverse momentum of at least 15 GeV/c and $2 < \eta < 4.5$, and a generator level $b$-quark of at least $P_T > 5$ GeV/c with $2.0 < \eta < 4.5$.

The fiducial cross-section is calculated using a Next-to-Leading-Order (NLO) Monte Carlo generator, POWHEG-BOX [163], with different input PDF sets. The PDF sets used in this study are MSTW [164], NNPDF [165] and CT10 [166]. The NNPDF set incorporates the latest results from HERA-1 [167], and the CT10 and NNPDF sets use a central value of $\alpha_s(M_Z)$, where MSTW fits $\alpha_s(M_Z)$ to the PDF parameters and uses the best fit value. More information on the PDFs recommended for the LHC can be found in [168]. The results for the fiducial cross-section is documented in Table 6.1.

The statistical uncertainties of the three samples are combined to provide the statistical uncertainty on the fiducial cross-section, and the deviation from the average fiducial cross-section to the most outlying one will later be taken as the systematic

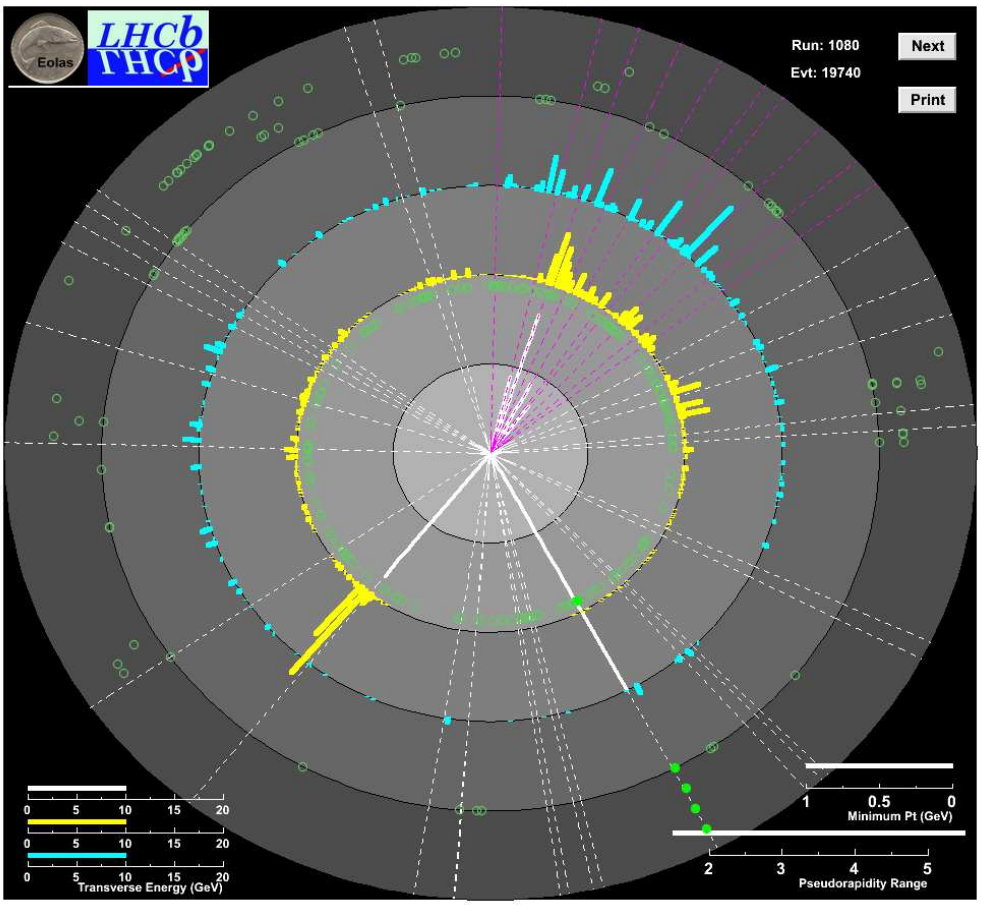


**Figure 6.4:** An event display of a simulated $t\bar{t}$ event. Increasing radius on the display corresponds to the $z$-axis in the experiment, the outermost ring represents the muon chambers, and $\phi$ represents $\phi$. The solid white bars are graphical representations of the transverse momentum of specific tracks, the yellow blocks represent ECAL clusters, and the blue blocks represent HCAL clusters. Muon chamber hits are represented by green circles, which are coloured solid if associated to a track. Purple tracks are associated to the $b$-jet.

| Generator | PDF | Events Generated | Events Passed | $\mathcal{L}$ (fb$^{-1}$) |
|---|---|---|---|---|
| POWHEG | MSTW2008nlo68cl | 24,000,000 | 1765 | 102.5 |
| POWHEG | NNPDF22 nlo 100 | 24,000,000 | 1512 | 102.5 |
| POWHEG | CT10nlo | 24,000,000 | 2087 | 102.5 |

**Table 6.1:** The three different samples used to calculate the top fiducial cross-section.

uncertainty. The effective luminosity ($\mathcal{L}$), is calculated by normalising to the NNLO calculated cross-section [26]. A theoretical uncertainty is calculated from the uncertainty on the theoretical cross-section used for normalization. This provides a value of

$$\sigma_{\text{fid}}(\sqrt{s} = 8 \text{ TeV}) = 17.5^{+1.2}_{-1.0}(\text{theo.}) \pm 0.2(\text{stat.}) \pm 2.9(\text{PDF})\text{fb}$$

where the first uncertainty refers to the theoretical uncertainty on the cross-section, the second uncertainty refers to the statistical uncertainties of the samples used, and the third uncertainty refers to the PDF uncertainties, which is calculated by taking the most outlying PDF value and subtracting it from the average.

The calculated fiducial cross-section can then be used with other generators to create further normalised samples. If $N$ events are generated by a Monte Carlo generator that pass the requirements, then the effective luminosity is:

$$\mathcal{L}_{\text{eff}} = \frac{N}{\sigma_{\text{fid}}}. \tag{6.1}$$

This allows for significantly higher statistics samples from different generators to be studied in depth whilst removing uncertainties which exist in an exclusively leading order (LO) generator. The uncertainty on this method is taken as the systematic uncertainty on the overall fiducial cross-section.

## 6.3 Simulation of Signal and Background Processes

### 6.3.1 Top Pair

Monte Carlo samples for top pair production were produced using PYTHIA 8.1 [169] (which is a LO generator) and then normalised by the NLO fiducial cross-section calculated using POWHEG-BOX to determine effective luminosities. The samples in use

for this analysis have the requirement that $\eta_{\mu,e} > 1.8$. This corresponds to a loosened acceptance for LHCb, which is later tightened at the detector reconstruction level. Requirements are not imposed on any $b$-jet activity at the generation level due to the channel of $\mu, e, b$ being a subset of the $\mu, e$ sample.

### 6.3.2 *Z* Boson Background

The primary background is the decay of a $Z$ boson to $\tau$ lepton pairs ($Z \to \tau^+\tau^-$) and the subsequent decay of the $\tau$ particles to a muon and an electron pair. The cross-section for $Z$ boson production at $\sqrt{s} = 8$ TeV is well measured at the LHC [170]:

$$\sigma(pp \to ZX) \times BR(Z \to l^+l^-) = 1.12 \pm 0.01(\text{stat.}) \pm 0.02(\text{syst.}) \pm 0.05(\text{lum.})\text{nb}$$

and is $\sim 5$ times larger than the overall expected $t\bar{t}$ cross-section at the same centre of mass energy. The LO diagram for $Z$ boson production is shown in Figure 6.5.

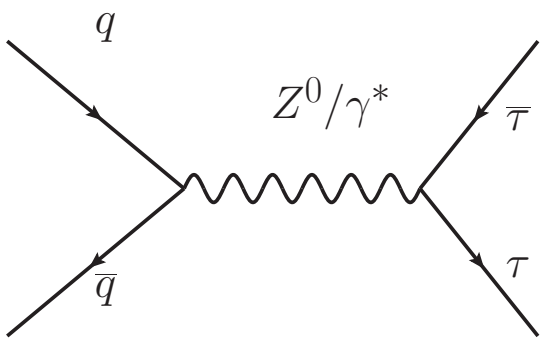


**Figure 6.5:** The LO $q\overline{q}$ Feynman diagram producing a $Z$ boson, decaying to two $\tau$ leptons.

The $\mu e$ channel significantly reduces the background for a top quark search from $Z$ bosons compared to using a $\mu\mu$ or $ee$ channel as the branching ratio requirement of $Z \to \tau\tau \to \mu e$ provides only a 2% [1] contribution compared to $Z \to \mu\mu$ or $Z \to ee$, which do not have additional neutrinos. An additional suppression of the $\tau$ decay modes can be made by exploiting a property of the $\tau$ lepton, namely that typically it decays within a few millimetres of the primary vertex as the $\tau$ lifetime is $2.9 \times 10^{-13}$ s. This characteristic allows for strong discrimination against signal by requiring that lepton tracks do not originate from secondary vertices.

Three Monte Carlo samples generated in PYTHIA (which uses the CTEQ5L PDF) are used for the $Z \to ll$ simulations, where the three samples correspond to $l = e, \mu, \tau$.

Four million $Z \to \tau\tau$ events are simulated, corresponding to an effective luminosity of $\sim 15$ fb$^{-1}$. Two samples of 500,000 events for $Z \to ee$ and $Z \to \mu\mu$ events are generated, corresponding to an effective luminosity of $\sim 2.5$ fb$^{-1}$, where the events require at least one lepton inside the LHCb acceptance.

### 6.3.3 *WW* Background

Diboson production is another significant background for top quark pair production. Both processes use the common decay channel of $WW \to \mu e$, thus it is kinematically and topologically very similar to the signal. The total cross-section for $WW$ production at $\sqrt{s} = 8$ TeV is predicted in MCFM to be $\sigma = 57.3^{+2.4}_{-1.6}$ pb which is consistent with CMS results [171, 172]. A diagram for the production of $WW$ dibosons is shown in Figure 6.6. The requirement of a $b$-jet provides a strong discriminator in the reduction of background contributions from $WW$ diboson production.

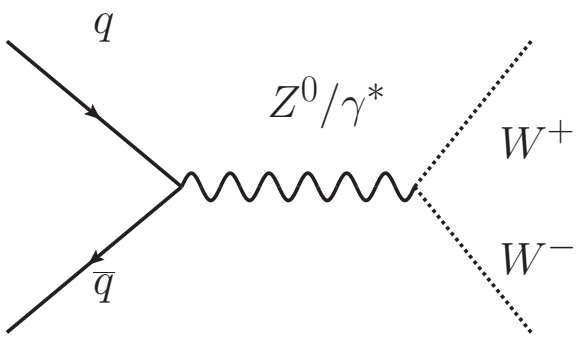


**Figure 6.6:** A LO Feynman diagram producing $WW$. Associated $b$-jets are rare because they can only be formed from an NLO production mechanism or falsely identified from the underlying event.

This background is evaluated using the same method as the evaluation for the $t\bar{t}$ signal sample described in Section 6.2. A fiducial cross-section is calculated in POWHEG-BOX [173] to be $\sigma_{\text{fid}} = 52.5 \pm 1.4$ (PDF) $\pm$ 0.2 (stat.) $\pm$ 2.2 (theo.) fb, without the additional $b$-quark requirement used for the top pair fiducial cross-section. A total of 200,000 $WW$ events are simulated, corresponding to 1762 fb$^{-1}$ of data.

### 6.3.4 *ZW* Background

The $ZW$ diboson contribution is rarer ($\sim 33\%$) than $WW$ bosons, but is also considered. To create $\mu, e$ candidates from $ZW$ events, the $Z$ boson is required to decay

to either $\mu\mu$ or $ee$ and the W boson required to decay to $e$ or $\mu$ respectively. The cross-section for $ZW$ production at $\sqrt{s} = 8$ TeV is experimentally measured to be $\sigma = 20.3^{+0.8}_{-0.7}(\text{stat.})^{+1.2}_{-1.1}(\text{syst.})^{+0.7}_{-0.6}(\text{lum.})$ pb by ATLAS [174], which is in agreement with the MCFM prediction [175]. An example LO production diagram for $ZW$ bosons is shown in Figure 6.7.

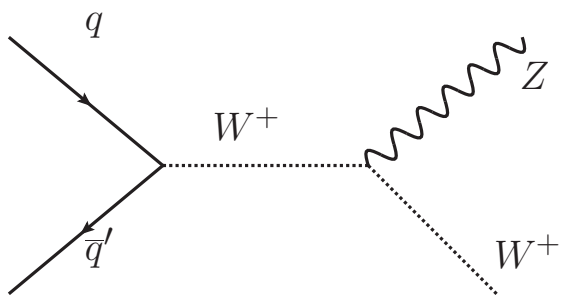


**Figure 6.7:** Quark anti-quark annihilation producing a $ZW$ boson pair.

The contribution of $ZW$ events to the signal region is expected to be symmetric between same sign (SS) and opposite sign (OS) channels, which is documented further in Section 6.6. A data driven method of estimating the $ZW$ contribution to the top signal is used and is based on the symmetry of SS (background-like) to OS (signal-like) events. The fiducial cross-section is estimated to be 3.2 fb, which after reconstruction efficiencies means the expectation of $ZW$ events in LHCb is negligible.

### 6.3.5 QCD Background

Due to the large number of processes that can contribute to the QCD background, a data driven method, rather than a Monte Carlo analysis, is used to calculate the contribution. As with the $ZW$ events the same sign channel, i.e. $\mu^{\pm}e^{\pm}$ is used for this purpose, as documented in Section 6.6. From generator level $b\bar{b}$ events, the rate of production of two leptons is estimated to be $20 \pm 1$ per fb$^{-1}$ with only the transverse momentum, isolation, and impact parameter requirements imposed, which are discussed further in Section 6.5. Upon imposition of the efficiencies obtained from the same sign channels i.e. the invariant mass efficiency, the $b$-tagging efficiency and the impact parameter closest approach efficiency, and the overall analysis reconstruction efficiency, this contribution is estimated to be $< 2$ events per fb$^{-1}$.

To check the consistency of the Monte Carlo hypothesis with the data, the electron and muon anti-isolation efficiencies are tested in both samples. The result is obtained

that, from Monte Carlo, 65 of 318 electrons are $< 40\%$ isolated, and 2080 from 22846 muons. This gives efficiencies of $20.4 \pm 2.5\%$ and $9.1 \pm 2.0\%$ respectively. In data, these efficiencies are calculated to be $18.4 \pm 7.0\%$ and $6.6 \pm 1.1\%$ respectively, which is consistent with the Monte Carlo hypothesis. This demonstrates the QCD events dominate in the same sign channel.

### 6.3.6 Higgs Background

Other contributory processes such as Higgs Boson productions are neglected by considering the cross-section alone [176]. The expectation of Higgs at $\sqrt{s}$=7 TeV in LHCb is $< 0.2$ events per fb$^{-1}$, which constitutes <5% of the $t\bar{t}$ signal before the additional requirement of a $b$-jet. This background is therefore neglected.

## 6.4 Event Pre-selection

To purify the datasets from the full $\mu$ trigger stream for 2012 of 500M events, a further stripping is applied to enhance the $t\bar{t}$ signal content. This process reduces the sample selection down to 100,000 events. This requires that the potential tracks of interest, such as the $\mu$ or e, are of high quality and the electron and muon candidates exist in the event. The selections applied in this pre-selection are standard LHCb criteria with well known efficiencies, which are documented in full in Appendix A, and additional requirements: the impact parameter for each lepton is $< 35$ $\mu$m and $P_T(e) >$ 5 GeV/c.

### 6.4.1 Triggering

Data is acquired through the LHCb muon triggers[†], which requires a single $\mu$ in an event with $P_T > 15$ GeV/c. The efficiency of this triggering line is calculated in Section A.3.1.

[†]Specifically *L0MuonDecision*, *Hlt1SingleHighPTMuon* and *Hlt2SingleHighPTMuon*. These triggers also impose a *global event cut*, which is a maximum number of SPD hits. The triggers used in this analysis require events to have <600 SPD hits. More detail on these can be found in Chapter 5.

### 6.4.2 Track Selection

Tracks for muon and electron candidates are selected requiring long-tracks in the fiducial region $2.0 < \eta_{\mu,e} < 4.5$, and a $\chi^2$ probability of obtaining the track fit greater than 0.1% in order to reject poorly reconstructed tracks. Tracks contributing to the $b$-jet process are taken from all tracks in the event, but the final $b$-jet must have a jet axis of $2.0 < \eta < 4.5$. The distribution of track quality in the $t\bar{t}$ Monte Carlo for reconstructed and truth-matched signal tracks is shown in Figure 6.8.

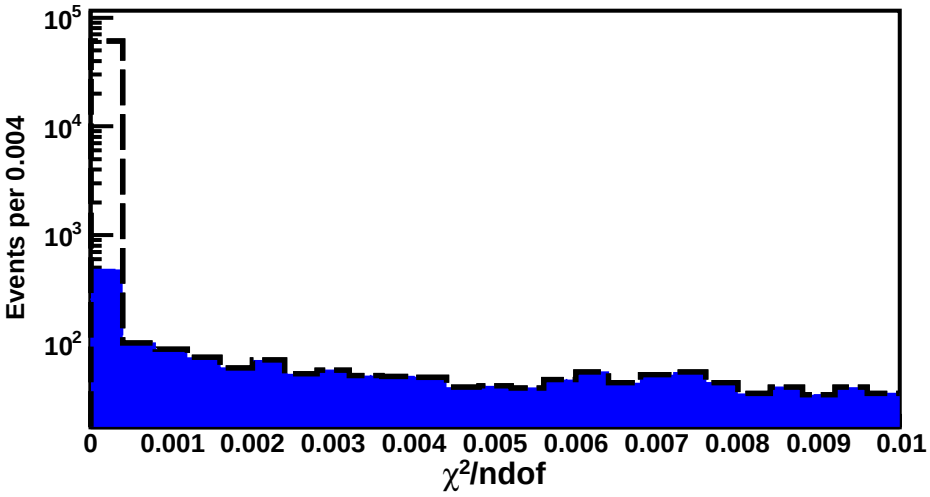


**Figure 6.8:** Track fit $\chi^2/ndof$ for all tracks (black) and tracks which are associated to an MC truth muon (blue) in $t\bar{t}$ Monte Carlo.

### 6.4.3 Muon Identification

Muon identification is done via the standard procedure documented in Chapter 5, requiring Tight Muons rather than the slightly higher efficiency Loose Muons. An additional requirement is imposed, known as $\epsilon^{\mu}_{veto}$, which is designed to remove electrons misidentified as muons. This is performed by requiring that the ECAL energy associated with the track is no more than 10 GeV.

### 6.4.4 Electron Identification

The identification of high energy momentum electrons is more complex than that of muons at LHCb due to saturation of the calorimeter. This analysis will use a custom electron definition for sample selection similar to the one used in the LHCb $Z \rightarrow ee$ cross-section measurement [98]. This custom definition uses a set of criteria imposed upon all tracks in an event, and additionally requires information from the PRS, ECAL and HCAL calorimeters, which are listed below

$$E_{ECAL}/P > 0.1$$
$$E_{HCAL}/P < 0.05$$
$$E_{PRS} > 0.05 \text{ GeV}.$$

In addition to the calorimeteric information, it is also required that the candidate tracks must fail the *Loose Muon* requirement documented in Chapter 5, which ensures they match to less than three hits in the final muon stations.

## 6.5 Top Event Selection From Data

Selection requirements were developed to enhance the purity and background rejection of the chosen channel. The most sensitive variables were found to be: the transverse momentum of the leptons ($P_T$), the invariant mass of the dileptons ($M_{\mu,e}$), the impact parameter of the leptons ($IP_l$), the impact parameter closest approach of the two leptons (IPCA), the isolation of the leptons ($I_l$) and a variable (JetNN) that discriminates for the $b$-content of a jet. Further details of these variables are given in Chapter 5. The impact parameter is discussed further in Section A.1. These are discussed in order of their application:

$P_T(\mu, e)$: A transverse momentum requirement selects events in which each lepton must have at least 15 GeV/c. Transverse momentum requirements assist in the identification of leptons from $t \rightarrow W \rightarrow l$ decays. The comparison of the $P_T$ for the electron from MC samples and data is illustrated in Figure 6.9. The estimated purity after this requirement is $\sim 0.8\%$.

$M_{inv}(\mu, e)$: An invariant mass requirement is imposed on the dileptons. The primary background contribution to the backgrounds of primary vertex $\mu, e$ events are anticipated

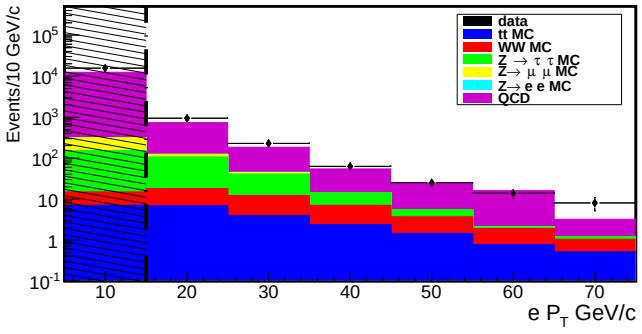


**Figure 6.9:** The $P_T$ spectrum for selected electron candidates after loose requirements are imposed upon the event. The QCD contribution is reduced by a factor of 10 by imposing a requirement that the electron transverse momentum is $> 15$ GeV/c. The shaded area corresponds to a region that is discarded after a selection requirement.

to be random combinations of muons and electrons e.g. particles which have no common source. In the case of the $Z$, $WW$, $ZW$, and $t\bar{t}$ samples, due to the common parent of the dileptons, the mass spectra for the two leptons will be higher than that of the QCD and other combinatoric backgrounds. A requirement on the invariant mass of $>15$ GeV/c$^2$ allows discrimination from these random combinations of dileptons to events in which a heavier resonance is in common for the two leptons. An example of the invariant mass with the loose requirements is illustrated in Figure 6.10. The estimated purity after this requirement is $\sim 1.0\%$.

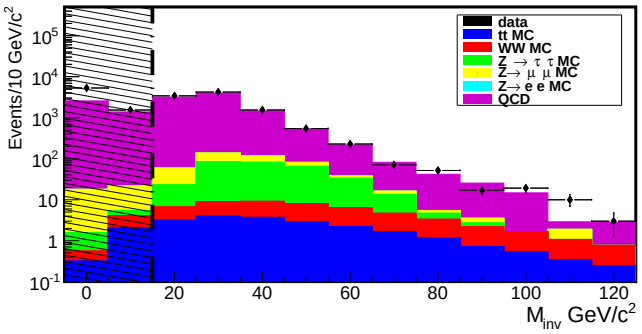


**Figure 6.10:** The invariant mass for the processes considered. The shaded area on the left hand side of the plot corresponds to discarded events.

*IPCA*: An IPCA requirement of $< 35$ $\mu$m suppresses back-to-back leptons, or leptons which originate from the decay of long-lived particles, and helps to suppress $Z \rightarrow \tau\tau$ con-

tributions. This is presented in Figure 6.11. The estimated purity after this requirement is $\sim$1.3%.

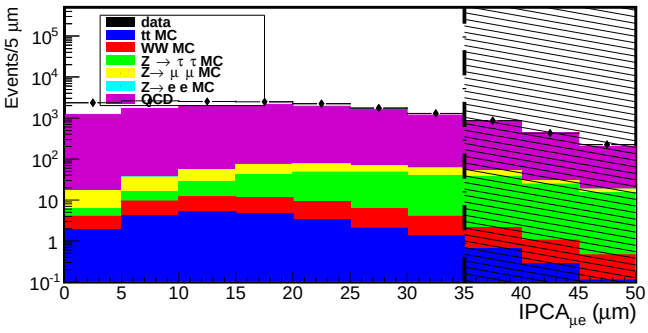


**Figure 6.11:** The impact parameter closest approach distribution for the $\mu e$ system. The QCD and $Z \rightarrow \tau\tau$ distributions can be observed to be flat, whereas the $t\bar{t}$ Monte Carlo peaks around $\sim$10-15 $\mu$m. The shaded area corresponds to high IPCA events which are removed from the sample.

$I_l$: Requiring isolated leptons (of isolation$>$ 0.9) discriminates against leptons originating from jets versus leptons from direct decays such as a $W$ boson. This is illustrated in Figure 6.12 and Figure 6.13. The estimated purity after this requirement is $\sim$5.8%.

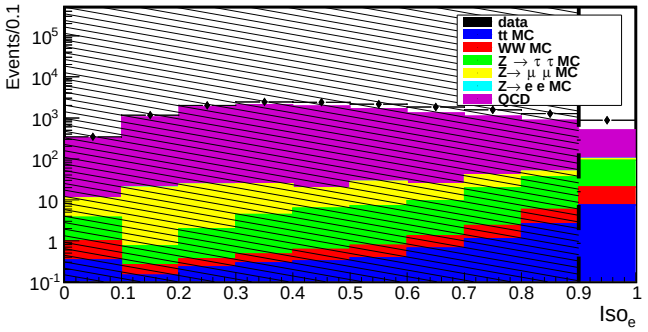


**Figure 6.12:** The isolation quantity on candidate electrons in selected events. By requiring this quantity to be $\geq$ 0.90, which corresponds to the unshaded area, contributions from QCD backgrounds are significantly reduced.

*Jet NN out*: Requiring jets to have a neural network $b$-tagger classification of $>$ 0.90 means the jet is strongly identified as being $b$-like, and is very unlikely to be originating from a gluon or light flavour quark. The output for all jets in all events passing the loose requirements is presented in Figure 6.14. The estimated purity after this requirement is $\sim$47.6%.

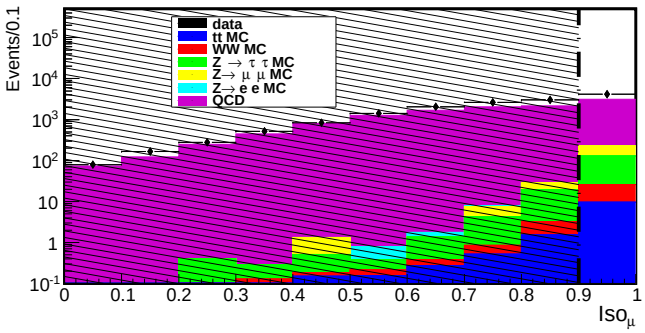


**Figure 6.13:** The isolation quantity on candidate muons in selected events. By requiring this quantity to be $\geq 0.90$, which corresponds to the unshaded area, contributions from QCD backgrounds are significantly reduced.

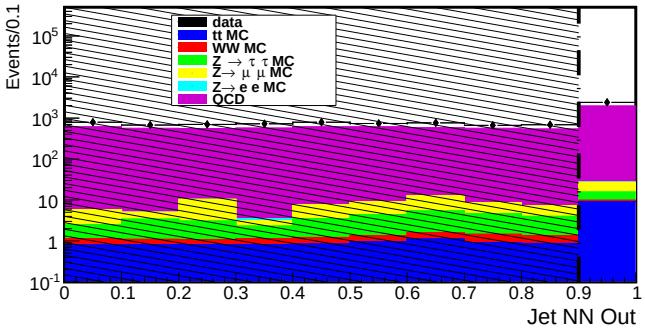


**Figure 6.14:** The neural network output for all jets in events requiring the loose selection.

Events are also removed from the sample where they pass the $Z \to \mu\mu$ criteria. The requirements for this are documented in Appendix A. The efficiency of this requirement on $t\bar{t}$ Monte Carlo is found to be compatible with 100%.

After application of the full selection requirement 6 candidate events are found in data. The invariant mass spectrum of the candidates against Monte Carlo is presented in Figure 6.15. The Kolmogorov-Smirnov [177] probability of the data being compatible with the considered backgrounds and the $t\bar{t}$ signal is found to be $\sim$58%.

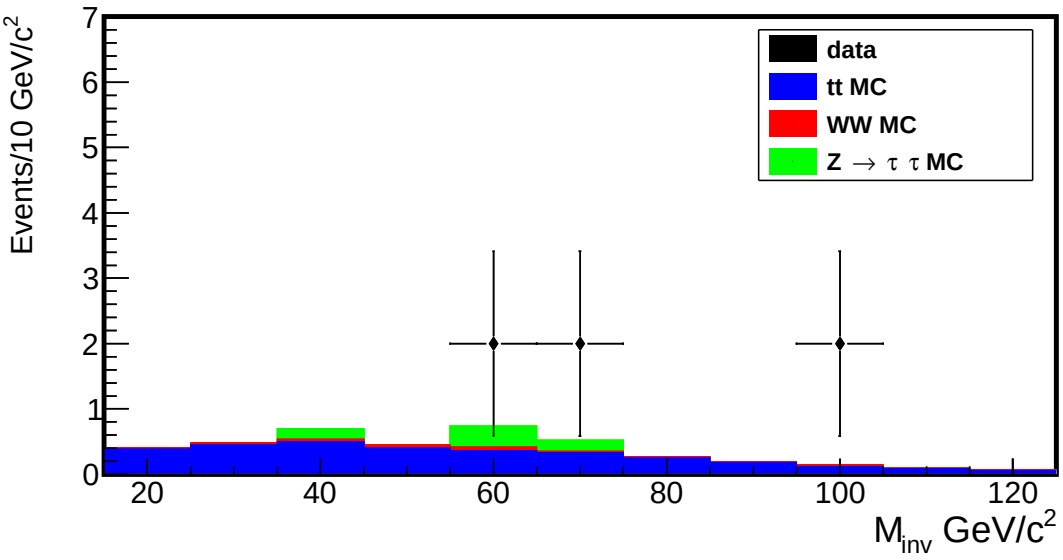


**Figure 6.15:** The invariant mass spectrum for the lepton pair for all the candidate events and the Monte Carlo expectation after the selection procedure is utilised. The Monte Carlo and QCD contributions have been described in Section 6.3, and the data sample utilised is the full LHCb 2012 2.01 fb$^{-1}$ sample.

## 6.6 Control Regions

The chosen technique to understand the QCD contributions was the use of control regions. These are regions that do not correspond to the signal phase space and are obtained by either changing the charge requirements, loosening some of the selection requirements, or inverting them.

Two control regions are utilised, the first one to test the hypothesis of symmetry between the *OS* and *SS* channels, and the second one to estimate background contributions to the signal region.

### 6.6.1 Anti-Isolated Channel

The anti-isolated region is used to test the assumed hypothesis of equality between the opposite sign and same sign channels. It is the implementation of the full selection requirements with only the isolation criteria changed. Instead of requiring $I_l > 90\%$ used in the full selection process, the anti-isolated requirement that $I_l < 40\%$ is imposed instead. QCD backgrounds, due to their origin as either $q\overline{q}$ production or similar processes (such as $W + jet$), have a probability that describe the kinematics of one or more of the jets appearing as an isolated lepton. Due to the inherent underlying activity in the jet, it is a reasonable assumption that significantly more QCD events would be selected using anti-isolation rather than the isolation criteria.

It is found after the full selection that 4 events remain in the opposite sign channel, and 3 in the same sign channel (as shown in Figure 6.16), which is consistent with the assumed hypothesis of symmetry between the *OS* and *SS* channels. With only the $\mu$,$e$ requirements imposed, a total of 12 events are found in the *OS* channel, and 7 in the *SS*. This is shown in Figure 6.17, and is also compatible with the symmetry hypothesis.

### 6.6.2 Same Sign Channel

The same sign channel is used to estimate contributions from QCD events and $ZW$ boson decays, which are then subtracted from the signal contribution. It is expected that these will be charge symmetric between the same sign channel and the opposite sign channel, as either lepton from a $Z \rightarrow \mu\mu$ decay could be outside the acceptance, leaving equal possibilities of $ZW \rightarrow \mu^+e^+$ and $ZW \rightarrow \mu^-e^-$ pairs. The full analysis is repeated on the channel searching for $\mu^\pm e^\pm$ events (as opposed to $\mu^\pm e^\mp$ events), and the final number of events are considered to be the background in the opposite sign channel. The number of events observed here are subtracted away from potential signal candidates observed in the $\pm\mp$ channel.

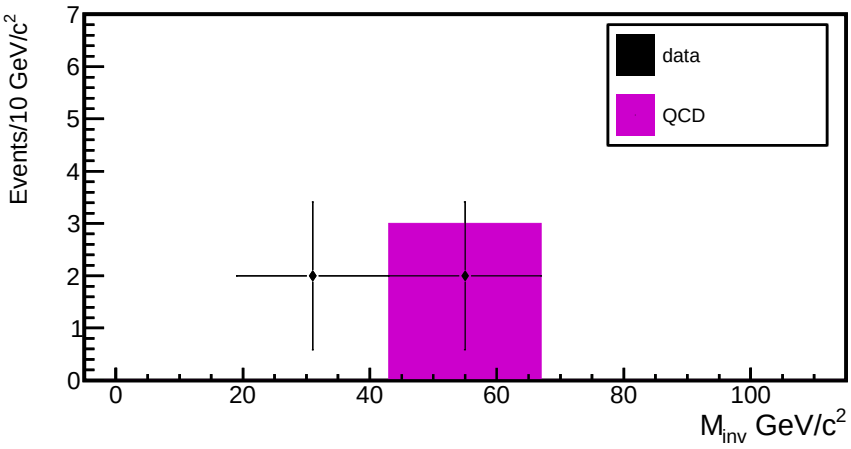


**Figure 6.16:** Opposite sign versus same sign data for full selection requirements with the anti-isolation requirement. 4 events are found in the *OS* channel, and 3 in the *SS*. The same-sign contribution is labelled "QCD" on this plot. The compatibility between the data and QCD is found to be $\sim 78\%$ using the Kolmogorov-Smirnov test.

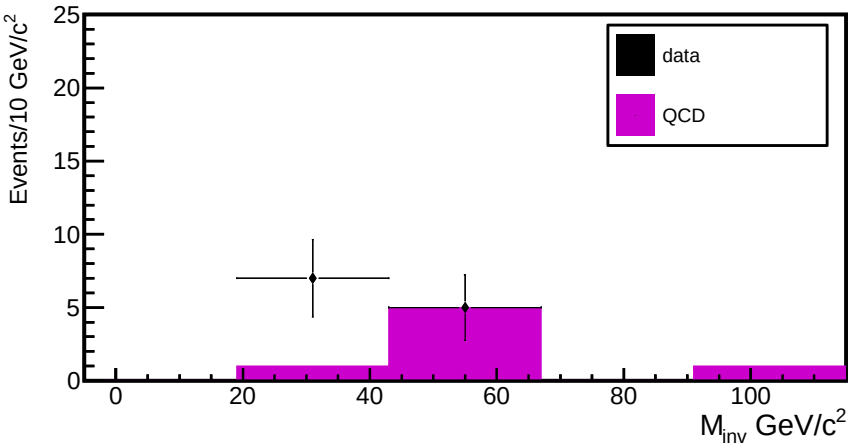


**Figure 6.17:** Opposite sign versus same sign data for only $\mu, e$ requirements with the anti-isolation requirement. 12 events are found in the opposite sign channel, with 7 in the same sign channel. The same-sign contribution is labelled "QCD" on this plot. The compatibility using the Kolmogorov-Smirnov test is found to be $\sim 36\%$.

## 6.7 Cross-Section Determination

The cross-section can be determined through the relation:

$$\sigma = \frac{N_{sig} - N_{bkg}}{\epsilon_{rec}\epsilon_{sel}\mathcal{L}A} \tag{6.2}$$

where $\mathcal{L}$ represents the luminosity of the data sample used and is quoted in units of $\text{fb}^{-1}$, $\epsilon_{sel}$ represents the selection efficiency and $\epsilon_{rec}$ represents the reconstruction efficiency, and $A$ represents the acceptance. These are documented in more detail in the following sections.

### 6.7.1 Luminosity

The instantaneous luminosity is determined using two different techniques. The first is a Van der Meer scan [178, 179], where one beam is scanned sideways across the other, and the collision rate is measured as a function of the beam displacement to ascertain the beam profile. The second method, which uses vertex detection of beam-gas interactions [180], reconstructs the vertices originating from material interactions to determine the beam profile. The information ascertained from these scans can then be used in Equation (3.3) to calculate the luminosity, with the comparison of the value obtained by both methods providing an uncertainty. This provides a discrepancy between the two measurement techniques of 3.5% [181]. For the data sample used here, which represents 2.01 $\text{fb}^{-1}$, this provides an uncertainty of $\pm$ 70.3 $\text{pb}^{-1}$.

### 6.7.2 Background Estimation

The background contributions are estimated through Monte Carlo samples, normalised by luminosity and are summarised in Table 6.2.

Selection systematic uncertainties and cross-section uncertainties are added in quadrature to yield a systematic uncertainty on the WW sample of $\sim$10.5%, and on the $Z \rightarrow \tau\tau$ sample of 51.4%. The overall uncertainty on the backgrounds remains unchanged at $\pm$1.05 events e.g. the systematic uncertainties are negligble.

| Sample | Contributions [Evts/2.01 fb$^{-1}$] | Statistical Uncertainty |
|---|---|---|
| WW | 0.32 | 0.02 |
| $Z \to \tau\tau$ | 0.65 | 0.33 |
| QCD | 0.00 | 1.00 |
| Total | 0.97 | 1.05 |

**Table 6.2:** A summary table of the expected background contributions from Monte Carlo.

## 6.8 Selection Related Systematic Uncertainties

Table 6.3 summarises the selection efficiency in this analysis, as well as the statistical and systematic uncertainties, and their combination in quadrature. Since the statistical uncertainties define the precision of the systematic uncertainties, these are combined into a single total systematic uncertainty. The final result, which has an uncertainty of 7%, is:

$$\epsilon_{sel} = 0.535 \pm 0.037(\text{syst.})$$

| Requirement | Efficiency | Stat. Uncert. [%] | Syst. Uncert. [%] |
|---|---|---|---|
| ncand | 0.972 | 0.9 | 0.0 |
| $M_{inv(\mu,e)}$ | 0.925 | 0.9 | 4.5 |
| $IP_\mu$ | 0.992 | 1.0 | 0.7 |
| $IP_e$ | 0.990 | 1.0 | 0.7 |
| $IPCA$ | 0.954 | 1.0 | 1.5 |
| $I_\mu$ | 0.852 | 1.0 | 4.3 |
| $I_e$ | 0.793 | 1.0 | 0.8 |
| Combined | 0.535 | 2.5 | 6.5 |

**Table 6.3:** A summary of the selection requirements and their associated uncertainties.

The selection related systematic uncertainties are documented in full in Appendix A.

## 6.9 Reconstruction Efficiency and Systematic Uncertainties

A summary table of the efficiencies of the reconstruction and the systematic uncertainties of these quantities is presented in Table 6.4. The combined value is the product of the efficiencies, and the combined systematic uncertainty is the weighted quadrature combination of the systematic uncertainties and their respective quantities. $\epsilon_{trig}$ refers to the efficiency of the trigger used in this analysis, $\epsilon_{GEC}$ refers to the global event cut used on the same triggering line, $\epsilon^{l}_{track}$ is the tracking efficiency for a specific type of lepton, $\epsilon_{ID}$ is the identification efficiency of a specific lepton, $\epsilon_{reso}$ is the resolution efficiency of the detector, $\epsilon_b$ is the $b$-tagging efficiency which also factors in the reconstruction efficiency for $b$-jets, and $\epsilon_{veto}$ is the efficiency of the muon ECAL cluster veto.

| Parameter | Efficiency | Systematic Uncertainty [%] |
|---|---|---|
| $\epsilon_{trig}$ | 0.756 | 2.0 |
| $\epsilon_{GEC}$ | 0.842 | 2.7 |
| $\epsilon^{\mu}_{track}$ | 0.946 | 1.5 |
| $\epsilon^{\mu}_{ID}$ | 0.986 | 1.2 |
| $\epsilon^{e}_{track}$ | 0.886 | 2.9 |
| $\epsilon^{e}_{ID}$ | 0.843 | 1.2 |
| $\epsilon_{reso}$ | 0.738 | 0.7 |
| $\epsilon_b$ | 0.579 | 16.8 |
| $\epsilon^{\mu}_{veto}$ | 0.979 | 2.0 |
| Combination | 0.186 | 17.6 |

**Table 6.4:** A summary of the reconstruction efficiencies and their associated systematic uncertainties.

This gives a combined reconstruction efficiency for events which have $2.0 < \eta_{\mu,e} < 4.5$, $2.0 < \eta_b < 4.5$, $P_T(\mu, e) < 15$ GeV/c and $P_T(b) < 5$ GeV/c of

$$\epsilon_{rec} = 0.186 \pm 0.033.$$

The reconstruction efficiencies and their systematic uncertainties are documented in full in Appendix A.

## 6.10 Acceptance and Final State Radiation

To translate from the measured number of candidates to the fiducial cross-section, it is also important to take into account acceptance effects. This is particularly true in the case of the $b$-quark, where a $b$-quark just outside of the $\eta$ range can still create a jet which is identified as being inside the $\eta$ range, and being tagged as a $b$-jet. The resulting acceptance factor is computed to be $1.035 \pm 0.006$, where the uncertainty arises from the combined statistical uncertainties on the component quantities. The method of calculating this acceptance is documented further in Appendix A.

## 6.11 Results

One of the candidate events is shown in Figure 6.18. A summary table of the values and their associated uncertainties is presented in Table 6.5.

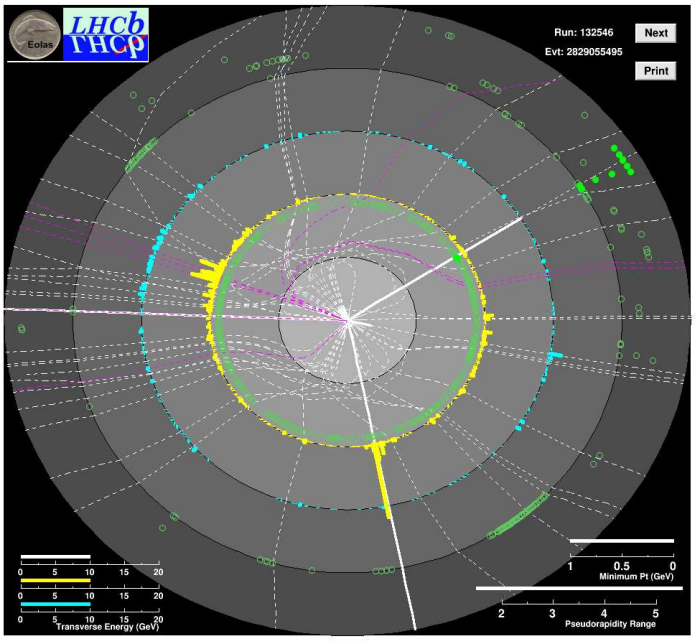


**Figure 6.18:** An event display for a data candidate. For a description of the graphic, please see Figure 6.4.

| Component | Value | Uncertainty [%] |
|---|---|---|
| N | 6 | $^{+60.0}_{-40.0}$ |
| $N_{bkg}$ | 0.97 | 108.2 |
| $\epsilon_{rec}$ | 0.186 | 17.7 |
| $\epsilon_{sel}$ | 0.535 | 6.9 |
| A | 1.035 | 0.6 |
| $L$ | 2.01 | 3.5 |

**Table 6.5:** A summary of the components and their respective uncertainties for the cross-section calculation.

The cross-section calculation (Equation (6.2)) can be restated now as:

$$\sigma = \frac{6.00 - 0.97}{0.186 \cdot 0.535 \cdot 1.035 \cdot 2.008} \tag{6.3}$$

which provides the result of $\sigma = 24.3$ fb. The systematic uncertainties on the reconstruction and selection efficiencies of 17.6% and 7.0% are combined in quadrature with the background systematic uncertainty of 20.9% and the acceptance uncertainty of 0.6% to give a total systematic uncertainty of 28.2%, or 6.9 fb. The luminosity uncertainty is calculated to be 0.9 fb, and the statistical uncertainties are calculated to be $+14.6$ and $-9.7$ fb by looking at the 68% confidence limit for a Poisson distribution with a mean of 6 events and propagating these uncertainties to the cross-section.

The final cross-section of

$$\sigma = 24.3^{+14.6}_{-9.7}(\text{stat.}) \pm 6.9(\text{syst.}) \pm 0.9(\text{lum.})\text{fb}$$

is consistent with the calculated prediction of:

$$\sigma_{\text{fid}}(\sqrt{s} = 8 \text{ TeV}) = 17.5^{+1.2}_{-1.0}(\text{theo.}) \pm 0.2(\text{stat.}) \pm 2.9(\text{PDF})\text{fb}.$$

The cross-section is limited by the statistics available, with the lower statistical limit only comparable to the systematic uncertainty after $\sim 2\times$ the data sample, or $\sim 4$ fb$^{-1}$ of delivered luminosity. After this, the dominant uncertainty is driven by the $b$-tagger uncertainty and the QCD contribution, however it can be expected that the QCD uncertainty will also decrease with increasing data. The $\sim 27\%$ systematic uncertainty is larger than the recent ATLAS or CMS results discussed in Chapter 2, which are typically of the order of $\sim 15\%$.

Using a method similar to the one employed by CDF/D0 for estimating the signal significance [182], in which toy experiments based on the background expectation and its uncertainty are used, it is possible to estimate the probability of obtaining the observed number of events through background fluctuations alone. This is performed by using a Gaussian distribution to generate a random expected number of background events (discarding experiments in which the expected number of background events are <0), and then generating a random number according to a Poisson distribution using this expected number of background events. This quantity is evaluated over 100,000,000 pseudo-experiments to be $\sim 1.3\%$, which corresponds to a significance of $\sim 3.7\sigma$.

## 6.12 Outlook

For a hypothetical increased data sample of 50 fb$^{-1}$ at 8 TeV, assuming the same systematic uncertainties, it is possible to estimate a statistical uncertainty of 8.3%, and assuming no contributions in the background control region, the cross-section would be accurate to $\sigma \pm 8.3\%(\text{stat.}) \pm 20.1\%(\text{syst.}) \pm 3.5\%(\text{lum.})$, or a $4.5\sigma$ measurement. The resultant 150 top candidates would, assuming a Standard Model asymmetry, using the equation [55]:

$$\delta A = \sqrt{\frac{2 \cdot A \cdot (1 - A)}{N_{evts}}} \tag{6.4}$$

yields a result of $A_C = 1.6^{+1.5}_{-1.5}\%$.

A fiducial cross-section can be calculated for $\sqrt{s} = 14$ TeV using the same methods detailed above. This provides a result of $\sigma_{\text{fid}} = 283.6 \pm 2.9$ (stat.) $\pm$ 22.5 (syst.) fb. If the same efficiencies are assumed as previously measured, of 18.9% $\times$ 53.5%, it is possible to expect 10.1% of these events to be reconstructed and selected, thus 29 events per fb$^{-1}$. With a nominal data collection of 6 fb$^{-1}$, approximately 175 reconstructed $t\bar{t}$ events should be available. This would yield a statistical uncertainty of approximately $\sim 8\%$.

# Chapter 7

# Conclusion

This thesis has explored the ability to measure and predict radiation damage in the LHCb VELO through measurement and analysis of IV scans. The quantification and understanding of this radiation damage is an important part of the operation of the detector, and the exploitation of the data acquired by the experiment. The data taken by the IV scans has been compared to simulation and allows for predictions regarding the future behaviour of the detector, and its lifetime, to be made. Projections have been calculated for 6 fb$^{-1}$ of delivered luminosity, where the currents range from 90→150 $\mu$A. It has also been projected that, for a simulated thermal runaway limit of 1 mA, the VELO should be able to withstand, from a current perspective, 50 fb$^{-1}$.

This thesis has also documented a technique for a cross-section measurement for top quark pair production in the forward region at LHCb using a dilepton+$b$-jet channel, analysed using 2.01 fb$^{-1}$ of data collected by LHCb in 2012 at $\sqrt{s} = 8$ TeV. This is an important foundation for potential asymmetry measurements. The technique imposes a selection requirement on the two leptons and an additional jet purity requirement. Backgrounds are analysed through a combination of data driven and Monte Carlo studies. Efficiencies are studied using Monte Carlo and data, and the comparisons thereof, to translate an observed number of events back into a cross-section which can then be compared with theoretical predictions for $t\bar{t} \to \mu eb$ with the leptons and a $b$-quark in $2.0 < \eta < 4.5$. A result is obtained of

$$\sigma_{fid} = 24.3 \pm {}^{+14.6}_{-9.7}(\text{stat.}) \pm 6.9(\text{syst.}) \pm 0.9(\text{lum.})\text{fb}$$

where the first uncertainty is statistical, the second uncertainty systematic, and the third arising from luminosity uncertainty. The accumulated number of events represents

a $\sim 3.7\sigma$ excess over the background-only hypothesis, but is limited by the available data sample. The analysis becomes systematically limited at $\sim 4$ fb$^{-1}$, with a systematic uncertainty of $\sim 27\%$, which is greater than the ATLAS or CMS systematic uncertainties of $\sim 15\%$. The LHC should restart data taking in 2014 at a centre of mass energy of 14 TeV, where the fiducial cross-section for top pair production increases $16\times$ to $\sigma_{fid} = 283.6$ fb, at which point 6 fb$^{-1}$ of accumulated data should result in a sample of $\sim 8\%$ statistical uncertainty.

# Appendix A

# Efficiencies and Systematic Uncertainties

## A.1 Pre-selection

$IP_l$: An impact parameter requirement searches for leptons which have a very low impact parameter, of <35 $\mu$m, with a primary vertex, compatible with a lepton originating from that primary vertex smeared by detector effects. This requirement assists the transverse momentum requirements in ensuring the leptons originate from heavy parents. This suppresses long-lived intermediate stages on some backgrounds such as $Z \to \tau\tau$. These are shown in Figure A.1 and Figure A.2. The estimated purity after this requirement is $\sim$1.1%.

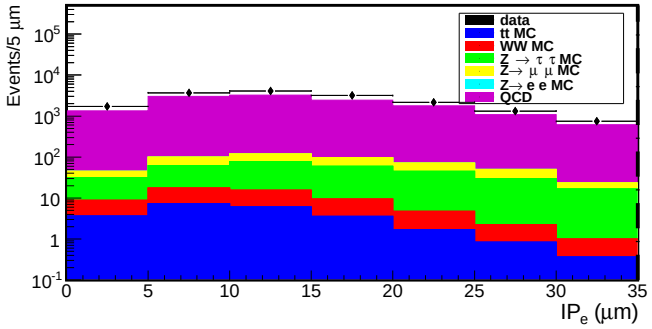


**Figure A.1:** The impact parameter for the electron. Pre-selection requirements have been imposed on this quantity already which are not more strictly selected upon after. Signal contribution continues to decay after $IP_l > 25$ $\mu$m, and this quantity is not selected upon.

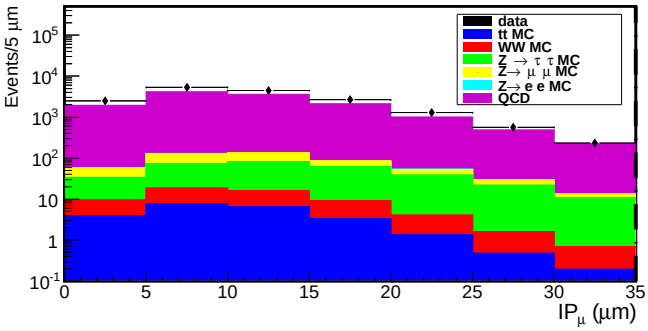


**Figure A.2:** The impact parameter for the muon. Similarly to the electron, pre-selection requirements have been imposed on this quantity and they are not changed for the full selection process.

## A.2 Selection Related Systematic Uncertainties

Selection efficiencies are determined from Monte Carlo samples. Differences between Monte Carlo and data are evaluated to provide systematic uncertainties on individual requirements. The selection efficiencies for the requirements in place in this analysis are presented in Table A.1, with the statistical uncertainties on the quantities presented as well. A source of systematic uncertainties arises from the differences in distributions

| Requirement | Events Surviving | Requirement Efficiency | Stat. Uncertainty [%] |
|---|---|---|---|
| Initial | 11854 | N/A | |
| $M_{inv(\mu,e)}$ | 10956 | 0.924 | 0.9 |
| $IP_\mu$ | 10875 | 0.993 | 1.0 |
| $IP_e$ | 10766 | 0.990 | 1.0 |
| $IPCA$ | 10275 | 0.954 | 0.9 |
| $I_\mu$ | 9043 | 0.880 | 0.9 |
| $I_e$ | 7368 | 0.815 | 1.0 |
| Combined | 7368 | 0.622 | 2.3 |

**Table A.1:** A summary table of the efficiencies as taken directly from Monte Carlo. Some of the values are subsequently corrected later.

between Monte Carlo and data. These distributions are evaluated through Monte Carlo and data comparisons in control channels. The $\mu$ lepton distributions are evaluated using the methodology of the LHCb $Z \to \mu\mu$ analysis [183], and similarly differences in

the electron distributions are evaluated using the methodology of the LHCb $Z \rightarrow ee$ analysis [98]. The requirements for these are documented in Table A.2 and Table A.3.

| Requirements |
|---|
| $P_T\mu > 20$ GeV/c |
| $60 < M_{\mu\mu} < 120$ GeV/c$^2$ |

**Table A.2:** Selection process for $Z \rightarrow \mu\mu$ events used to compare Monte Carlo and data distributions.

| Requirements |
|---|
| $P_Te > 20$ GeV/c |
| $M_{ee} > 40$ GeV/c$^2$ |

**Table A.3:** Selection process for $Z \rightarrow ee$ events used to compare Monte Carlo and data distributions.

Systematic uncertainties arising from the differences in distributions between Monte Carlo and data is taken by calculating a requirement efficiency on both samples, and the difference between the efficiency is taken as the systematic uncertainty on the quantity.

### A.2.1 Muon Transverse Momentum Uncertainty

The transverse momentum of leptons is found to be well described between Monte Carlo and data for the $Z \rightarrow \mu\mu$ channel in Figure A.3. This is thus taken without a systematic uncertainty.

### A.2.2 Impact Parameter Uncertainty

Impact parameter is evaluated from track level information in $Z \rightarrow \mu\mu$ data and Monte Carlo, and is presented in Figure A.4. The agreement is found to be good between Monte Carlo and data, with a systematic uncertainty evaluated by taking the difference in the efficiency of requiring $IP < 35\mu m$. The efficiency of this requirement is found to be 0.963 in Monte Carlo and 0.970 in data, which contributes a systematic uncertainty on the impact parameter distribution of $\pm$ 0.007 on both leptons. The difference in the

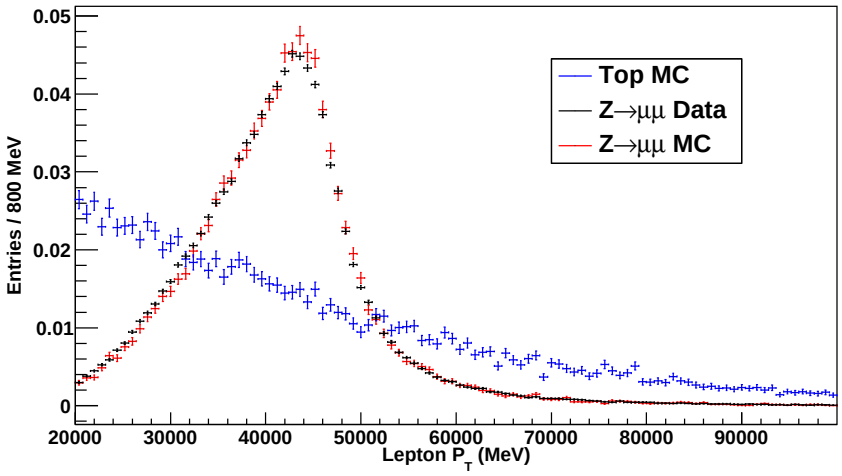


**Figure A.3:** The transverse momentum of $Z \rightarrow \mu\mu$ events in data and Monte Carlo, with $\mu$ from $t\bar{t}$ events included.

impact parameter from the $t\bar{t}$ Monte Carlo sample with respect to the $Z \rightarrow \mu\mu$ can be attributed to the increased activity in the $t\bar{t}$ events due to the additional requirement of a $b$-jet. This additional $b$-jet results in having significantly more particles with which to assist in the calculation of the vertex position.

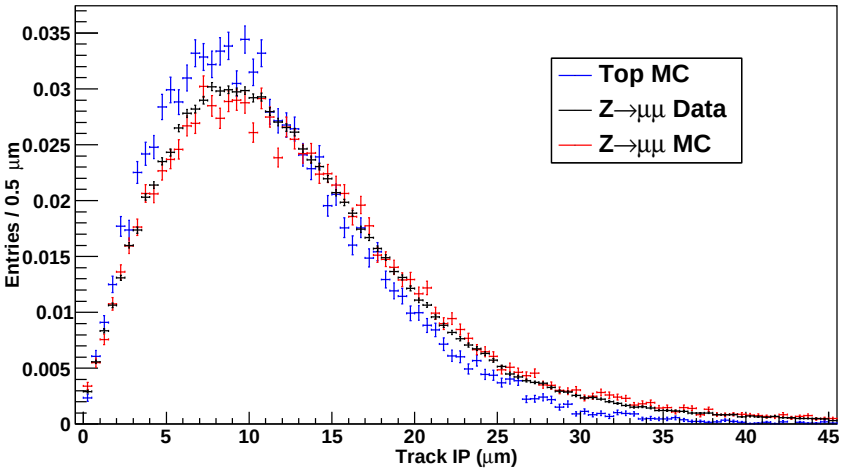


**Figure A.4:** Impact parameter comparisons between Monte Carlo and data for $Z \rightarrow \mu\mu$. $t\bar{t}$ Monte Carlo is used to evaluate the impact parameter for $\mu$ particles arising from $t$ decays.

This can be re-stated as:

$$\epsilon_{\mu(e)} = 0.993(0.990) \pm 0.007(\text{syst.}) \pm 0.010(\text{stat.})$$

### A.2.3 Impact Parameter Closest Approach Uncertainty

The impact parameter closest approach is found to be in good agreement between Monte Carlo and data in Figure A.5. The selection efficiency is evaluated for $IPCA_{ll} < 35\mu m$ and is found to be 0.389 in Monte Carlo and 0.403 in data. This contributes a systematic uncertainty of $\pm 0.014$. The $t\bar{t}$ Monte Carlo has a significantly reduced IPCA due to the nature of the Z events - $Z \rightarrow ll$ decays typically result in the two leptons appearing back-to-back in the *(x,y)* plane - or $\Delta\Phi \sim 180°$. This gives them an IPCA typically of $\sim 2 \times$ IP. For decays originating from $WW$ bosons, this kinematic restraint is not imposed, allowing the leptons to have no significant angular dependence.

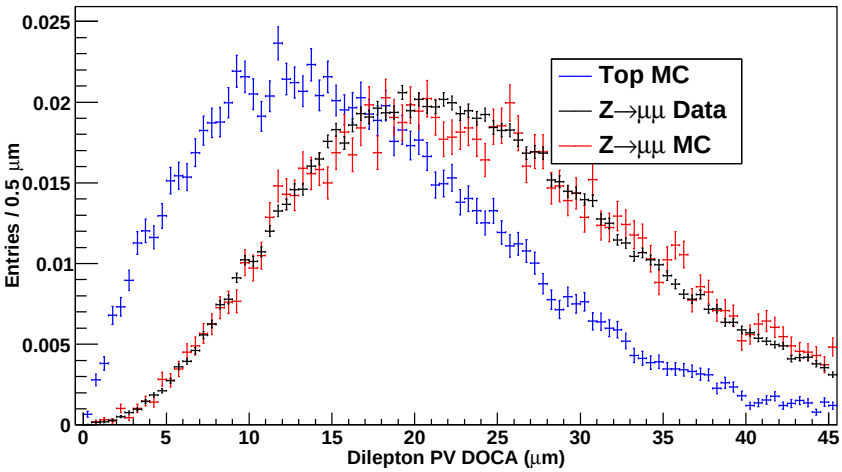


**Figure A.5:** Impact parameter closest approach agreement between $Z \rightarrow \mu\mu$ MC and data. The quantity is also plotted for $IPCA_{\mu e}$ for $t\bar{t}$ Monte Carlo.

This can be summarised as:

$$\epsilon_{IPCA(\mu,e)} = 0.954 \pm 0.014(\text{syst.}) \pm 0.009(\text{stat.})$$

### A.2.4 Muon Isolation Uncertainty

The muon isolation is found to be in disagreement between $Z \rightarrow \mu\mu$ Monte Carlo and data. This uncertainty is further compounded by the poorly modelled $NPV$ distribution between the $t\bar{t}$ Monte Carlo and data, which the isolation quantity is heavily dependent on. The assumed cause is a badly modelled underlying event in simulation, which introduces an NPV-based dependency.

To account for the discrepancies, it becomes necessary to perform a bin-by-bin correction based on the number of primary vertices in an event. It is also necessary to re-weight the $t\bar{t}$ sample to calculate the isolation efficiency correctly. The isolation quantity is composed of two parameters, the muon $P_T$ and the charged track energy in a cone of $\Delta R = 0.5$ around the muon. Since the muon transverse momentum is well modelled in data and Monte Carlo, the uncertainty is taken to be on the cone energy. To correct the isolation quantity, scale-factors are applied to the cone energy to match data and Monte Carlo distributions for the isolation variable.

A Kolmogorov-Smirnov (K-S) test is a measure of the compatibility between a data sample and a hypothesis, or two samples. In the context used here, it returns a probability that tested sample(s) are from the same distribution. By iterating over a range of scale-factors, and applying the K-S test, it is possible to find the most optimal scale-factor to correct the distributions on a bin-by-bin basis. The unoptimised plot is presented in Figure A.6 for $NPV = 1$.

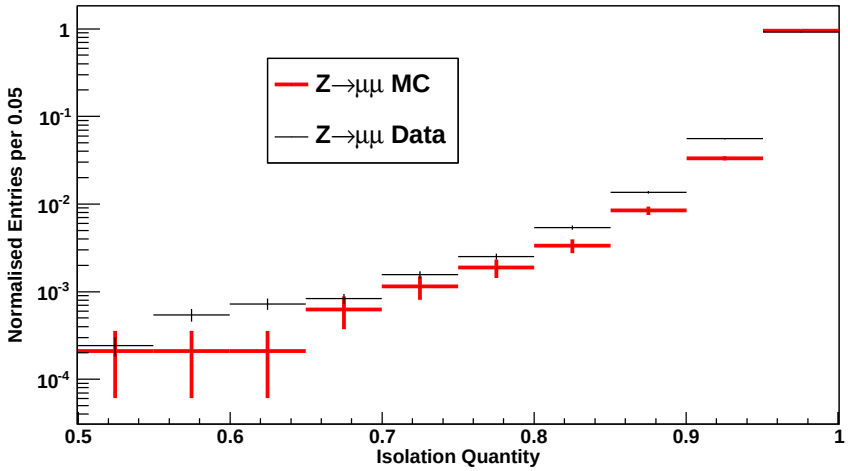


**Figure A.6:** Unoptimised distributions for $Z \rightarrow \mu\mu$ data and Monte Carlo. The isolation is found to be significantly different in Monte Carlo than data.

The scalefactors obtained from the optimisation routine is listed in Table A.4. The comparative optimised plot is presented in Figure A.7.

| $NPV$ | Scalefactor |
|---|---|
| 1 | 1.37 |
| 2 | 1.35 |
| 3 | 1.43 |
| 4 | 1.47 |
| 5 | 1.45 |
| 6 | 1.71 |
| 7 | 1.51 |

**Table A.4:** Scalefactors listed by $NPV$ obtained from $Z \rightarrow \mu\mu$ Monte Carlo and data comparisons.

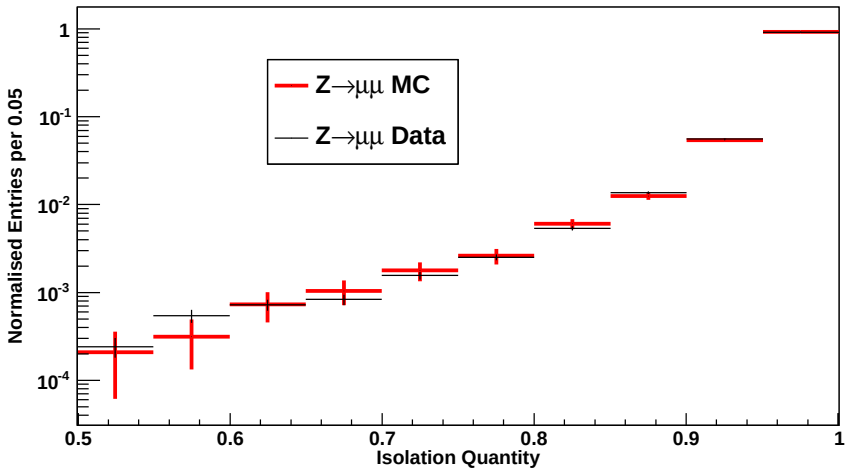


**Figure A.7:** The scaled distribution for $NPVs = 1$, using the K-S test optimisation.

The efficiency of passing the selection requirement is also strongly correlated with the number of primary vertices in an event, which is summarised in Table A.5. To accurately calculate the isolation rate, the $t\bar{t}$ sample must be re-weighted by the data distribution of primary vertices. The efficiency is also significantly effected by the presence of a $b$-jet in the event, therefore the $b$-jet selection process is applied to the $t\bar{t}$ Monte Carlo sample in the calculation of the isolation efficiency.

| $NPVs$ | Passing [Events] | Total [Events] | Pass rate | Pass Rate Uncert. | Re-Weight Factor |
|---|---|---|---|---|---|
| 1 | 4433 | 5054 | 0.877 | 0.005 | 0.271 |
| 2 | 3142 | 3711 | 0.847 | 0.006 | 0.372 |
| 3 | 1222 | 1528 | 0.800 | 0.011 | 0.235 |
| 4 | 305 | 421 | 0.724 | 0.023 | 0.092 |
| 5 | 54 | 92 | 0.587 | 0.057 | 0.024 |
| 6 | 5 | 8 | 0.625 | 0.234 | 0.005 |
| 7 | 1 | 1 | 1.000 | 0.840 | <0.001 |

**Table A.5:** The pass rate and the re-weight factor as a function of the number of primary vertices in an event for $t\bar{t}$ Monte Carlo.

The combined pass rate for the re-weighted $t\bar{t}$ Monte Carlo yields a result of

$$\epsilon_{I_\mu} = 0.825 \pm 0.012(\text{stat.})$$

The systematic uncertainty on the isolation quantity is taken to be the post-scaled discrepancy between the isolation requirement efficiency on $Z \rightarrow \mu\mu$ Monte Carlo and data, which yields results of 0.936 and 0.973 respectively, which contributes a $\pm$ 0.037 systematic uncertainty.

$$\epsilon_{I_\mu} = 0.825 \pm 0.012(\text{stat.}) \pm 0.037(\text{syst.})$$

A systematic uncertainty also arises from the uncertainty on the $NPV$ distribution, which differs from $Z \rightarrow \mu\mu$ and $Z \rightarrow ee$ data. The $t\bar{t}$ NPV re-weighting process is performed with both scales, and the difference between them is taken to be the systematic uncertainty. This is found to be 0.825 and 0.832, which is contributes a $\pm$ 0.007 uncertainty. This is combined in quadrature with the discrepancy on the selection requirement, as well as the statistical uncertainty on the pass rate, to yield an overall systematic uncertainty of

$$\epsilon_{I_\mu} = 0.852 \pm 0.040$$

Histograms for the isolation quantity for all the primary vertices, and the K-S test optimised values, are available in Appendix B.1.

### A.2.5 Electron Transverse Momentum Uncertainty

The electron transverse momentum is found to differ significantly from Monte Carlo to data in the $Z \rightarrow ee$ channel. The systematic uncertainty arising from this is calculated here but accounted for separately as a kinematic feature manifesting as $\epsilon_{reso}$, in Section A.3.8. The electron $P_T$ is found to be in poor agreement between Monte Carlo and data as demonstrated in Figure A.8.

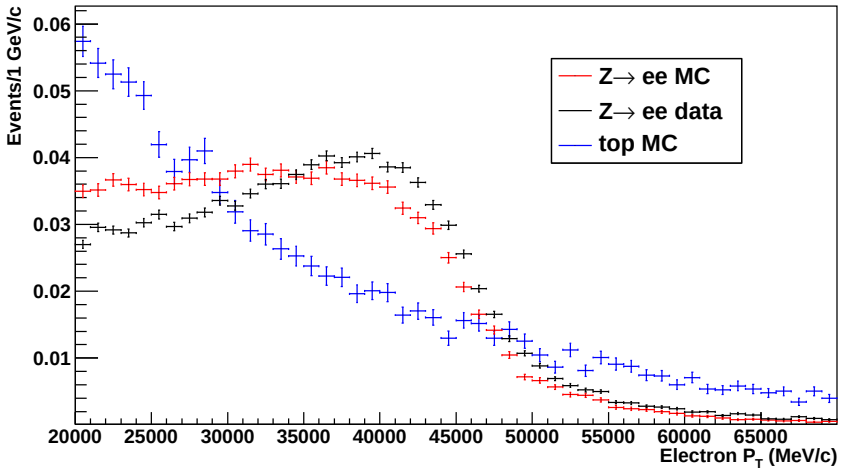


**Figure A.8:** Electron transverse momentum between Monte Carlo and data. The peak is significantly smeared in comparison to the $Z \rightarrow \mu\mu$ peak due to ECAL saturation.

The electron $P_T$ is corrected by using a calibration scale-factor. It is found through an iterative process that scaling the $P_x$ and $P_y$ components by a linear $1.03 \pm 0.01$ provides best closest agreement between Monte Carlo and data. The corrected transverse momentum spectrum is illustrated in Figure A.9.

Once the $P_T$ correction factor has been found, the resolution efficiency is calculated from $t\bar{t}$ Monte Carlo to be 0.736. The systematic uncertainty on this efficiency is calculated to be the effect of the propagation of the uncertainty on the scale-factor (e.g. $\pm$ 0.01) upon the resolution efficiency, and combined in quadrature with the statistical uncertainty on the resolution. This value combined gives a $\pm$ 0.004 uncertainty. The uncertainty is then combined with the statistical uncertainty of $\pm$ 0.003 in quadrature to provide a result of $\pm$ 0.005.

The effect of the electron smearing is presented in Figure A.10, which displays the Monte Carlo truth $P_T$ for electrons in a $t\bar{t}$ sample against the reconstructed $P_T$ for MC events with $P_T$ >15 GeV/c. Events smeared to the left of $y = x$ represent electrons that

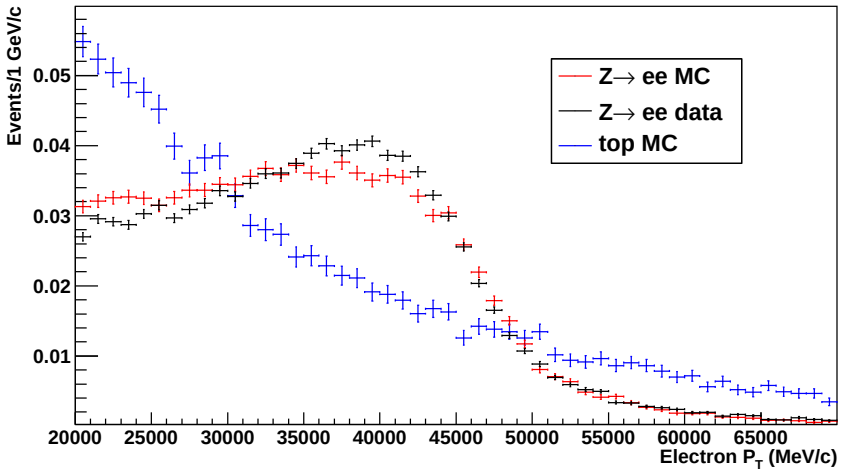


**Figure A.9:** The corrected electron $P_T$ spectrum after a correction factor has been applied.

have transverse momenta reconstructed below the Monte Carlo truth value. The same plot is produced for muons in Figure A.11 for comparative purposes.

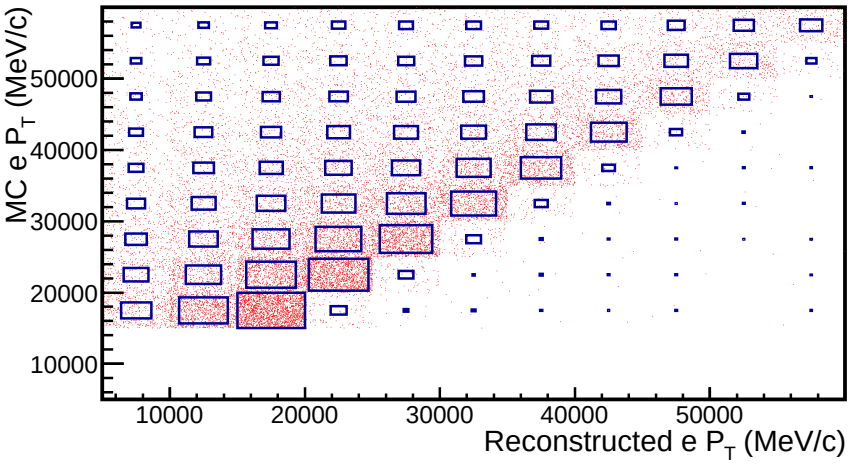


**Figure A.10:** Electron $P_T$ MC vs reconstructed for $t\bar{t}$ electrons.

## A.2.6 Electron Isolation Uncertainty

The isolation on the electron, similar to the isolation of the muon as described in Section A.2.4, is found to be in disagreement between Monte Carlo and data, and this is further affected by the discrepancies on the $NPV$ distribution. The same method is

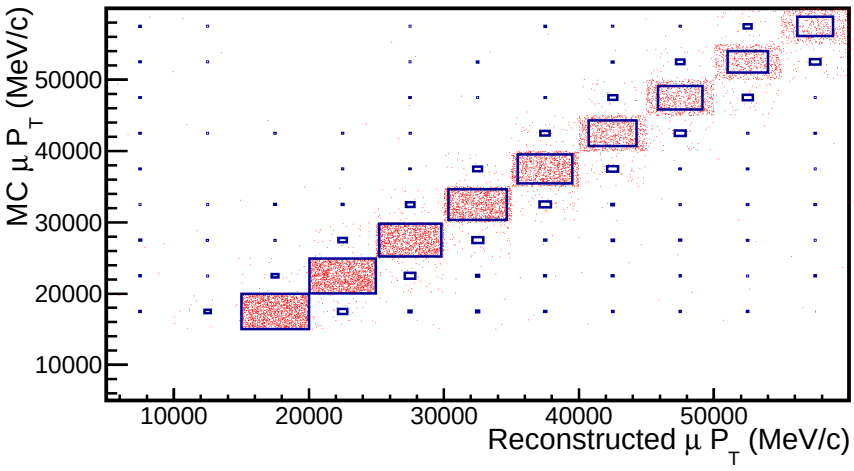


**Figure A.11:** Muon $P_T$ MC vs reconstructed for $t\bar{t}$ muons.

employed to correct the quantity. The unscaled distribution for $NPV = 3$ is presented in Figure A.12.

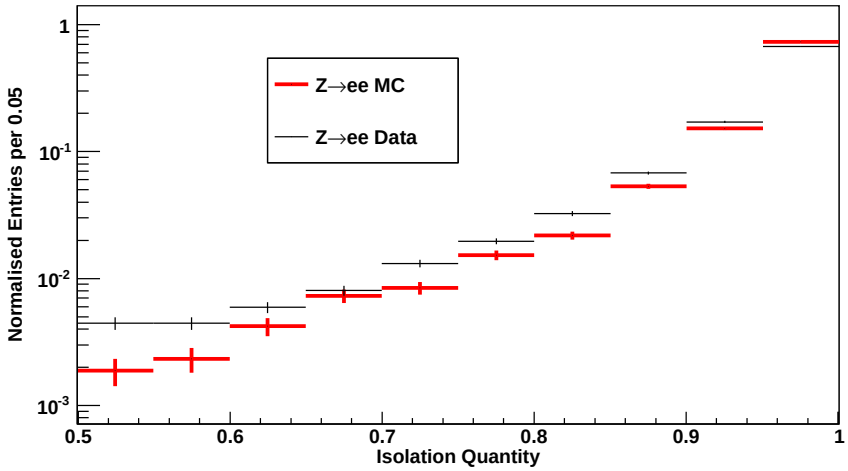


**Figure A.12:** Electron isolation for $Z \rightarrow ee$ MC and data before any Monte Carlo corrections are applied.

It is necessary to implement the same bin-by-bin technique for the electrons, and the scale-factors are summarised in Table A.6. An example plot scaled is presented for $NPV = 3$ in Figure A.13.

| $NPV$ | Scalefactor |
|---|---|
| 1 | 1.22 |
| 2 | 1.32 |
| 3 | 1.29 |
| 4 | 1.16 |
| 5 | 1.09 |
| 6 | 1.00 |
| 7 | 1.01 |

**Table A.6:** Scalefactors listed by $NPV$ obtained from $Z \rightarrow ee$ Monte Carlo and data comparisons.

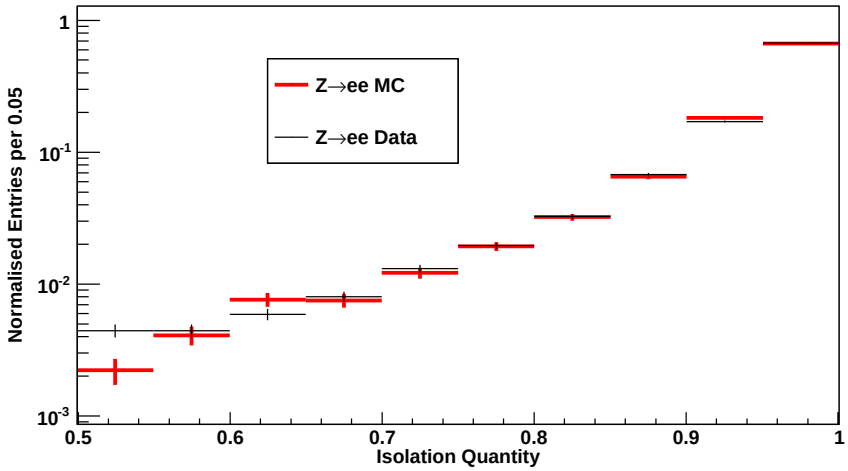


**Figure A.13:** The K-S test optimised corrections for the *NPV=3* distribution.

The efficiency of the selection requirement must be re-calculated to account for the distribution difference in $NPV$. The summary of the re-weighting process is listed in Table A.7.

| $NPVs$ | Passing [Events] | Total [Events] | Pass rate | Pass rate Uncert. | Re-Weight Factor |
|---|---|---|---|---|---|
| 1 | 3005 | 3652 | 0.823 | 0.007 | 0.289 |
| 2 | 2113 | 2739 | 0.771 | 0.008 | 0.389 |
| 3 | 789 | 1073 | 0.735 | 0.014 | 0.230 |
| 4 | 217 | 320 | 0.678 | 0.028 | 0.074 |
| 5 | 37 | 67 | 0.552 | 0.068 | 0.016 |
| 6 | 4 | 7 | 0.571 | 0.247 | 0.002 |
| 7 | 1 | 1 | 1.000 | 0.840 | <0.001 |

**Table A.7:** The pass rate and the re-weight factor as a function of the number of primary vertices in an event for $t\bar{t}$ Monte Carlo.

The combined pass rate for the re-weighted $t\bar{t}$ Monte Carlo yields a result of

$$\epsilon_{I_e} = 0.767 \pm 0.013(\text{stat.}).$$

Two sources of systematic uncertainty are considered. One source is the uncertainty on the NPV distribution, which differs slightly between $Z \to \mu\mu$ and $Z \to ee$. The isolation requirement efficiency is computed for both re-weighting scales, and the difference between the two is taken to be the systematic uncertainty. The second re-weighting scale yields a result of

$$\epsilon_{I_e} = 0.762$$

thus contributing an uncertainty of $\pm$ 0.005. A second uncertainty arises from post-correction differences between Monte Carlo and data, where $Z \to ee$ Monte Carlo and data selection efficiencies are compared. This are found to yield efficiencies of 0.852 and 0.855 for Monte Carlo and data respectively, contributing an overall systematic uncertainty of $\pm$ 0.003. These two uncertainties are combined in quadrature with the statistical uncertainty on the pass rate to yield a result of:

$$\epsilon_{I_e} = 0.767 \pm 0.014.$$

A full comparison of all the primary vertices, and the K-S optimised results, are available in Appendix B.2.

### A.2.7 Invariant Mass Uncertainty

The invariant mass distribution is difficult to compare between Monte Carlo and data given the limited statistics in the analysis. The best estimate for the systematic uncertainty is to use a well-defined channel, for example $Z \rightarrow \mu\mu$ and compare the Monte Carlo and data distributions. This is calculated by increasing the requirements on the analysis to three windows, as demonstrated in Table A.8. The result of this is to take the largest deviation as the systematic uncertainty between data and Monte Carlo as the systematic uncertainty on the Monte Carlo description of the invariant mass. The invariant mass of these reconstructed Z events is presented in Figure A.14. The overall efficiency of the invariant mass is taken from the $t\bar{t}$ Monte Carlo sample.

| Window [GeV/c$^2$] | Monte Carlo Efficiency | Data Efficiency | Deviation |
|---|---|---|---|
| $70 < M_{\mu\mu} < 110$ | 0.976 | 0.962 | 0.014 |
| $80 < M_{\mu\mu} < 100$ | 0.910 | 0.887 | 0.023 |
| $85 < M_{\mu\mu} < 95$ | 0.796 | 0.754 | 0.042 |

**Table A.8:** The difference between Monte Carlo and data for $Z \rightarrow \mu\mu$ reconstruction using different mass windows.

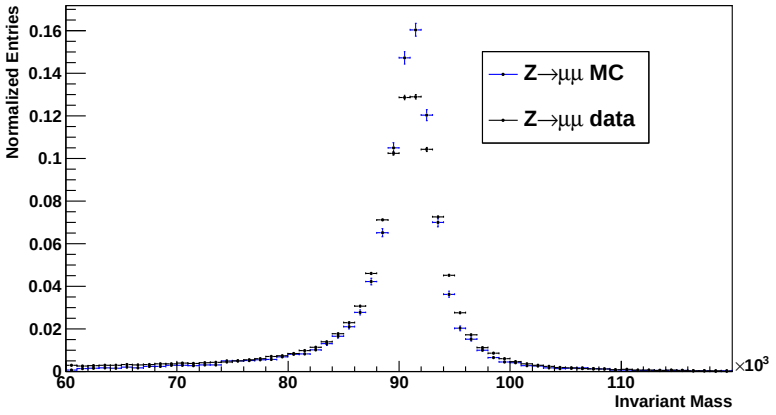


**Figure A.14:** The invariant mass spectrum for $Z \rightarrow \mu\mu$ events in Monte Carlo and data, used for the trigger efficiency study and later systematic uncertainty studies in Section A.2.

The maximum deviation of 0.042 is taken as the difference between the Monte Carlo and the data. This provides an invariant mass requirement efficiency of

$$\epsilon_{M_{inv}} = 0.924 \pm 0.042(\text{syst.}) \pm 0.009(\text{stat.}).$$

### A.2.8 Number of Candidates and Primary Vertex Association Uncertainty

The efficiency of these two requirements are tested in $Z \rightarrow \mu\mu$ Monte Carlo and data. The primary vertex association requirement is found to be compatible between Monte Carlo and data and is also compatible with an efficiency of 1.000. The candidate requirement is found from $t\bar{t}$ Monte Carlo to be 0.972, and the comparison in $Z \rightarrow \mu\mu$ Monte Carlo and data is also found to be consistent, so no systematic uncertainty is taken from this value, or

$$ncand = 0.972 \pm 0.009(\text{stat.}).$$

### A.2.9 Selection Summary

Table A.9 summarises the selection efficiency in this analysis, as well as the statistical and systematic uncertainties, and their combination in quadrature. Due to the statistical uncertainties providing the precision of the systematic uncertainties, these are combined into a single number to contribute a total systematic uncertainty. The final result is, which has an uncertainty of 7%, is:

$$\epsilon_{sel} = 0.535 \pm 0.040(\text{syst.}).$$

| Requirement | Requirement Eff. | Stat. Uncert. [%] | Syst. Uncert. [%] |
|---|---|---|---|
| $ncand$ | 0.972 | 0.9 | 0.0 |
| $M_{inv(\mu,e)}$ | 0.924 | 0.9 | 4.5 |
| $IP_{\mu}$ | 0.993 | 1.0 | 0.7 |
| $IP_{e}$ | 0.990 | 1.0 | 0.7 |
| $IPCA$ | 0.954 | 0.9 | 1.5 |
| $I_{\mu}$ | 0.852 | 1.0 | 4.3 |
| $I_{e}$ | 0.793 | 1.0 | 0.8 |
| Combined | 0.535 | 2.5 | 6.5 |

**Table A.9:** A summary table of all the selection efficiencies and their uncertainties.

## A.3 Reconstruction Efficiency and Systematic Uncertainties

The reconstruction efficiency, $\epsilon_{rec.}$, in Equation (6.2) can be broken down to the components

$$\epsilon_{rec.} = \epsilon_{GEC} \cdot \epsilon_{reso} \cdot \epsilon_{trig} \cdot \epsilon^{e}_{ID} \cdot \epsilon^{\mu}_{ID} \cdot \epsilon^{e}_{track} \cdot \epsilon^{\mu}_{track} \tag{A.1}$$

where the global event cut efficiency, $\epsilon_{GEC}$, is the efficiency for $t\bar{t}$ events to pass the global event cut requirements placed at the trigger stage, $\epsilon_{res}$ being the resolution efficiency for true particles in the kinematic range required compared to the constructed particles (discussed further in Section A.3.8), and the trigger efficiency, $\epsilon_{trig}$, representing the efficiency of the trigger accepting the event. The tracking finding efficiencies, $\epsilon^{\mu}_{track}$ and $\epsilon^{e}_{track}$ represent the probability that a particle of a certain type can be reconstructed as a long track. Where a long track has been reconstructed the particle identification efficiencies, stated as $\epsilon^{\mu}_{ID}$ and $\epsilon^{e}_{ID}$, is the efficiency identifying these tracks as their particles by passing the identification requirements imposed upon them.

### A.3.1 Trigger Efficiency

The trigger efficiency is evaluated by analysis of $Z \rightarrow \mu\mu$ data. Reconstructed Z events (requiring two $\mu$ leptons each of $P_T > 20$ GeV/c and a system requirement of 60 GeV/c$^2$ < M$_{\mu\mu}$ < 120 GeV/c$^2$, following the LHCb paper [183]) are tested to look

at the efficiency of muons passing the relevant L0, HLT1 and HLT2 trigger lines. The transverse momentum is loosened in this case to correspond to the requirement imposed in the selection of $P_T > 15$ GeV/c.

The trigger efficiency is evaluated using a tag-and-probe method on these reconstructed events. The efficiency is then given by the number of events triggered by the tag divided by the number of events triggered on both tag and probe. It is found that 207,132 events of 274,317 pass the tag and probe test in data. This gives an efficiency of 0.756. An evaluation on $t\bar{t}$ Monte Carlo provides a trigger efficiency of 0.727. An evaluation on $Z \rightarrow \mu\mu$ Monte Carlo gives a result of 0.742. The difference in these are taken to be the systematic uncertainty on the trigger efficiency. The efficiency as a function of transverse momentum is stable within the systematic uncertainty. This is presented in Figure A.15.

$$\epsilon_{trig} = 0.756 \pm 0.015(\text{syst.}).$$

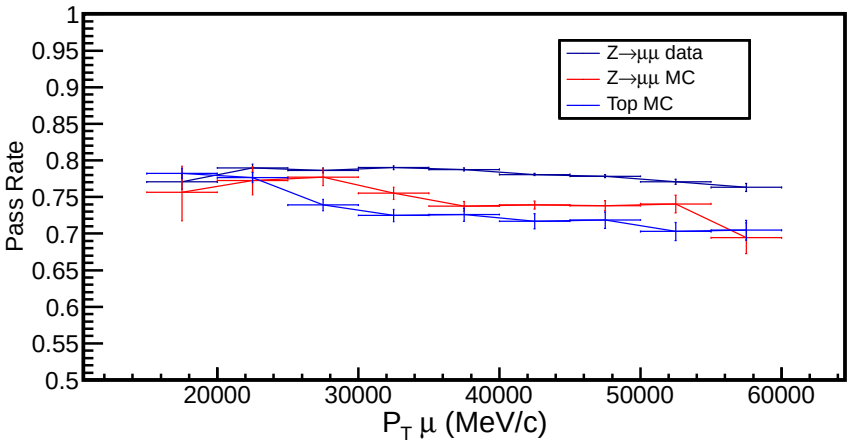


**Figure A.15:** The $Z \rightarrow \mu\mu$ trigger efficiency as a function of transverse momentum.

## A.3.2 Global Event Cut

The trigger line deployed for this analysis, namely the *L0MuonDecision*, *Hlt1SingleMuonHighPTDecision* and *Hlt2SingleMuonHighPTDecision* require that any events passing the trigger must have $< 600$ hits on the SPD detector. To measure

the effect of this on the sample selection, a Monte Carlo versus data comparison of $Z \rightarrow \mu\mu$ is performed, where the events are required to pass the *L0DiMuonDecision*, *Hlt1DiMuonHighMassDecision* and *Hlt2DiMuonZDecision* lines. This requirement is in place as the DiMuon lines only require $N_{SPD} < 900$, rather than 600, which allows for evaluation of the behaviour of the Monte Carlo modelling above the 600 hits threshold.

The number of SPD hits in $Z \rightarrow \mu\mu$ is plotted and compared via a $\chi^2/ndof$ test. This is found in the initial instance to be $\chi^2/ndof = 230.1$, which is presented in Figure A.16, which is then optimised via $\chi^2/ndof$ minimisation through a scale-factor.

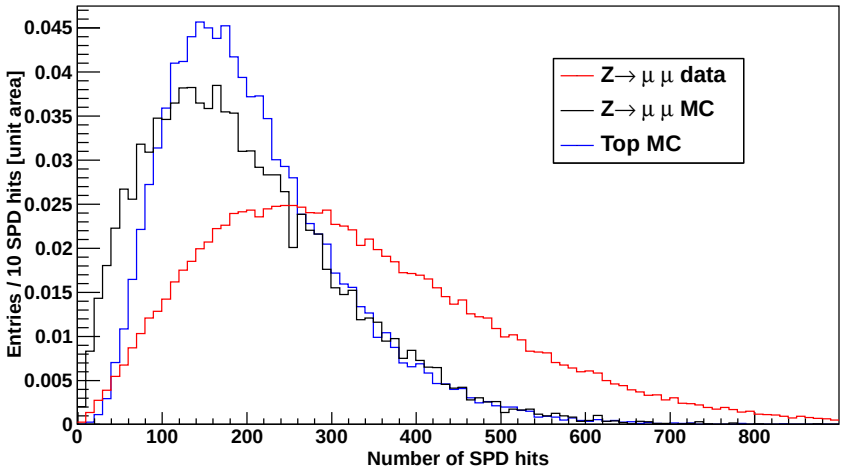


**Figure A.16:** SPD hits in $Z \rightarrow \mu\mu$ Monte Carlo and data, $t\bar{t}$ Monte Carlo without any scale-factor.

The scale-factor used to minimise the difference between the Monte Carlo and data is calculated through an iterative process, and it is found to be optimal at 1.664, presented in Figure A.17.

Furthermore it is found that the average number of interactions per bunch crossing is in disagreement between the $t\bar{t}$ Monte Carlo and data, so a re-weighting process must be carried out to re-weight the number of primary vertices in Monte Carlo to match data. The uncorrected number of primary vertices is presented in Figure A.18.

After the re-weighting and scale-factor process, it is found that the SPD requirement efficiency on the $t\bar{t}$ Monte Carlo is $0.828 \pm 0.011$, with $Z \rightarrow \mu\mu$ in data and Monte Carlo corresponding to 0.928 and 0.905 respectively, with a difference in MC vs data of 0.023. This is combined in quadrature with the statistical uncertainty on the re-

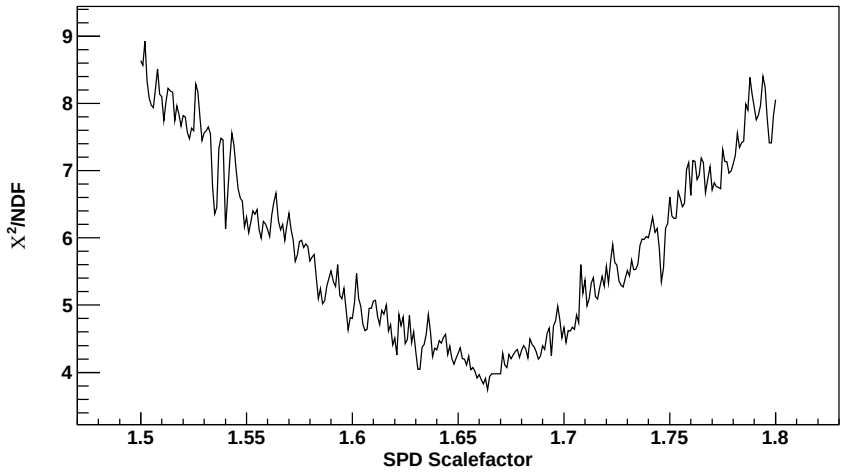


**Figure A.17:** The $\chi^2/ndof$ factor as a function of different scale-factors. The minimised value is chosen as the optimal value for scaling of the Monte Carlo SPD hits to match data.

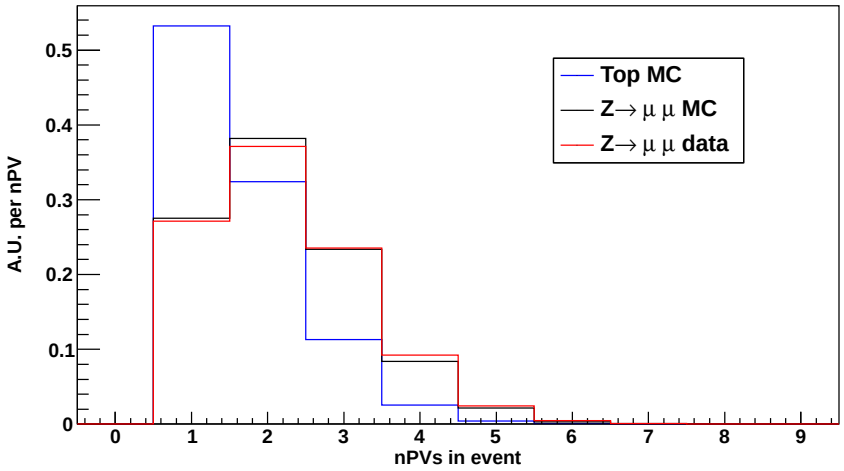


**Figure A.18:** The uncorrected number of reconstructed interactions per bunch crossing in Monte Carlo and data. The $t\bar{t}$ sample has poor agreement with data.

weighting efficiency on the $t\bar{t}$ sample to give a total uncertainty of

$$\epsilon_{GEC} = 0.828 \pm 0.025.$$

The final SPD hits distribution is presented in Figure A.19.

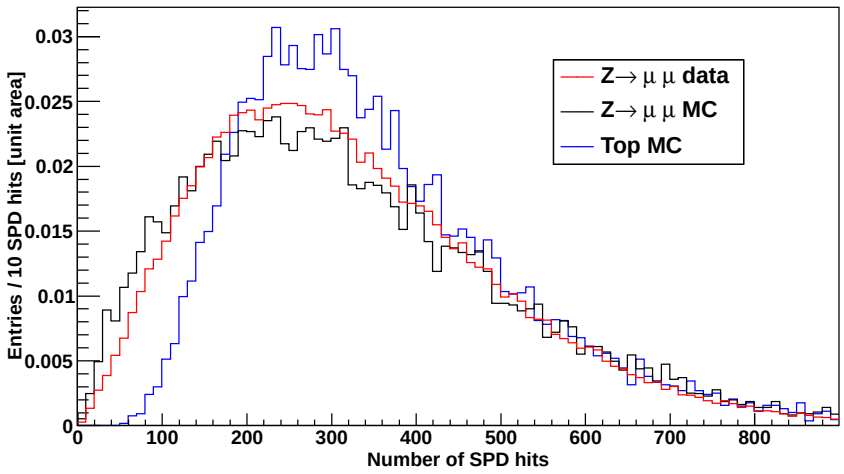


**Figure A.19:** The SPD hit distribution for Monte Carlo and data after the re-weighting process for the number of primary vertices and the scale-factor calibration.

### A.3.3 Muon Tracking Efficiency

The muon tracking efficiency is calculated on Monte Carlo samples by analysing events in which a muon of $P_T > 15$ GeV/c is in the LHCb acceptance ($2 < \eta < 4.5$) and is successfully reconstructed as a track. The tracking efficiency is calculated from $t\bar{t}$ Monte Carlo to be $\epsilon^{\mu}_{track} = 0.941$. The systematic uncertainty on this value is considered by calculating the same quantity on $Z \rightarrow \mu\mu$ Monte Carlo and performing a data driven muon tracking efficiency calculation. The $Z$ Monte Carlo gives a result of $\epsilon^{\mu}_{track} = 0.975$. The data evaluation requires a more complicated method described below.

A data search for $Z \rightarrow \mu\mu$ is performed, using a 'tag-and-probe' technique. This technique uses a muon as the tag, and the probe is a muon-TT track [184], and is demonstrated in Figure A.20. Muon tracks are, by default, constructed using VELO seeds and T-station information, with the particle identification being carried out in the muon chambers. By constructing a muon-TT track, that is to say a track using information only from the TT station and the muon chambers, it is possible to construct

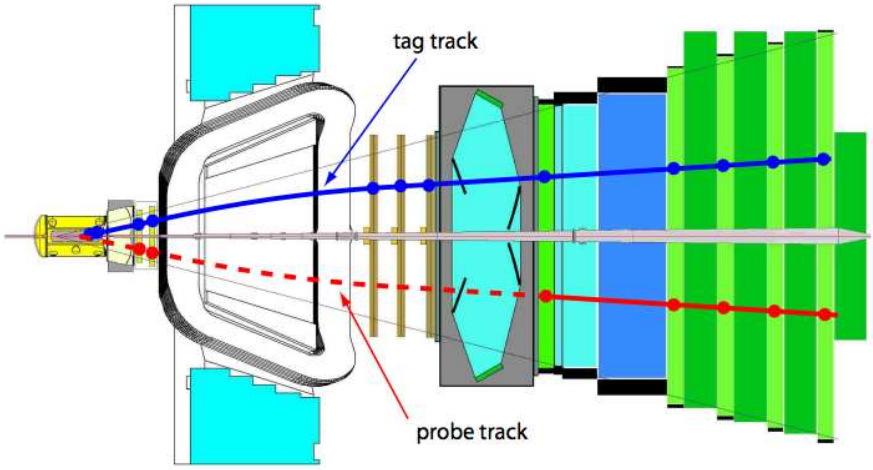


**Figure A.20:** A demonstration of the tag and probe method. The tag track has been clearly identified as a muon track with VELO and T station hits. The probe track only requires TT and muon chamber hits to qualify. Reproduced from [184].

muon candidates independent of the information used to construct the standard muons used in the $Z \to \mu\mu$ analysis. The probe then looks for a matching standard muon, and the rate at which this is found is the muon tracking efficiency. When this is performed on data, it is found to be $\epsilon^{\mu}_{track} = 0.961$ [185]. The difference between the $Z$ Monte Carlo and data is then normalised to the tracking efficiency for the $t\bar{t}$ Monte Carlo sample, providing a systematic uncertainty of 0.014

$$\epsilon^{\mu}_{track} = 0.941 \pm 0.014.$$

### A.3.4 Muon Identification Efficiency

The muon identification efficiency is calculated on Monte Carlo by looking at events where a Monte Carlo muon has a track reconstructed. This track then has its requirements checked against the muon identification requirements, and the proportion of tracks originating from a Monte Carlo muon reconstructed as a muon compared to the total number of tracks originating from a Monte Carlo muon is the identification efficiency. This is calculated in $t\bar{t}$ Monte Carlo to be $\epsilon^{\mu}_{ID} = 0.990$. The systematic uncertainty of this is computed by a comparison between the identification efficiency in $Z \to \mu\mu$ Monte Carlo ($\epsilon^{\mu}_{ID} = 0.973$) and data.

The muon identification efficiency is performed on $Z \rightarrow \mu\mu$ data by using a tag and probe method where the tag is a single well reconstructed muon [97]. The probe is then all tracks in the event, and an additional criteria is imposed that the probe must be isolated for purity reasons. The tag and probe technique then attempts to reconstruct $Z$ bosons using the standard requirements outlined in Table A.2. The identification efficiency is calculated by the number of probes which successfully create a potential $Z$ candidate (e.g. $60 < M_{inv} < 120$ GeV/c$^2$) divided by the total number of probes. It is found on data to be $\epsilon^{\mu}_{ID} = 0.985$ [185]. Thus this provides the systematic uncertainty on the muon identification efficiency, or

$$\epsilon^{\mu}_{ID} = 0.990 \pm 0.012.$$

### A.3.5 Electron Tracking Efficiency

The electron tracking efficiency is calculated from $t\bar{t}$ Monte Carlo by analysing the proportion of electrons with $2 < \eta < 4.5$ and $P_T$ >15 GeV/c that have a track reconstructed. This is calculated to be $\epsilon^{e}_{track} = 0.867$. The systematic uncertainty is taken from [97], which uses a tag and probe method on $Z \rightarrow ee$ events in data. The systematic uncertainty is taken to be 3.0%. This provides an electron tracking efficiency of

$$\epsilon^{e}_{track} = 0.867 \pm 0.026.$$

### A.3.6 Electron Identification Efficiency

The electron identification efficiency is calculated from $t\bar{t}$ Monte Carlo by looking at the number of events in which a Monte Carlo electron has a track successfully reconstructed compared to the number of cases where this electron passes the requirements listed in below. This is calculated to be $\epsilon^{e}_{ID} = 0.864$. The systematic uncertainty of this quantity is taken from [98], where a tag and probe technique is applied, requiring only the tag to pass the electron identification. This provides an electron identification efficiency of

$$\epsilon^{e}_{ID} = 0.864 \pm 0.010.$$

### A.3.7 *b*-jet Reconstruction Efficiency

The $b$-jet reconstruction efficiency is calculated from $t\bar{t}$ Monte Carlo by looking for jets in the event which is identified as originating from a $b$ hadron, and looking at the rate at which these events pass the selection requirement. The efficiency is found to be $\epsilon^{b}_{eff} = 0.579 \pm 0.006$.

The systematic uncertainty is taken from Monte Carlo, by computing the mis-tag rate in Monte Carlo, which is 0.097. The mis-tag rate is calculated by looking at the number of jets which are identified as not originating from a $b$ hadron, and computing the rate. This is combined in quadrature with the efficiency and normalised by the efficiency to give an uncertainty of 0.097

$$\epsilon_b = 0.579 \pm 0.097.$$

The $b$-tagging uncertainty is large compared to the uncertainties at ATLAS or CMS, and could be reduced by using a data-driven method. For example a tag-and-probe on $b\bar{b}$ pairs could be utilised, however it is experimentally difficult to have an unbiased sample of $b$-jets. Triggers in LHCb exploit properties of $b$-mesons, such as the lifetime, and would potentially bias any efficiency measurement reliant on them.

### A.3.8 Resolution Efficiency

Due to the limitations of the electromagnetic calorimeter in LHCb (detailed further in in Section 3.2.3) the energy reconstruction of high momentum electrons can be poor. This results in an inefficiency in the reconstruction of $P_T > 15$ GeV electrons. This is evaluated in Section A.2.5 to be

$$\epsilon_{reso} = 0.736 \pm 0.005.$$

### A.3.9 Muon ECAL Veto

For the purpose of sample purity by removing high $P_T$ electrons misidentified as muons, it is possible to use a veto requirement on the muons. This is done by looking at the ECAL deposits associated with the track, and removing candidates above a certain threshold.

The requirement in place is:

$$E_{ECAL} < 10 \text{ GeV}.$$

The efficiency of which is estimated through the $t\bar{t}$ Monte Carlo, and compared to $Z \rightarrow \mu\mu$ Monte Carlo and data. The efficiency in $t\bar{t}$ Monte Carlo is found to be 0.979. For $Z \rightarrow \mu\mu$ Monte Carlo, this number is found to be 0.974, and in data it is found to be 0.976. The veto efficiency summary can be given as:

$$\epsilon^{\mu}_{veto} = 0.979 \pm 0.002.$$

### A.3.10 Reconstruction Efficiency Summary

A summary table of the efficiencies of the reconstruction and the systematic uncertainties upon those quantities is presented in Table A.10. The combined value is the product of the efficiencies, and the combined systematic uncertainty is the weighted quadrature combination of the systematic uncertainties and their respective quantities.

| Parameter | Efficiency | Systematic Uncertainty [%] |
|---|---|---|
| $\epsilon_{trig}$ | 0.756 | 2.0 |
| $\epsilon_{GEC}$ | 0.842 | 2.7 |
| $\epsilon^{\mu}_{track}$ | 0.946 | 1.5 |
| $\epsilon^{\mu}_{ID}$ | 0.986 | 1.2 |
| $\epsilon^{e}_{track}$ | 0.886 | 2.9 |
| $\epsilon^{e}_{ID}$ | 0.843 | 1.2 |
| $\epsilon_{reso}$ | 0.738 | 0.7 |
| $\epsilon_{b}$ | 0.579 | 16.8 |
| $\epsilon^{\mu}_{veto}$ | 0.979 | 2.0 |
| Combination | 0.186 | 17.6 |

**Table A.10:** A summary table of the reconstruction efficiencies and the systematic uncertainties on each quantity.

This gives a combined reconstruction efficiency for events which have $2.0 < \eta_{\mu}, \eta_{e} < 4.5$, $2.0 < \eta_{b} < 4.5$, $P_T(\mu, e)$ <15 GeV/c and $P_T(b)$ <5 GeV/c of

$$\epsilon_{rec} = 0.186 \pm 0.033.$$

## A.4 Acceptance and Final State Radiation

The requirement is imposed that $2.0 < \eta_{jet} < 4.5$, which must then be compared to the original $b$-quark direction. This is computed from several numbers:

*Muon Acceptance*: is when $\mu$ leptons outside of $2 < \eta_{\mu} < 4.5$ are either bent or reconstructed as being inside of this range. The opposite case must also be considered, where leptons that would otherwise contribute to the fiducial cross-section are subsequently outside of it. The number of muons bending out(in) is 289(219) of a total of 73359 in the fiducial region.

*Electron Acceptance*: employs the same principle as the muons, by looking for cases where electrons that should (should not) be contributing to the candidates in fact do (do not). A total of 267(209) electrons are found bending out(in) of the fiducial region from 73359.

*b-jet* $P_T$: requirements are only loosely translated to the fiducial requirements. The fiducial requirement is that a $b$-quark must be inside the volume of $2 < \eta < 4.5$, with a $P_T > 5$ GeV/c. The jets are constructed with the requirement of a minimum $P_T$ of 5 GeV/c, but as this is the scalar summation of all the particles in the jet, it does not necessarily translate to the original $b$-quark having sufficient $P_T$. This is anticipated to be low, due to the high mass of the top quark, resulting in typically significant boosts for the $b$-quark. The number of jets originating from $b$-quarks with low $P_T$ is found to be 26 from 55765.

*b-jet edge effects*: can occur when a $b$-quark outside of the fiducial region decays into a jet which is at least partially reconstructed as being in $2 < \eta < 4.5$ and being identified as a $b$-jet. This is found occur in 2269 of 55765 cases.

*b-jet fragmentation effects*: can occur when a $b$-quark inside the fiducial region is reconstructed as a jet that is outside of the $\eta$ range. This is found to occur in 265 of 55765 cases.

The resulting acceptance factor is computed to be $1.035 \pm 0.006$, where the uncertainty arises from the combined statistical uncertainties on the component quantities.

## A.5 QCD Background Uncertainty

Due to the lack of events in the same sign channel, the QCD background uncertainty is calculated by looking at the cut efficiencies of the $\epsilon^{\mu}_{veto}$, $\epsilon_{iso\mu}$, $\epsilon_{isoe}$, and $\epsilon_{b-tag}$ on the same sign channel, and then scaling these numbers by the number of events prior to these four requirements. The efficiencies are found to be 33.9%, 11.3%, 4.5% and 91.1% respectively, which when scaled by the 575 events prior to the imposition of these requirements yields an estimated $\sim$0.90 events. This is taken as the systematic uncertainty on the QCD background.

# Appendix B

# Isolation Corrections

## B.1 Muon Isolation

Figure B.1 to Figure B.4 present the isolation for $Z \rightarrow \mu\mu$ data and Monte Carlo before corrections. A summary table of the K-S test optimal scale factors are presented in Table B.1, and the same plots after corrections are presented in Figure B.5 to Figure B.8.

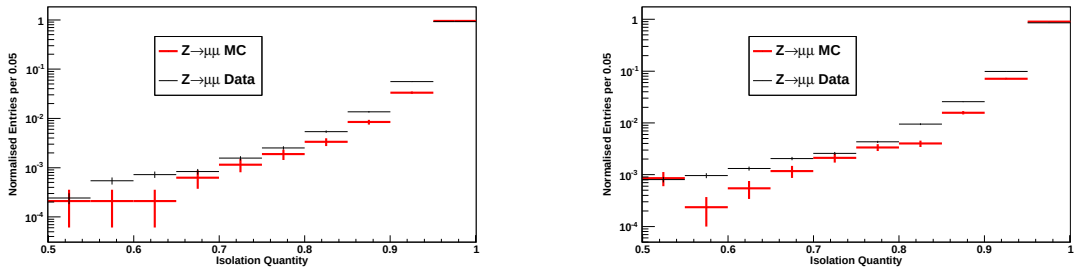


**Figure B.1:** Left: The unscaled muon isolation for $NPV$=1, and Right: for $NPV$=2.

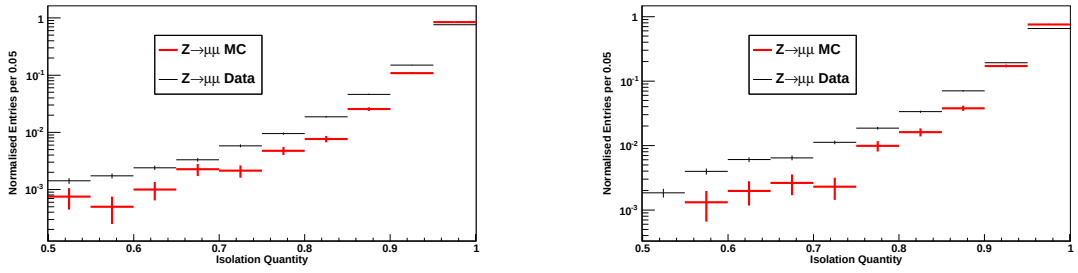


**Figure B.2:** Left: The unscaled muon isolation for $NPV$=3, and Right: for $NPV$=4.

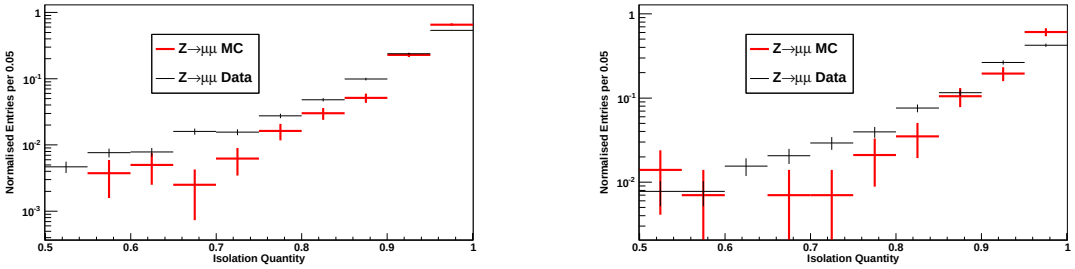


**Figure B.3:** Left: The unscaled muon isolation for $NPV$=5, and Right: for $NPV$=6.

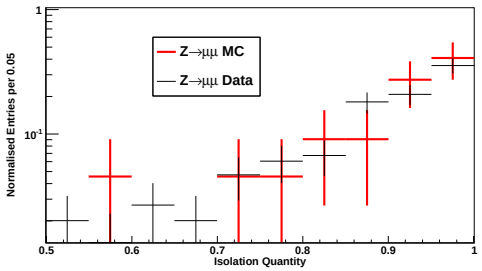


**Figure B.4:** Unscaled muon isolation for $NPV = 7$.

| NPV | K-S test optimal |
|---|---|
| 1 | 1.33 |
| 2 | 1.35 |
| 3 | 1.43 |
| 4 | 1.47 |
| 5 | 1.45 |
| 6 | 1.71 |
| 7 | 1.51 |

**Table B.1:** A full list of the scale-factors used for different $NPV$ values in correcting the $NPV$ distribution for the $t\bar{t}$ Monte Carlo.

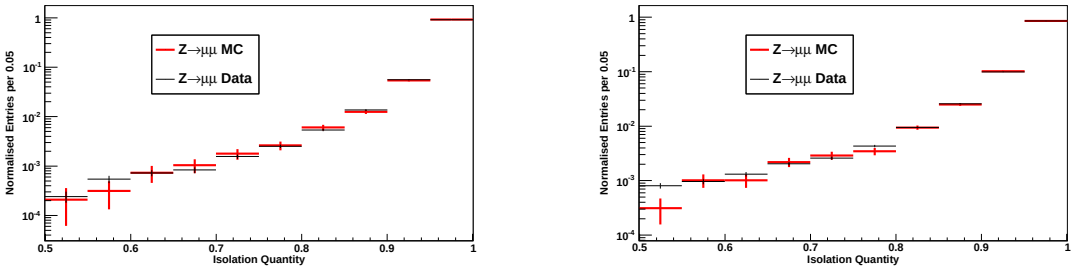


**Figure B.5:** Left: The K-S test optimal value for $NPV$=1, and Right: for $NPV$=2.

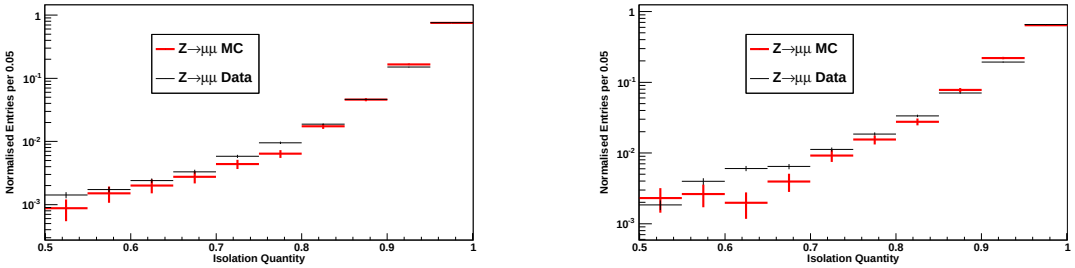


**Figure B.6:** Left: The K-S test optimal value for $NPV$=3, and Right: for $NPV$=4.

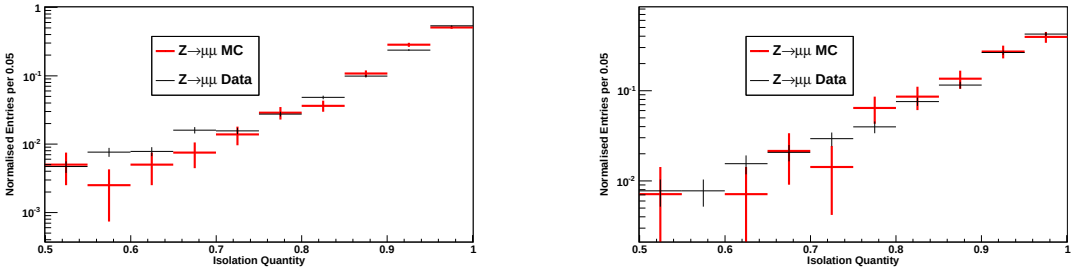


**Figure B.7:** Left: The K-S test optimal value for $NPV$=5, and Right: for $NPV$=6.

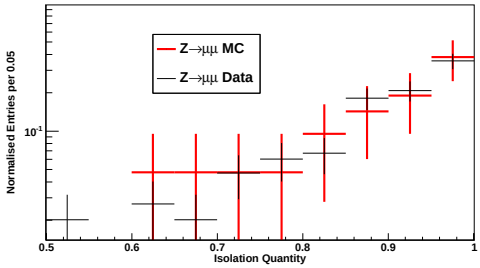


**Figure B.8:** The K-S test optimal value for $NPV = 7$.

## B.2 Electron Isolation

Figure B.9 to Figure B.12 present the isolation for $Z \rightarrow ee$ data and Monte Carlo before corrections. A summary table of the K-S test optimal scale factors are presented in Table B.2, and the same plots after corrections are presented in Figure B.13 to Figure B.16.

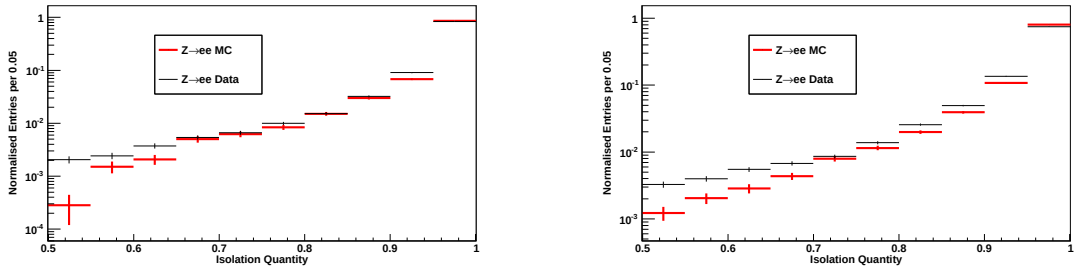


**Figure B.9:** Left: The unscaled electron isolation for $NPV$=1, and Right: for $NPV$=2.

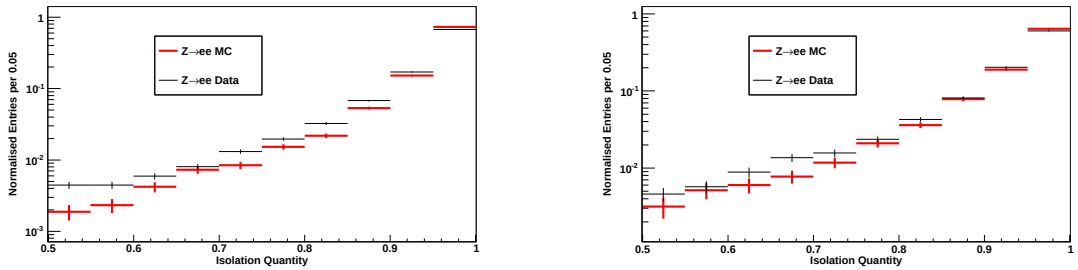


**Figure B.10:** Left: The unscaled electron isolation for $NPV$=3, and Right: for $NPV$=4.

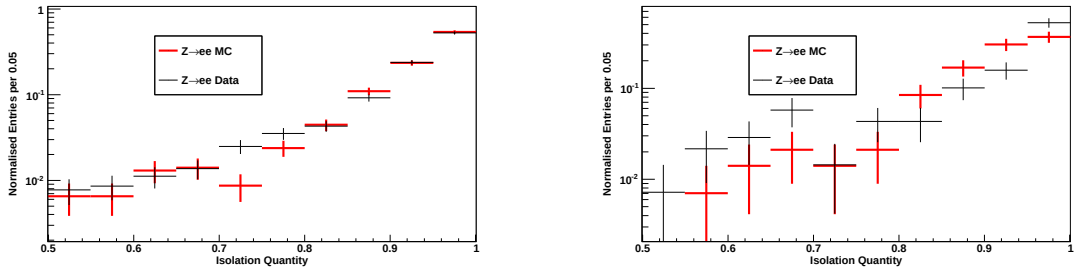


**Figure B.11:** Left: The unscaled electron isolation for $NPV$=5, and Right: for $NPV$=6.

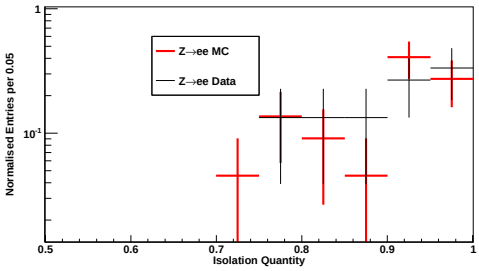


**Figure B.12:** Unscaled electron isolation for $NPV = 7$.

| NPV | K-S test optimal |
|---|---|
| 1 | 1.22 |
| 2 | 1.32 |
| 3 | 1.29 |
| 4 | 1.16 |
| 5 | 1.09 |
| 6 | 1.00 |
| 7 | 1.01 |

**Table B.2:** A full list of the scale-factors used for different $NPV$ values in correcting the $NPV$ distribution for the $t\bar{t}$ Monte Carlo.

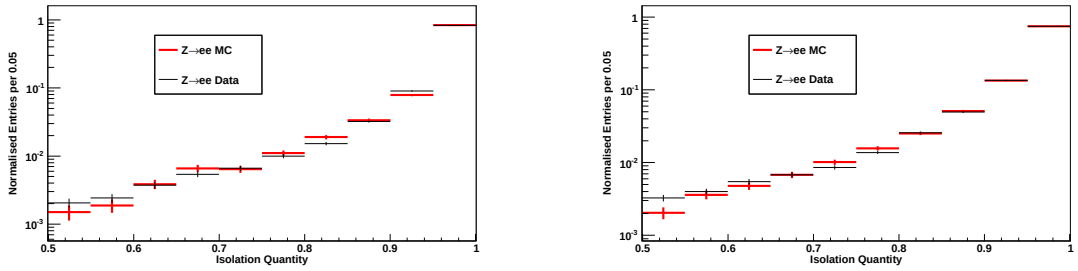


**Figure B.13:** Left: The K-S test optimal value for $NPV$=1, and Right: for $NPV$=2.

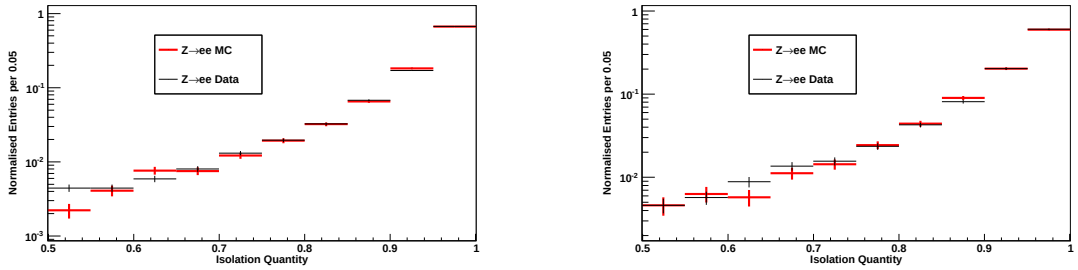


**Figure B.14:** Left: The K-S test optimal value for $NPV$=3, and Right: for $NPV$=4.

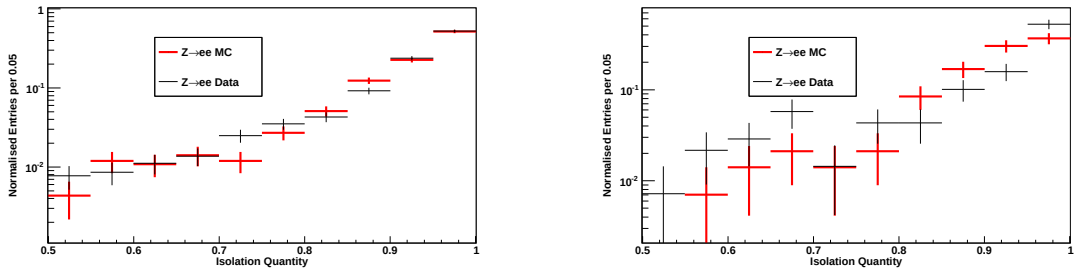


**Figure B.15:** Left: The K-S test optimal value for $NPV$=5, and Right: for $NPV$=6.

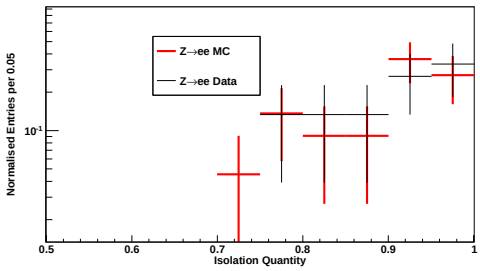


**Figure B.16:** The K-S test optimal value for $NPV = 7$.

# References


[1] J. Beringer *et al.*, Particle Data Group, Phys. Rev. D **86**, 010001 (2012).

[2] F. Halzen and A. D. Martin, *Quarks and Leptons*, Wiley (1984).

[3] R. Mann, *An Introduction to Particle Physics and the Standard Model*, CRC Press (2009).

[4] P. A. M. Dirac, Proceedings of the Royal Society of London, Series A. **117**, 610 (1928).

[5] H. Goldstein, *Classical Mechanics*, Addison-Wesley Publishing Company, Reading MA (1980).

[6] M. Herrero, *The Standard Model*, hep-ph/9812242 (1998).

[7] T. Nakano and K. Nishijima, Prog. Theor. Phys. **10**, 581 (1953).

[8] B. Pontecorve, Sov. Phys. JETP **26**, 984 (1968).

[9] P. W. Higgs, Phys. Rev. Lett. **13**,, 508, (1964).

[10] D. Silverman, Available at `http://sites.uci.edu/energyobserver/2013/02/24`

[11] J. Goldstone, Nuovo Cim. **19**, 154 (1961).

[12] K. J. Barnes, O. J. Senior and N. D. Virgo, J. Phys. A:Math. Gen. **29**, 4957 (1996).

[13] A. G. Cohen, D.B. Kaplan and A. E. Nelson, Ann. Rev. Nucl. Part. Sci. **43**, 27 (1993).

[14] J. Christenson *et al.*, Phys. Rev. Lett. **13**, 138 (1964).

[15] M. L. Perl *et al.*, Phys. Rev. Lett. **35**, 1489 (1975).

[16] S. Herb *et al.*, Phys. Rev. Lett. **39**, 252 (1977).

[17] K. Kodama *et al.*, The DONUT Collaboration, Phys. Lett. **B504**, 218 (2001).

[18] D. Kahana and S. Kahana, Phys. Rev. **D52**, 3065 (1995).

[19] F. Abe *et al.*, The CDF Collaboration, Phys. Rev. Lett. **74**, 2626 (1995).

[20] S. Abachi *et al.*, The D0 Collaboration, Phys. Rev. Lett. **74**, 2422 (1995).

[21] I. Bigi *et al.*, Phys. Lett. **B181**, 157 (1986).

[22] A. Accardi, W. Melnitchouk, J. F. Owens, Phys. Rev. **D87**, 094012 (2013).

[23] J. M. Campbell, J. W. Houston and W. J. Stirling, Rept. Prog. Phys. **70**, 89 (2007).

[24] L. Reina, Available at `http://www.phys.psu.edu/~cteq/schools/summer09/`

[25] N. Kidonakis, *Top Quark Theoretical Cross Sections and pT and Rapidity Distributions*, hep-ph/1109.3231 (2011).

[26] N. Kidonakis, *Differential and total cross sections for top pair and single top production*, hep-ph/1205.3453 (2012).

[27] D. Karabacak, S. Nadi and S. K. Rai, Phys. Rev. **D85** 075011 (2012).

[28] *Determination of the Top Quark Mass with a Template Method in the All Hadronic Decay Channel using 2.04/fb of ATLAS Data*, ATLAS-CONF-2012-030 (2012).

[29] *Measurement of the top quark mass in the dilepton channel in pp collisions at* $\sqrt{s}$*=7TeV*, CMS-PAS-TOP-11-016 (2012).

[30] *Measurement of the ttbar production cross-section in pp collisions at* $\sqrt{s}$ *= 7 TeV using kinematic information of lepton+jets events*, ATLAS-CONF-2011-121 (2011).

[31] S. Chatrchyan *et al.*, CMS Collaboration, JHEP **1211**, 067 (2012).

[32] *Determination of the Top Quark Mass from the ttbar Cross Section at* $\sqrt{s}$ *= 7 TeV*, CMS-PAS-TOP-11-008 (2011).

[33] S. Blyweert, *Top-quark mass measurements at the LHC*, hep-ex/1205.2175 (2012).

[34] *Combination of ATLAS and CMS top-quark pair cross section measurements using up to 1.1 fb-1 of data at 7 TeV*, ATLAS-CONF-2012-134 (2012).

[35] M. Aoki, *Top Quark Production at the LHC for the ATLAS and CMS Collaborations*, hep-ex/1305.3695 (2013).

[36] *Measurement of the top quark pair production cross section in the single-lepton channel with ATLAS in proton-proton collisions at 8 TeV using kinematic fits with b-tagging*, ATLAS-CONF-2012-149 (2012).

[37] *Top pair cross section in e/mu+jets at 8 TeV*, CMS-PAS-TOP-12-006 (2012).

[38] M. Jezabek and J. H. Kuhn, Nucl. Phys. **B314**, 1 (1989).

[39] L. H. Orr and J. L. Rosner, Phys. Lett. **B246**, 221 (1990).

[40] V. M. Abazov *et al.*, D0 Collaboration, Nature **429**, 638 (2004).

[41] J. Shu, K. Wang and G. Zhu, Phys. Rev. **D85**, 034008 (2012).

[42] O. Antunano, J. H. Kuhn and G. Rodrigo, Phys. Rev. **D77**, 014003 (2008).

[43] A. Djouadi *et al.*, Phys. Rev. **D82**, 071702 (2010).

[44] E. L. Berger *et al.*, Phys. Rev. Lett **106**, 201801 (2011).

[45] V. M. Abazov *et al.*, Phys. Rev. **D84**, 112005 (2011).

[46] *Study of the Top Quark Production Asymmetry and Its Mass and Rapidity Dependence in the Full Run II Tevatron Dataset*, CDF-Note-10807, (2012).

[47] K. Rinnert, *Top physics program in LHCb*, available at `http://indico.cern.ch/conferenceOtherViews.py?view=standard&confId=189617`

[48] R. Gauld, *Feasibility of top quark measurements at LHCb and constraints on the large-x gluon PDF*, hep-ph/1311.1810 (2013).

[49] J. H. Kuhn and G. Rodrigo, Phys. Rev. Lett **81**, 49 (1998).

[50] V. Ahrens *et al.*, *Forward-Backward and Charge Asymmetries in the Standard Model*, hep-ph/1212.5859 (2012).

[51] G. Rodrigo, *The ttbar asymmetry in the Standard Model and beyond*, hep-ph/1207.0331 (2012).

[52] *Measurement of the charge asymmetry in dileptonic decay of top quark pairs in pp collisions at* $\sqrt{s}$ *= 7 TeV using the ATLAS detector*, ATLAS-CONF-2012-057 (2012).

[53] K. Shaw, ATLAS Collaboration, J. Phys. Conf. Ser. **452**, 012058 (2013).

[54] M. Giordani, *Charge Asymmetry in Top Pairs at ATLAS*, ATL-PHYS-PROC-2012-270 (2012).

[55] R. Gauld, *Measuring top quark production asymmetries at LHCb*, LHCb-PUB-2013-009 (2013).

[56] P. Bryant and L. Evans, JINST **3**, S08001 (2008).

[57] *CERN - Science Grand Format*, available at `http://bigscience.web.cern.ch/bigscience/en/lhc/lhc2.html`

[58] G. Aad *et al.*, ATLAS Collaboration, JINST **3**, S08003 (2008).

[59] S. Chatrchyan *et al.*, CMS Collaboration, JINST **3**, S08004 (2008).

[60] K. Aamodt *et al.*, ALICE Collaboration, JINST **3**, S08002 (2008).

[61] A. A. Alves *et al.*, LHCb Collaboration, JINST **3**, S08005 (2008).

[62] S. Y. Lee, *Accelerator Physics*, World Scientific Publishing Co. Pte. Ltd., (2004).

[63] N. V. Krasnikov and V. A. Matveev, Theor. Math. Phys **132**, 1189 (2002).

[64] *Combination of results on the rare decays* $B^0_{(s)} \to \mu^+\mu^-$ *from the CMS and LHCb experiments*, LHCB-CONF-2013-012-001, (2013).

[65] D. Fournier, EPJ Web Conf. **28**, 01003 (2012).

[66] S. Mrenna, T. Sjostrand and P. Skands, JHEP **0605**, 026 (2006).

[67] *LHCb : Technical Proposal*, Tech. Proposal, CERN, Geneva (1998).

[68] *LHCb Magnet Technical Design Report*, CERN/LHCC 2001-007 (2001).

[69] *LHCb Inner Tracker Technical Design Report*, CERN/LHCC 2002-029 (2002).

[70] *LHCb Outer Tracker Technical Design Report*, CERN/LHCC 2001-024 (2001).

[71] M. Needham and T. Ruf, *Estimation of the material budget of the LHCb detector*, LHCb-2007-025 (2007).

[72] *LHCb - Large Hadron Collider Beauty Experiment*, available at `http://lhcb-public.web.cern.ch/lhcb-public/en/Detector/VELO-en.html`

[73] P. Turner, *Silicon Sensor Design and Geometry*, EDMS Document 401568 (2005).

[74] *LHCb VELO Technical Design Report*, CERN/LHCC 2001-011 (2001).

[75] M. Agari *et al.*, Nucl. Instrum. Meth. **A518**, 468 (2004).

[76] S. Loecher and M. Schmelling, *The Beetle Reference Manual*, LHCb-2005-105 (2006).

[77] A. Bay *et al.*, Nucl. Instrum. Meth. **A535**, 497 (2004).

[78] C. Parkes and T. Szumlak, *Application of the Pedestal Following Algorithm to the VELO Detector*, LHCb-2009-036 (2009).

[79] N. Tuning, *L1-type clustering in the VELO on test-beam data and simulation*, LHCb-2003-073 (2003).

[80] A. Papadelis, *Characterisation and Commissioning of the LHCb VELO detector*, PhD thesis, VU University, Amsterdam (2009).

[81] L. Landau, J. Phys. (USSR) **8**, 201 (1944).

[82] VELO Conference Plots, available at `https://lbtwiki.cern.ch/bin/view/VELO/VELOConferencePlots`

[83] H. Spieler, *Semiconductor Detector Systems*, Oxford University Press (2005).

[84] B. Rakotomiaramanana, *The Design and Production of the LHCb VELO High Voltage System and Analysis of the Bd K* + − Rare Decay*, PhD thesis, Glasgow University, Glasgow, (2010).

[85] H. F. W. Sadrozinski, ICFA Instrum. Bull. **14**, 9 (1997).

[86] M. van Beuzekom, A. Van Lysebetten and B. Verlatt, Proceedings of Science **009**, (2007).

[87] Instituto Internacional del Frio, *8th IIR Gustav Lorentzen Conference on Natural Working Fluids (GL2008)*, (2008).

[88] A. Van Lysebetten, Nucl. Instrum. Meth. **A617**, 67 (2010).

[89] G. Casse *et al.*, *VELO module production: Vacuum tank tests*, CERN-LHCB-2007-082 (2008).

[90] *LHCb Reoptimized Detector Design and Performance Technical Design Report*, CERN/LHCC 2003-0301 (2003).

[91] G. F. Knoll, *Radiation detection and measurement*, Wiley (2000).

[92] *LHCb RICH Technical Design Report*, CERN/LHCC 2000-037 (2000).

[93] *LHCb Calorimeter Technical Design Report*, CERN/LHCC 2000-036 (2000).

[94] C. W. Fabjan and R. Wigmans, Rept. Prog. Phys **52**, 1519 (1989).

[95] I. Machikhiliyan, *First years of running for the LHCb Calorimeter System*, LHCb-PROC-2013-048, (2013).

[96] I. Machikhiliyan, J. Phys. Conf. Ser. **160**, 012047 (2009).

[97] S. Farry, *A measurement of Z production using tau final states with the LHCb detector*, CERN-THESIS-2012-227 (2012).

[98] R. Aaij *et al.*, JHEP **1302**, 106 (2013).

[99] I. Machikhiliyan, Nucl. Phys. Proc. Suppl. **177-178**, 310 (2008).

[100] *LHCb Muon Technical Design Report*, CERN/LHCC 2001-010 (2001).

[101] A. Bondar *et al.*, Nucl. Instrum. Meth. **A493**, 8 (2002).

[102] *Addendum to the LHCb Muon Technical Design Report*, CERN/LHCC 2003-002 (2003).

[103] *Second Addendum to the LHCb Muon Technical Design Report*, CERN/LHCC 2005-012 (2005).

[104] S. M. Sze, *Semiconductor Devices*, John Wiley & Sons (2002).

[105] R. Bailey *et al.*, Nucl. Instrum. Meth. **213**, 201 (1983).

[106] G. Lutz, *Semiconductor Radiation Detectors*, Springer (1999).

[107] A. Affolder *et al.*, *Radiation damage in the LHCb Vertex Locator*, physics.ins-det/1302.5259 (2013).

[108] H. W. Kraner, Z. Li and K. U. Posnecker, Nucl. Instrum. Meth. **A279**, 266 (29189).

[109] G. Patel, *Liverpool LHCb Velo Module Production*, available at `http://hep.ph.liv.ac.uk/velodb/velo1`

[110] A. Chilingarov, *Intrinsic Concentration and Generation Current Temperature Dependence*, available at `http://eprints.lancs.ac.uk/39969`

[111] M. Moll, *Radiation Damage in Silicon Particle Detectors*, Hamburg, University of Hamburg (1999).

[112] M. Moll, *RD50 Status Report 2009/2010 - Radiation hard semiconductor devices for very high luminosity colliders*, CERN-LHCC-2012-010 (2012).

[113] H. E. Boesch and F. B. McLean, IEEE Trans. Nucl. Sci. **32**, 3940 (1985).

[114] H. E. Boesch and F. Taylor, IEEE Trans. Nucl. Sci. **31** 1273 (1984).

[115] G. Hall, Rep. Proc. Phys **57**, 481 (1994).

[116] *RUNDB - Fills*, available at `http://lbrundb.cern.ch`

[117] T. J. V. Bowcock and G. Casse, *Operating conditions for the VELO silicon*, LHCb-2001-069 (2001).

[118] T. Bowcock, Private Communication, (2013).

[119] E. Rodrigues, *Tracking Definitions*, LHCb-2007-006 (2007).

[120] D. Hutchcroft, *VELO Pattern Recognition*, LHCb-2007-013 (2007).

[121] R. W. Forty and M. Needham, *Standalone Track Reconstruction in the T-stations*, LHCb-2007-022 (2007).

[122] O. Callot, *Online Pattern Recognition*, LHCb-2004-094 (2004).

[123] Y. Xie, *Short track reconstruction with VELO and TT*, LHCb-2003-100 (2003).

[124] M. Needham, *Performance of the Track Matching*, LHCb-2007-129 (2007).

[125] S. Hansmann-Menzemer and S. Stahl, *Update on Downstream Tracking*, LHCb-INT-2009-032 (2009).

[126] J. Van Tilburg, *Track simulation and reconstruction in LHCb*, PhD thesis, Vrije U. Amsterdam, Amsterdam (2005).

[127] R. Fruhwirth, Nucl. Instrum. Meth. **262** 444 (1987).

[128] R. E. Kalman, Transactions of the ASME– Journal of Basic Engineering **D82**, 35 (1960).

[129] A. Strandlie and R. Fruhwirth, Rev. Mod. Phys. **82**, 1419 (2010).

[130] J. R. T. De Mello-Neto and M. Gandelman, *Muon ID performance with the reoptimized LHCb detector*, LHCb-2003-089 (2003).

[131] F. Archilli *et al.*, *Performance of the Muon Identification at LHCb*, physics.ins-det/1306.0249 (2013).

[132] X. Cid Vidal, *Muon Identification in the LHCb experiment*, hep-ex/1005.2585 (2010).

[133] G. Lanfranchi *et al.*, *The Muon Identification Procedure of the LHCb Experiment for the First Data*, LHCb-PUB-2009-013 (2009).

[134] F. Machefert, *LHCb calorimeter electronics. Photon Identification. Calorimeter Calibration.*, PhD thesis, U. Paris-Sud 11, Dept. Phys. Orsay (2011).

[135] I. Belyaev and H. Terrier, *Particle identification with LHCb calorimeters*, LHCb-2003-092 (2003).

[136] N. Harnew, *Particle ID with the LHCb RICH System*, LHCb-PROC-2005-023 (2005).

[137] M. Adinolfi *et al.*, Eur. Phys. J. **C73**, 2431 (2013).

[138] *LHCb Trigger Technical Design Report*, CERN/LHCC 2003-031 (2003).

[139] F. Alessio *et al.*, J. Phys. Conf. Ser. **119**, 022003 (2008).

[140] R. Aaij *et al.*, JINST **8**, P04022 (2013).

[141] E. Aslanides *et al.*, Nucl. Instrum. Meth. **A579**, 989 (2007).

[142] V. A. Baskov *et al.*, *Pile-up detector for LHCb*, LHCb-99-014 (1999).

[143] M. Van Beuzekom *et al.*, *Pile-up veto L0 trigger system for LHCb using large FPGA's*, available at `cds.cern.ch/record/599532` (2002).

[144] R. Cornat, J. Lecoq and P. Perret, *Level-0 decision unit for LHCb*, LHCb-2003-065 (2003).

[145] J. Albrecht, Nucl. Phys. B, Proc. Suppl. **187**, 237 (2009).

[146] G. Corti *et al.*, IEEE Trans. Nucl. Sci. **53**, 1323 (2006).

[147] G. Barrand *et al.*, Comput. Phys. Commun. **140**, 45 (2001).

[148] J. Alwall *et al.*, Comput. Phys. Commun. **176**, 300 (2007).

[149] S. Agostinelli *et al.*, Nucl. Instrum. Methods Phys. Res. A **506**, 250 (2002).

[150] R. Brun *et al.*, Proceedings AIHENP **96**, 81 (1997).

[151] B. R. Webber, Int. J. Mod. Phys. **A15S1**, 577 (2000).

[152] *Measurement of jet production in* $Z^0/\gamma^* \rightarrow \mu^+\mu^-$ *events at LHCb in* $\sqrt{s} = 7$ *TeV pp collisions*, LHCb-CONF-2012-016 (2012).

[153] M. Cacciari, G. P. Salam and G. Soyez, JHEP **0804**, 063 (2008).

[154] M. Cacciari, G. P. Salam and G. Soyez, Eur. Phys. J. **C72**, 1896 (2012).

[155] M. Cacciari and G. P. Salam, Phys. Lett. **B641**, 57 (2006).

[156] M. Wobisch and T. Wengler, *Hadronization corrections to jet cross-sections in deep inelastic scattering*, hep-ph/9907280 (1998).

[157] S. D. Ellis and E. D. Soper, Phys. Rev. **D48**, 3160 (1993).

[158] M. Feindt and M. Prim, Nucl. Instrum. Meth. **A698**, 84 (2013).

[159] M. Feindt, *A Neural Bayesian Estimator for Conditional Probability Densities*, physics/0402093 (2004).

[160] K. Rinnert, Private Communication, (2012).

[161] M. Hashemi, *Single Top Events as a Source of Light Charged Higgs in the Fully Hadronic Final State at LHC*, hep-ph/1305.2096 (2013).

[162] *LHC Higgs Cross Section Working Group*, available at `http://twiki.cern.ch/twiki/bin/view/LHCPhysics/CrossSections`

[163] S. Frixione, P. Nason and G. Ridolfi, JHEP **0709**, 126 (2007).

[164] A. D. Martin *et al.*, Eur. Phys. J. **C70**, 51 (2010).

[165] R. D. Ball *et al.*, Nucl. Phys. **B855**, 608 (2012).

[166] H. L. Lai *et al.*, Phys. Dev. **D82**, 074024 (2010).

[167] F. D. Aaron *et al.*, H1 and ZEUS Collaboration, JHEP **1001**, 109 (2010).

[168] A. Cooper-Sarkar, *PDFs for the LHC*, hep-ph/1107.5170 (2011).

[169] T. Sjostrand *et al.*, Comput. Phys. Commun. **178**, 852 (2008).

[170] *Inclusive W/Z cross section at 8 TeV*, CMS-PAS-SMP-12-011 (2012).

[171] *Measurement of WW production rate*, CMS-PAS-SMP-12-013 (2012).

[172] A. Savin, *Production of W and Z bosons at hadron colliders*, hep-ex/1212.3695 (2012).

[173] T. Melia *et al.*, JHEP **1111**, 078 (2011).

[174] *A Measurement of WZ Production in Proton-Proton Collisions at* $\sqrt{s}$*=8 TeV with the ATLAS Detector*, ATLAS-CONF-2013-021, (2013).

[175] V. Lombardo, *Diboson production cross section at LHC*, hep-ex/1305.377 (2013.)

[176] R. Aaij *et al.*, LHCb Collaboration, JHEP **1305**, 132 (2013).

[177] D. C. Boes, F. A. Graybill and A. M. F. Mood, *Introduction to the Theory of Statistics*, McGraw-Hill International Editions (1974).

[178] V. Balagura, Nucl. Instrum. Meth. **A654**, 634 (2011).

[179] S. van der Meer, *Calibration of the Effective Beam Height in the ISR*, CERN-ISR-PO-68-31 (1968).

[180] M. Ferro-Luzzi, Nucl. Instrm. Meth. **A553**, 388 (2005).

[181] R. Aaij *et al.*, LHCb Collaboration, JINST **7**, P01010 (2012).

[182] P. K. Sinervo, *Signal Significance in Particle Physics* CDF-PUB-STATISTICS-PUBLIC-6031 (2002).

[183] R. Aaij *et al.*, LHCb Collaboration, JHEP **1206**, 058 (2012).

[184] M. De Cian, *A Measurement of the Tracking Efficiency for High-*$p_T$ *Tracks in Reco06-Stripping10 Collision Data*, LHCb-INT-2010-058 (2010).

[185] S. Farry, Private Communication, (2013).